University of Dublin
Trinity College

Modification of anisotropy in ultra-thin magnetic layers

A thesis submitted to the
University of Dublin, Trinity
College
in application for the degree of
Doctor of Philosophy
by

Ciarán Fowley

School of Physics
December 17, 2010

To my Family and Friends

Declaration

This thesis has not been submitted as an exercise for a degree at this or any other university. It is entirely the candidate's own work. The candidate agrees that the Library may lend or copy the thesis upon request. This permission covers only single copies made for study purposes, subject to normal conditions of acknowledgement.

Summary

The areal density of modern magnetic storage stands somewhere between 200-300 Gb/in^2. The scaling of current continuous medium technology is expected to reach a limit below 1 Tb/in^2. Future technologies require discontinuous media in which magnetic islands are used to store individual bits of information. In order for this technology to come to fruition the magnetic anisotropy should be well controlled. The magnetic anisotropy determines both the field required to switch the magnetisation (which has a knock-on effect for power consumption) and the thermal stability (which determines the lifetime of the stored information). At present, magnetic storage exploits materials with high perpendicular magnetic anisotropy. In this thesis we attempt to modify systems possessing perpendicular magnetic anisotropy, and promote these modifications in the context of future memory technologies.

There are three sources of magnetic anisotropy, shape, magneto-crystalline and magneto-elastic anisotropy. These compete to define an anisotropy axis, which can either be in-plane or out-of-plane. The out-of-plane or perpendicular anisotropy is of interest here. In order to have perpendicular magnetic anisotropy, the shape anisotropy which gives rise to the demagnetising energy must be overcome. The magneto-crystalline and magneto-elastic anisotropies can be of the same order of magnitude as the shape anisotropy when certain constraints are met and give a perpendicular easy axis. Magneto-crystalline anisotropy is a result of coupling of the electronic orbitals to a particular crystallographic axis, thus giving a preferred magnetic easy axis. Magneto-elastic anisotropy is a result of stress applied to a film which deform the crystal cell and give an additional contribution to the magneto-crystalline anisotropy.

Band filling of the electron orbits can promote the perpendicular anisotropy through symmetry breaking at interfaces and spin orbit coupling. We can modify this contribution through the electronic density of the ferromagnet. By applying an electric field we can change the number of electrons per unit cell *at the interface* in ultra-thin magnetic layers. This can in turn change the magnetic properties of the interface.

Strain serves to deform the unit cell and, through the magnetostriction constant, can promote perpendicular anisotropy. By modifying the interfacial strain we can systematically decrease the magnetic anisotropy. In ultra-thin films we can detect a change in strain-induced anisotropy electrically.

In the first two chapters a more detailed outline is given to the ideas and needs of magnetic storage as well as the various experimental techniques used throughout the thesis. Chapter 3 gives an overview of the sources of anisotropy and how perpendicular magnetic anisotropy arises. Chapter 4 outlines a study in which we determine the value of the interfacial anisotropy for the CoFeB/Pd interface (320 $\mu J/m^2$). CoFeB is an amorphous alloy that has found wide use in in-plane magnetic tunnel junctions and is a promising candidate for magnetic tunnel junctions with perpendicular magnetic anisotropy. Magnetic tunnel junction electrodes with perpendicular magnetic anisotropy can help reduce the critical current density for spin-transfer-torque switching. These devices will find use in spin-transfer-torque magnetic random access memories. The phenomenological volume and surface contributions to the perpendicular anisotropy in the CoFeB/Pd system is determined. We also find an induced moment of 0.63 μ_B on the first monolayer of Pd atoms.

Chapter 5 explores the modification of perpendicular magnetic anisotropy using electric fields. We use a novel device design in which highly doped silicon is used as a gate and thermally grown SiO_2 is used as a dielectric. Subsequent insulator/ferromagnetic layer deposition allow us to modify the electron density at the insulator/ferromagnet interface. The application of an electric field is investigated in several systems, MgO/Fe/Pt, MgO/CoFeB/Pt and MgO/CoFeB/Pd. Chapter 5 builds on the anisotropy information obtained in Chapter 4. We find that it is possible to modify the perpendicular magnetic anisotropy in the MgO/CoFeB/Pd and the MgO/CoFeB/Pt system by applying an electric field. In the unannealed MgO/CoFeB/Pd system a positive gate voltage increases the perpendicular anisotropy, whereas in the annealed MgO/CoFeB/Pt system a positive gate voltage decreases the perpendicular anisotropy. The effect is larger in the case of annealed Pt capping.

Finally in Chapter 6 we modify the magneto-elastic anisotropy by using light ions to relieve stress at the Co/Pt interface in multilayer systems. Using a state-of-the-art He^+ ion microscope we magnetically pattern Hall bar structures. We strongly modify the perpendicular anisotropy at fluences between 10^{15} and 10^{16} ions/cm^2. We show that we can modify the anisotropy axis to an extent that out-of-plane magnetisation is no longer stable at zero field and the remanence goes to zero. This is a result of the ion-beam induced damage which allows the magneto-elastic stress to relax and a fall in anisotropy is observed. This result differs from previous literature reports on ion-induced damage in the fact that the beam is localised to a spot size of below 16 nm^2. We also observe surface sputtering of Pt with the ion-beam and determine the relationship between sputtered material and exposure dose.

Appendices at the rear of the text are included for tools used for the experimental work and are included for knowledge transfer.

Acknowledgements

"Experiments should be reproducible..... but life is never reproducible"
- H. Kurt

First and foremost, I have to acknowledge and thank Prof. Mike Coey, not only for the wonderful opportunity to study in his laboratory but also for allowing me to travel during the course of my study. An appropriate quote would be "Ciarán is the most well-travelled, under-published student I've ever had". It goes without saying that without his support I would not be able to do my experiments, to use the range of equipment I have been able to, to collaborate with the people I have collaborated with, or to be as responsible as I was (especially in all those CRANN cleanroom meetings).

My deepest thanks to the Group, who have been a very supportive bunch. Almost everybody has contributed to this thesis, in the form of either scientific measurements or discussions.

I have made some great friends here and worked with some amazing people. Peter Dunne has always been a good laugh and good support, he has been here from the start and is still here at the end. If I ever did anything bad, he would point it out, anything good, he would try to make me feel bad. There is no greater quote for true friendship than "its always great when you're someone else's drunken mistake".

I thank Dr. Karsten Rode for his advice on both science and life, I haven't made up my mind which I think he's better at advising in but he is certainly useful for either. He has pushed me to work and think scientifically for myself, while simultaneously distracting me with breaks where we would enjoy the sunshine and a beer. We also did a lot of 'labouring' when we moved to CRANN and are self certified tradesmen. He has been extremely helpful with discussing the theoretical aspects of my experimental thesis. Dr. Huseyin Kurt, whom with I also have fond memories of general tradesmanship, has been essential in focusing me to write this with his constant questioning "Have you written your thesis yet?". He has also been an excellent help in the cleanroom and has improved the Shamrock by a more than a few μTorr in pressure. His practical knowledge is also second to none. Dr. Kaan Oğuz, has become my fondest Turk of all. I remember (hazily) a night of Raki, and (fondly) all those trips we made, Strasbourg, Nancy, York, Washington D.C., Juelich. He has always been a good friend, and I suppose he should have a medal for putting up with my racial abuse for four years. I don't know how many times

we have pulled apart the Shamrock and put it back together, or fixed things around the lab. He is henceforth forgiven for his snoring when we shared rooms.

Our office in CRANN (L4.22) has been a great place to sit, I will really miss it. Huseyin Tokuc has always cheered my up by asking for money *after* offering me one of his biscuits, he is always on hand to help in the lab. Darragh Crotty, apart from being a target for my air powered shotgun, has often accompanied me on hazy nights which end pleasantly in some shape or form. I apologise to him for all those times I promised to help with collecting acetone from HazMat and turning up after 10 am the next day. Dr. Cathy Boothman would often join us on nights out and subject us to wave after wave of verbal (and more painfully, physical) abuse. Myself and Franklyn Burke have often discussed (at lenght) the trials and tribulations of a simple man's life. I'm sure we will both miss our window seats to Pearse St. I wish him all the best wherever he goes. I thank Simone Alborghetti for his friendship and advice over the years. I am sure we will meet again. To the others (past and present) in the office, Dave, Sasha, Guoqiang, Lorenzo, Kevin, Greg, Ed, Quinli Ma, James, Jose and Stephen.... you guys made the office what it is. I will miss you.

In the SNIAMS lab, clockwise from the left, Dr. Plamen Stamenov was very much an inspiration for his superior intellect and love of heavy metal. Megadeth will be happily remembered in the O_2. He has always been ready (and patient) to answer any questions I have relating to physics. Venky (Dr. M Venkatesan), from day one "just staple the receipts together and submit" to the finals, always commenting on my life and wondering about girls I was seeing, and even calling one Rusty. He has done all the SQUID measurements in this thesis. Dr. Zhu Diao, has always been, in my mind, a very smart and capable guy. We have broken bread in Burger King many a time (how he ate so much though I do not know). He is a very kind and gentle person, except perhaps when one is writing ones thesis. He conducted the AFM/MFM scans for the helium ion project.

Dr. Robbie Gunning, who had all but written his PhD when I arrived, is the one who single handedly has probably brought out the worst in me in terms of general mayhem, I have many fond memories of ******* on **** in the ***, or ******* off the roof of ******, or even drinking in the *********. Dr. Fiona Byrne, probably (definitely) got far to much abuse from me over the 4 years, but seemed to take it quite well. Lately she's been very nice at giving lifts since I now, like her, live in the "ghetto". Peter already got a mention but he gets another one. Dr. Jonathan Alaria and Marita, I remember making jokes with Jon that Marita was just the right height for him, before she arrived for a PhD, so partially I will take credit for their subsequent marriage. I also forgive his choice of county colours, navy and sky blue all the way. For the electrochemistry corner I thank Damaris for her friendship and Lorena for entertaining all my Argentinian "facts". To the new souls, Karl and Hongjun the best of luck with your stuff.

My thanks to Dr. Sebastiaan van Dijken, Dr. Gen Feng and Dr. Emma Kerr for their

help when I started and showing my the heart of the Shamrock. Niizeki-sensai (Dr. Tomohiko Niizeki... oo-oo-oo) has always been counted in the good books on the fact that his is in fact Japanese, he has given much insight to the Japanese way of thinking, how the scientific world should really operate and how quickly a person can pick up cursing at the same level as a Dub. Dr. Greg Malinowski (now supernova) worked with me before he left for greener pastures, I enjoyed many trips and social interactions. Greg showed me good friends are honest and tell you when your journal club talk was "really terrible". Guinness with him, Sebastiaan and Chris Murray is fondly remembered. Chris has made me realise that just because you're forty and have a family and kids doesn't mean you cant still be funny. My love of safety and rules can thoroughly be blamed on him, and I am ever thankful for it!

Dr. Adriele Prina-Mello has always been a sound advice giver and I have to thank him for that, his bike has allowed me to reach my top speed of 52 kph under my own energies. Dr. Jiafeng Feng I have enjoyed talking to about non-scientific related things, even though sometimes I would lose my scientific temper. Dr. Gavin D'Arcy, what can you say he is a culchie. I'll never forget the first thing he said to me, a dirty joke about wellies. Dr. Colm Faulkner, good to work with but also good to have fun and socialise with. He always pushed in the right direction, pointed out the errors of my ways and commended my good decisions. Dr. Byong-Sun Chun has also shown me that I should make my own scientific path, and he always assured me "one day is ok!". Dr. Mohammed Abid has also taught me to be scientifically independent.

I have had a total of four summer students, Yvan, Debanjan, Nicolas and James. They were all kind people, some were good at experiments, some at theory. I hope the former stick to experiments and the latter to theory, but I also hope that they follow their dreams and be whoever they want to be.

To my close and loyal friends; Aidan, Fisher, Phil, Sean, Keogher, Caroline, Conal, Aoife, Ciara. Without you guys I would probably be taking life too seriously, not enjoying myself and have a fully functional liver :) I acknowledge your great wisdom in life, your ability to listen and above all your asking about my thesis work even though you never really wanted to know the answer. Thank you all for your kindest support and crushing low blows. I will never forget 2009 and its all your fault!

I thank Rustu for her support when I started and her random phone calls when she returned to Japan. She was and still is a dear friend, and who I now will rely on for all of my Labview programming.

To my every loving family, who put up with me forgetting all important dates and helping me out when I needed it, for telling me to buy new clothes, shave and get my hair cut. My father has, much to my own astonishment, been a great influence in being able to separate personal and professional life. He always said the cost of complaining is proposing something better and

that in itself has helped me solve a lot of problems. They say you are always a baby in your mothers eyes, I think that is especially true for me. Even though she never understood what I do, despite my attempts to explain, this work is dedicated to her and the rest of my family. My sister especially has put up with me for quite long enough. Hopefully in the near future I can repay them all their kind love. My aunt Josephine deserves a special mention. I've sent her letters from every conference and sure as hell she's going to get this oversized door stopper in the post! All of my extended family have been extremely supportive.

I suppose it is normal to forget some people writing this acknowledgement section, so in that case there should be some sort of broadbeam apology to those who are not mentioned. I've met far too many people over the last five years to remember but I like to think that they somehow affected me, so for all you forgotten souls, thank you for knowing me. Everyone has contributed in some way to the person I am today.

Officially I acknowledge Dublin City Council for fees and maintenance through the Higher Education Grants Scheme. Emission Zero is acknowledged for nullifying my carbon footprint from flights to conferences over the last five years, making this a carbon neutral thesis. This work was conducted under the framework of the INSPIRE programme, funded by the Irish Government's Programme for Research in Third Level Institutions, Cycle 4, National Development Plan 2007-2013. This work was also was supported by Science Foundation Ireland under the MANSE contract 05/IN/1850.

Finally a special thanks to Miléna. For her constant insistence that I work on my thesis. She has shown me most of my own country, for a city boy I've been outside the Pale too much. Hopefully we will see a lot more together in the future.

Contents

List of Figures

Chapter 1

Introduction

"Just write your thesis and get on with your life"

- Dr. Alina Deac

1.1 Magnetism and Man

Naturally occurring magnetism has existed since long before Man walked the earth. Engineered magnetism, however, is relatively new. The applications of magnetism and magnetic materials has grown from a simple compass for navigation, to the creation of the electric motor, to modern day magnetic storage. The density of magnetic storage has increased alongside processors to the point that a standard hard drive has a capacity in excess of 500 GB. This information is all stored magnetically on a rotating 3.5 inch wide disk. About a hundred individual magnets are used for every "bit" of information. One byte is eight bits. That means for a 1 terabyte (1 TB) hard drive the number of individual magnets is around 800,000,000,000,000. The increase in hard drive storage has been due to material improvements, design changes in read/write head technology and changes to the way data is stored on the drive media. A graph of retail hard drive capacity versus production year is shown in Figure 1.1. As can be seen from the figure the capacity has grown exponentially with time. Here we will introduce the technology of today as well as the technology of tomorrow which will, hopefully, allow for increasing capacity in the

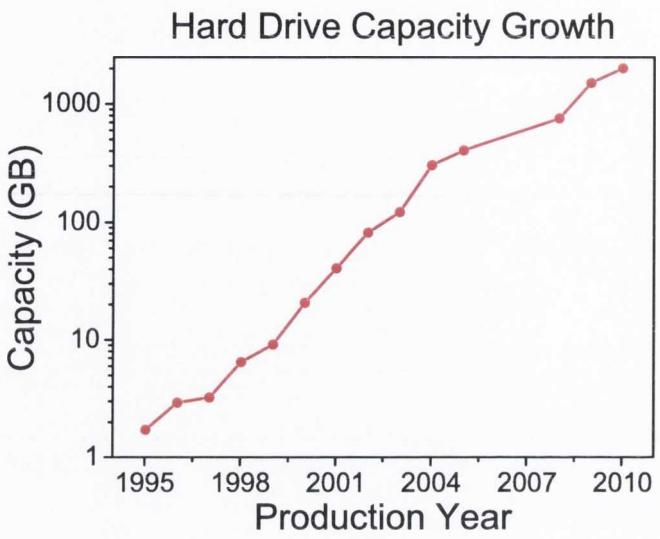

Figure 1.1: Hard drive capacity versus year. Note: the y-scale is logarithmic

coming years.

1.2 Magnetic Storage

Lets try to imagine how we store magnetic information on a disk. Imagine a cylindrical magnet with a well defined easy axis along its length, with magnetisation pointing either parallel or antiparallel to the axis. Now imagine a disk with several of these magnets with their easy axes perpendicular to the plane of the disk. The magnetisation can point parallel or antiparallel to the plane of the disk. The two stable magnetisation directions are both stable and they can be used to store binary ones and zeroes. When the magnetisation is parallel we can call this a "1", when antiparallel we can call this a "0". By sensing the stray field direction it is possible to determine whether a "1" or a "0" is stored. We use the phenomenon of magnetoresistance to sense the stray field from the hard disk. Although this is an oversimplification it is sufficient for realising that the magnetic stray field from the disk is an essential component of magnetic storage.

1.2.1 Data Reading

Magnetic materials display a dependence of their electrical resistance on the relative alignment of applied magnetic field to the current direction. This is called anisotropic magnetoresistance (AMR) [1]. The electrical resistivity varies as the cosine squared of the angle, θ, between the applied current and the applied magnetic field. The maximum change in resistance is given when the current and magnetic field are orthogonal. The effect is usually of the order of 1%. For modern magnetic storage, reading of magnetic information on the hard disk began with thin film AMR sensors but then proceeded to giant magnetoresistance (GMR) [2] and tunnel magnetoresistance (TMR) [3] [4] sensors. These devices consist of two magnetic layers (a few nm thick) separated by a metallic (GMR) or insulating tunnel barrier (TMR) spacer. The electrical resistance of these devices varies based on the cosine of the angle, θ, between the magnetisations of both magnetic layers. The GMR/TMR effect is much larger than the AMR signal. The maximum change of resistance is given when the magnetisations are opposite. Usually one layer is *fixed* and the other is *free*, the free layer is the sensing layer and its magnetisation direction responds to the stray fields from the recording medium [5] [6] [7]. The fixed layer is used as a reference and does not respond to the stray field from the recording medium. The GMR effect is of the order of 10% whereas the TMR effect is of the order 100%. The response due to external field for AMR and GMR/TMR read heads is shown in Figure 1.2 (a) and (b).

1.2.2 Data Writing

Write head technology has also progressed (see Figure 1.2 (c) and (d)). In longitudinal recording the magnetisation lies in the plane of the disk. The data was written using the stray field from a gap in a tiny electromagnet in the write head. The stray field from a gap in a ring electromagnet has a large component in the longitudinal direction. In order to increase the areal density, research was performed on materials where the magnetisation pointed in the perpendicular direction. If the magnetisation is perpendicular to the plane we can have higher recording densities than if the magnetisation is in-plane [8]. The shift to perpendicular record-

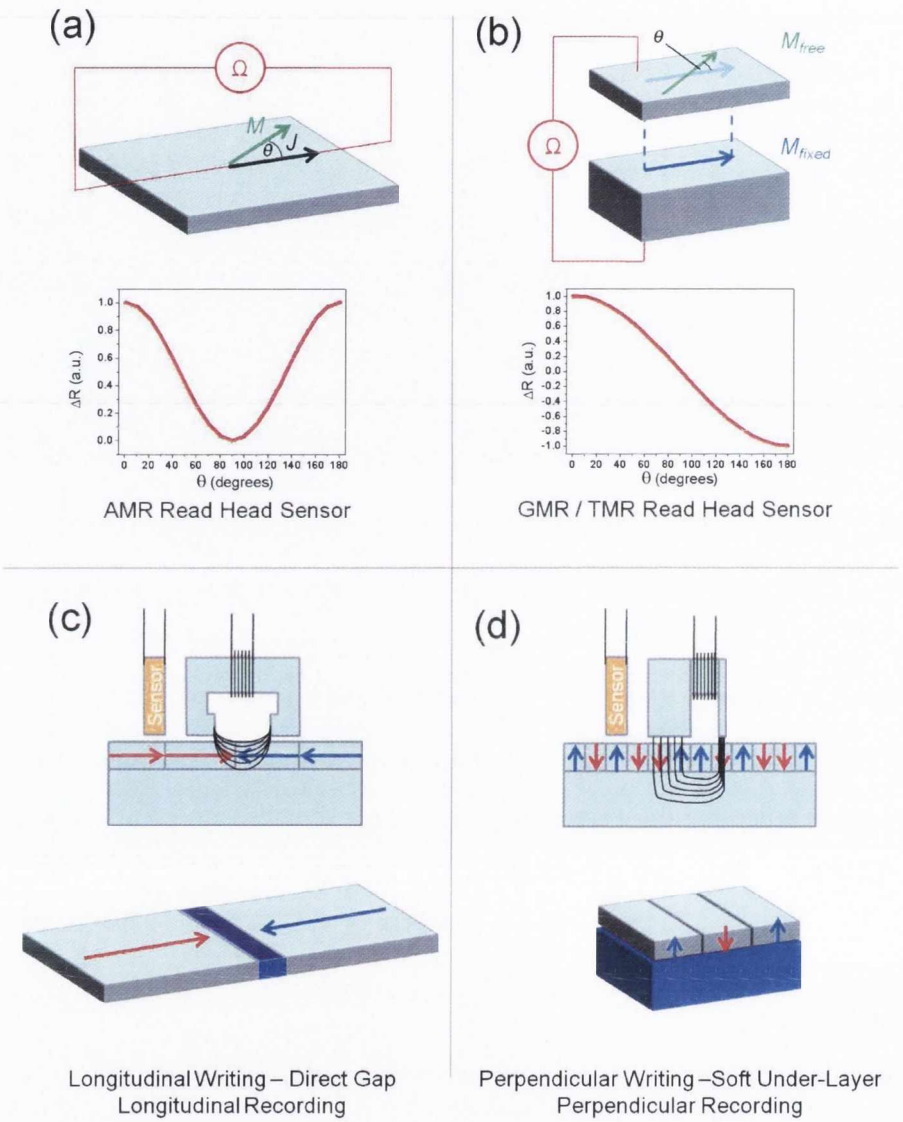

Figure 1.2: Schematic of the different responses to external field for AMR (a) and GMR/TMR (b) type read heads, and of the differences in longitudinal (c) and perpendicular (d) recording medium and writing technologies.

ing impacted the way data was written also. With perpendicular recording a magnetically soft underlayer (SUL) is used to place the recording medium directly in the pole piece gap (see Figure 1.2 (d)). The SUL allows the flux to be concentrated in the media directly under the write pole, the large return pole at the rear of the head spread the flux so as not to disturb any data already written. In order for data to be retained over a long time the recording material must have a large anisotropy (see chapter3). Materials with large anisotropies require more field to switch the magnetisation. The perpendicular write head has a very large field component in the perpendicular direction. As a result of these material and design improvements, the latest generations of hard drives utilise high anisotropy CoCrPt granular systems to store magnetic information [9] [10]. These CoCrPt-based media have high perpendicular magneto-crystalline magnetic anisotropy, are highly orientated and have high thermal stability.

1.3 Towards the Future

All the previous advances are responsible for the current areal densities of about 200-300 gigabits per square inch (Gb/in^2). The current obstacle is the fact that many individual granular domains, which all collectively are written and read as a whole, are required to store one bit of information. The grains have an average size but they are not identical or arranged in any periodic manner nor do they share the exact same switching fields. Although each grain has the potential to be a single bit, this is not the case in current hard disk drives. Information is written to a disk and read back at a fixed frequency. That is, the information is integrated over time. Stored data is detected in the magnetisation sampling time. Although earlier we have said that the magnetisation direction stores information, this is an oversimplification. In reality the stored data is detected in the stray field at domain walls between grains of opposite magnetisation. What is read back is if the magnetisation changed within the sampling time. As such, the information is encoded in the changes in magnetic topography: a region of uniformly magnetised grains represents a string of zeroes, whereas the region of up and down magnetised grains represents a string of ones. An excellent review of hard drives and how they work is given in

Ref. [11].

The main point to note from this is that in the current scheme the *read/write head defines the data track*. For the future it would be advantageous to use a *predefined track*, so instead of using many grains for storing one bit we can use one grain to store one bit. This gives an automatic increase in storage density. This has an associated problem in that the medium properties are under more strict control when a single magnet is used as a bit. In the current read/write scheme the many grains forming one bit are slightly different shapes and have a switching field distribution. The distribution in the grains allows for somewhat more relaxed writing because the data is read back over the entire volume.

Currently, the granular technology that we are currently using has an areal density limit below 1 Tb/in^2. The perpendicular magnetic grains are about 10 nm wide and 30 nm high. The roadmap for beyond 1 Tb/in^2 is under experimental investigation [12] and thinking beyond 10 Tb/in^2 has already begun [13].

In order to increase the density towards 1 Tb/in^2 several approaches have been proposed, bit patterned media [14], [15], multistate memory [16] [17], heat-assisted [18] or energy assisted [12] magnetic recording but also there is room for "something we haven't thought of yet" [19]. There is also the possibility of using more than one of these proposed techniques [20].

In the case of bit patterned media in particular, a greater control over the switching field distribution is required. Also, for smaller bits the anisotropy must be high in order for the thermal stability to be high. The drawback however is that the higher the anisotropy energy the larger the coercivity, meaning that we are required to apply more field to switch the magnetisation of the medium.

The physical property of concern when designing magnetic mass storage devices is the magnetic anisotropy. A magnetic particle must have sufficiently high anisotropy for it to retain its magnetic properties as it is scaled down to sub-100 nm scales, and also to retain its information over a number of years. This constraint is generally formulated as $K_{eff}V > 60\mathrm{k_b}T$, where K_{eff} is the anisotropy energy, V is the grain volume, $\mathrm{k_b}$ is Boltzmann's constant and T is the operating temperature [21].

The superparamagnetic limit [22] places an upper limit on hard disk drive recording density. The size of one bit is determined by the energy barrier in relation to the temperature. If the thermal energy at room temperature (or operating temperature) is too close to the magnetic energy, $K_{eff}V$, then the magnetisation will behave like a paramagnetic particle and lose its hysteresis. This means that, over time, a magnetic bit encoded as "1" can become a "0". Obviously this is no good for long term data storage.

In order to be useful, a medium must have high enough anisotropy so the magnetisation won't change over time, but low enough that it can be switched with low power. Each bit should also be the same, in so far as the switching field distribution should be so narrow that write errors do not occur and also the write process does not disturb neighbouring bits. Unlike the granular medium we no longer have the luxury of averaging over many grains. Most important for industrial roll out (and least important for research) is the end cost to integrate the system into current manufacturing processes.

In order to store information magnetically in smaller and smaller volumes it is necessary to first obtain totally independent magnetic volumes that can be treated as identical individual bits. Long range order with resolution on the nanometer length scale is one problem to be solved for bit patterned media to come to fruition. If long range order is established then the issue of magnetic diversity still exists. Isolated nano-pillars with the same nominal dimensions can have a distribution in switching fields and anisotropy. The patterning process used to obtain these islands can modify the coercivity and switching field distribution [23] [24].

There are two methods available for patterning discrete islands; physical separation of each island i.e. an array of independent nanopillars [15] ; or simply magnetically separating bits in a physically continuous medium i.e. to have a continuous medium composed of ferromagnetic islands in a continuous paramagnetic medium [25].

Modifying the anisotropy using electric fields is also a possibility for lowering the switching field [26] [27]. This would allow for electric field assisted switching in traditional systems, and also dynamic switching using high frequency voltage pulses and magnetic tunnel junctions [28] [29].

The successful engineering, control and modification of magnetic properties or perpendicular media is important for the future scaling of hard drive storage to higher and higher areal densities. In this thesis we investigate perpendicular anisotropy in thin films, including the influence of an electric field. We also explore a new method of modifying the anisotropy of magnetic thin films - irradiation in the helium ion microscope.

In Chapter 2 we cover the experimental techniques used for film and device fabrication and characterisation. In Chapter 3 we discuss the physical origin of the perpendicular magnetic anisotropy we aim to modify. Chapter 4 describes the experimental investigation of PMA in the CoFeB system. In Chapters 5 and 6 we discuss the modification of the magnetic anisotropy. Chapter 5 concerns the reversible control of the magneto-crystalline contribution to the interfacial anisotropy in different systems. We use an electric field to modify the electronic density at a ferromagnet/insulator interface and gain control over the anisotropy energy.

Chapter 6 discusses the irreversible control over stress induced anisotropy by light ion-irradiation using a *focused* beam. A beam of He^+ ions allows us to *locally* modify the perpendicular magnetic anisotropy in Co/Pt based multilayers. Chapter 7 draws the main conclusions from the work presented and ideas for future work related to the various projects.

Appendices in the rear of this Thesis comprise a manual for thin film processing and measurement, and represent the acquired knowledge on the experimental tool set used through the thesis work.

Bibliography

[1] McGuire, T.R., Potter, R.I. *IEEE Transactions on Magnetics* **MAG-11**(4), 1018–1038 (1975).

[2] Baibich, M.N., Broto, J.M., Fert, A., Van Dau, F.N., Petroff, F., Eitenne, P., Creuzet, G., Friederich, A., Chazelas, J. *Physical Review Letters* **61**(21), 2472–2475 (1988).

[3] Moodera, J.S., Kinder, L.R., Wong, T.M., Meservey, R. *Physical Review Letters* **74**(16), 3273–3276 (1995).

[4] Julliere, M. *Physics Letters A* **54**(3), 225–226 (1975).

[5] Leal, J.L., Oliveira, N.J., Rodrigues, L.M., Sousa, A.T., Freitas, P.P. *IEEE Transactions on Magnetics* **30**(6 pt 1), 3831–3833 (1994).

[6] Lin, Chien-Li, Sivertsen, John M., Judy, Jack H. *IEEE Transactions on Magnetics* **30**(6 pt 1), 3834–3836 (1994).

[7] Parkin, S.S.P., Kaiser, C., Panchula, A., Rice, P.M., Hughes, B., Samant, M., Yang, S.-H. *Nature Materials* **3**(12), 862–867 (2004).

[8] Bertram, H.N., Williams, M. *IEEE Transactions on Magnetics* **36**(1 PART 1), 4–9 (2000).

[9] Wood, R. *Journal of Magnetism and Magnetic Materials* **321**(6), 555–561 (2009).

[10] Wood, R., Hsu, Y., Schultz, M. *Hitachi Global Storage Technologies White Paper* (November 2007).

[11] Hayes, B. *American Scientist* **90**(5), 212 (2002).

[12] Stipe, B.C., Strand, T.C., Poon, C.C., Balamane, H., Boone, T.D., Katine, J.A., Li, J.-L., Rawat, V., Nemoto, H., Hirotsune, A., Hellwig, O., Ruiz, R., Dobisz, E., Kercher, D.S., Robertson, N., Albrecht, T.R., Terris, B.D. *Nature Photonics* **4**(7), 484–488 (2010).

[13] Yuan, Z.-M., Liu, B., Zhou, T., Goh, C.K., Ong, C.L., Cheong, C.M., Wang, L. *IEEE Transactions on Magnetics* **45**(11), 5038–5043 (2009).

[14] Hellwig, O., Hauet, T., Thomson, T., Dobisz, E., Risner-Jamtgaard, J.D., Yaney, D., Terris, B.D., Fullerton, E.E. *Applied Physics Letters* **95**(23), 232505 (2009).

[15] Hellwig, O., Bosworth, J.K., Dobisz, E., Kercher, D., Hauet, T., Zeltzer, G., Risner-Jamtgaard, J.D., Yaney, D., Ruiz, R. *Applied Physics Letters* **96**(5) (2010).

[16] Parkin, S.S.P., Hayashi, M., Thomas, L. *Science* **320**(5873), 190–194 (2008).

[17] Jeong, W.-C., Lee, B.-I., Joo, S.-K. *Journal of Applied Physics* **85**(8 II A), 4782–4784 (1999).

[18] Kryder, M.H., Gage, E.C., Mcdaniel, T.W., Challener, W.A., Rottmayer, R.E., Ju, G., Hsia, Y.-T., Erden, M.F. *Proceedings of the IEEE* **96**(11), 1810–1835 (2008).

[19] Terris, B. *Gordon research conference* .

[20] Kikitsu, A. *Journal of Magnetism and Magnetic Materials* **321**(6), 526–530 (2009).

[21] Weller, D., Moser, A. *IEEE Transactions on Magnetics* **35**(6), 4423–4439 (1999).

[22] Brown, W.F. *Physical Review* **130**(5), 1677–1686 (1963).

[23] Kitade, Y., Komoriya, H., Maruyama, T. *IEEE Transactions on Magnetics* **40**(4 II), 2516–2518 (2004).

[24] Devolder, T., Chappert, C., Chen, Y., Cambril, E., Bernas, H., Jamet, J.P., Ferré, J. *Applied Physics Letters* **74**(22), 3383–3385 (1999).

[25] Chappert, C., Bernas, H., Ferré, J., Kottler, V., Jamet, J.-P., Chen, Y., Cambril, E., Devolder, T., Rousseaux, F., Mathet, V., Launois, H. *Science* **280**(5371), 1919–1922 (1998).

[26] Weisheit, Martin and Faehler, Sebastian and Marty, Alain and Souche, Yves and Poinsignon, Christiane and Givord, Dominique. *Science* **315**(5810), 349–351 JAN 19 (2007).

[27] Zhou, T., Leong, S.H., Yuan, Z.M., Hu, S.B., Ong, C.L., Liu, B. *Applied Physics Letters* **96**(1), 012506 (2010).

[28] Maruyama, T. and Shiota, Y. and Nozaki, T. and Ohta, K. and Toda, N. and Mizuguchi, M. and Tulapurkar, A. A. and Shinjo, T. and Shiraishi, M. and Mizukami, S. and Ando, Y. and Suzuki, Y. *Nature Nanotechnology* **4**(3), 158–161 (2009).

[29] Chiba, D., Nakatani, Y., Matsukura, F., Ohno, H. *Applied Physics Letters* **96**(19), 192506 (2010).

Chapter 2

Deposition, Fabrication and Measurement Methods

*"Just because its impossible, don't let **that** psyche you out!"*

- Inspirational words from above

2.1 Introduction

This chapter will outline the various experimental techniques used in the fabrication of devices found in subsequent chapters. It will cover: Fabrication (sputter deposition and wafer dicing); Lithography, both physical (UV lithography, ion milling) and magnetic (focused ion beam); and Characterisation (extraordinary Hall effect, x-ray diffraction, SQUID magnetometry).

2.2 Fabrication

2.2.1 Sputter Deposition

Sputtering is a physical vapour deposition technique which allows the deposition of metals and insulators. It is currently a preferred industrial deposition technique and finds applications from the fabrication of hard drive platters to protective coatings on drill bits and even the aluminium

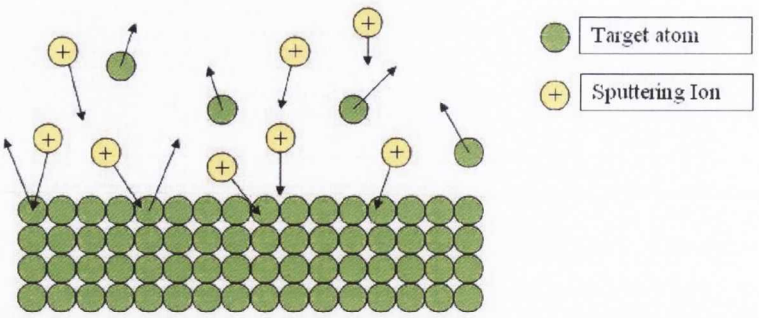

Figure 2.1: DC Sputtering process; when energetic ions strike the target surface they can eject target atoms.

foil deposition on the inside of crisp packets.

Sputtering involves the physical ejection of an atom from the surface when it is struck by another atom. This is generally accomplished by means of a plasma (see Figure 2.1). The ejected target atoms will condense on a nearby surface, either the chamber walls or a substrate. The energy that a target atom will have when it reaches its destination will be determined by its initial energy and the number of collisions it undergoes. It is therefore possible to control the energy of the sputtered atoms by adjusting the deposition conditions such as power and pressure. Adjusting the pressure will affect the mean free path, and control the energy of the sputtered atom when it reaches the substrate. This allows control of the film properties based on deposition conditions [1]. The more energy the atoms have when deposited the more they can reorganise themselves on the surface. By altering the substrate temperature we can also alter, through thermal expansion, the lattice constant and introduce strain.

The plasma is created by applying a large enough potential (higher than the ionization potential) across a gas in a vacuum chamber. In the simplest case the target is the cathode and the substrate is the anode. Figure 2.2 gives an overview of the process. Positively charged atoms in the plasma will be accelerated towards and impact on the negatively charged target surface. Upon impact the sputtering ion will undergo collisions and impart its energy to the target. If this energy is greater than the surface binding energy then a neutral atom can be ejected from the surface. The power supply on the left hand side of the figure supplies the necessary voltage

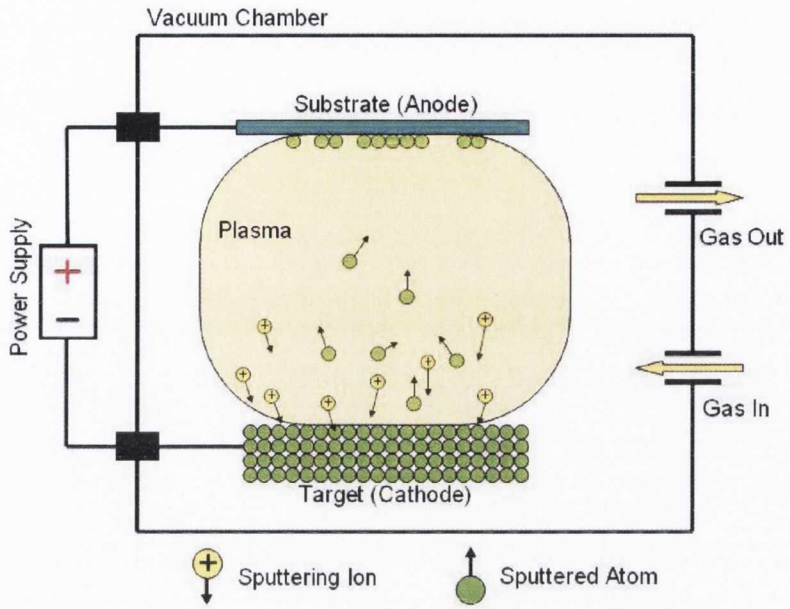

Figure 2.2: Sputtering process; ejected atoms from the target (cathode) are deposited on the substrate (anode).

to ionise the gas that is injected and extracted on the right hand side. The neutral atoms are not attracted to target nor substrate and simply travel in the direction they are ejected until they land either on the substrate or the vacuum chamber wall. They can change direction by colliding with other sputtered atoms or argon gas atoms. From this it can be seen that a higher deposition pressure will reduce the mean free path between these collisions. Therefore the target substrate distance, as well as the Ar gas pressure become important parameters in the sputtering process. Argon is an inert gas, and does not react chemically with either the substrate of the target material. Using other gases, it is possible to reactively sputter materials, for instance using an argon/oxygen or argon/nitrogen plasma, to form oxide and nitride species of the target material. Due to the fact that most ejected target atoms are neutral, it is obvious that the substrate is not required to be the anode. In order to attract ions the target must be negatively charged. This is the only requirement for sputtering in that charged ions impact on the target.

The power supply in Figure 2.2 is simplistically connected to the target and the substrate, in general this is not the case. Figure 2.3 shows a schematic of a magnetron sputter gun. The

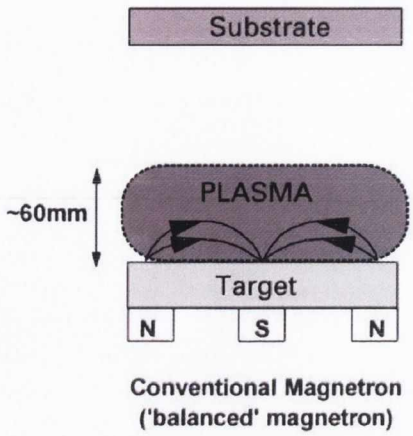

Figure 2.3: Schematic of a magnetron gun. Magnets under the target create an electron trap [2].

target is insulated from the sputter gun casing and the power supply applies a voltage between the target and the gun casing. A closed loop magnetic field is generated below the target material [2]. The magnetic field serves as an electron trap, confining the secondary electrons in a ring close to the target surface. Comparing Figures 2.2 and 2.3 we notice immediately that the plasma is confined near the target surface in the magnetron design. The increased density of the plasma in turn leads to increased deposition rates, as well as lower operating voltages and pressures. However since the electrons are now generally confined to a ring, the target efficiency is reduced. When the target is a ferromagnet, iron or cobalt for example, the magnetic field will be shielded by the target itself. If the field is not enough to saturate the material the flux will tend to pass through the target. Therefore the field from created must be large enough to saturate the target and allow the some stray field at the surface. It is therefore necessary for ferromagnetic targets to be thin, so that the flux generated by the magnet exceeds that required to saturate the target.

During reactive sputtering with oxygen, for example, the target surface will be oxidised. Oxides are generally insulating and will build up charge on the target surface. As soon as the charge exceeds the breakdown voltage, an arc will occur. An arc discharge can be thought of as a sudden burst in sputter power, this increased power will alter the growth rate and will generally give higher roughness in the deposited film. This excess charge must be neutralised to

have stable sputter parameters. It can be neutralised by reversing the target voltage for a certain time during the normal DC operation. This is accomplished using a DC pulser.

It is also possible to sputter purely insulating materials by radio-freqency (RF) sputtering. In this case the voltage on the target is alternated at a frequency of, typically, 13.5 MHz. RF sputtering requires an impedance matching circuit. The advantage of RF sputtering is that oxides and nitrides can be sputtered using only argon gas.

2.2.2 The Shamrock

The Shamrock is the sample preparation workhorse used for all the thin films featured in this thesis. It is currently located in the Class 10,000 deposition area of the CRANN cleanroom (CRANN L4.31). The Shamrock comprises two high vacuum, and one ultra high vacuum, process chambers. It also has a transport module (TM) containing a computer controlled robot for movement of wafers and a loadlock cassette module (CM). A schematic and corresponding photograph of the Shamrock tool is shown in Figure 2.8, the schematic represents an top-down view of the tool, whereas the photograph is a head on image. All samples were prepared on standard thermally oxidised silicon wafers. These wafers are either 110 mm in diameter and 525 μm thick, or 150 mm in diameter and 625 μm thick. Samples in this thesis are grown on the full 4" (110 mm) wafers or on diced chips 1" (25.4 mm) square substrates which were diced from 6" (150 mm) wafers. The 25.4×25.4 mm^2 dies were prepared using an Disco DAD 3320 automatic wafer dicer in the CRANN cleanroom chase (CRANN L4.39) as described in section 2.2.8. This dicing yielded sixteen 25.4×25.4 mm^2 chips which were then processed individually in the deposition facilities in the cleanroom.

2.2.3 Chamber A

Chamber A is the main process chamber and part of the original tool. The Shamrock found use in the sputtering of early thin film read heads for companies including Seagate. It contains 6 DC magnetron sputtering "S-Guns" used for metal sputtering and an ion mill for substrate

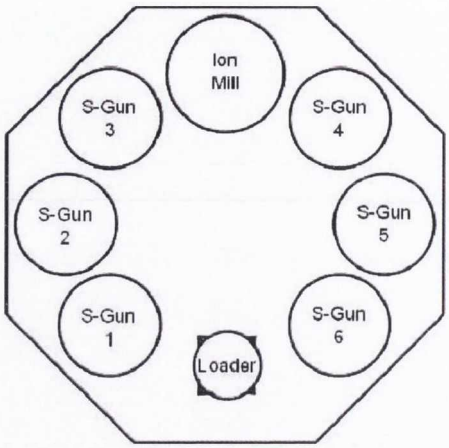

Figure 2.4: Schematic of chamber A

cleaning and gentle layer etching. Guns 5 and 6 are equipped with an extra coil for optional RF deposition. Gun 5 is also equipped with a gas injection ring for reactive deposition with O_2. Gun 6 is currently connected to the SparcLE DC pulser and is used for reactive sputtering of nitride films of copper and aluminium. It is possible to sputter uniformly on 4" and 6" wafers using only 3" sputter targets due to the unique planetary turntable rotation available in Chamber A of the machine. The planetary design also allows simultaneous processing of up to four wafers with uniform deposition. It does place a constraint on film thickness variations as the planetary motion means that the substrate is not always over the target. In order to deposit a uniform layer 11 revolutions of the turntable are necessary. At 44 rpm this means that 1 revolution takes 1.36 s. 11 revolutions take exactly 15 seconds. At typical deposition rates of about 0.01 - 0.02 nm/s, the thickness increase should be at least 0.15 - 0.3 nm to be consistent. A magnetic field of $\sim$ 10 mT can be applied during film deposition, using magnets surrounding the substrate, to induce an in-plane easy axis of magnetisation. The field is supplied by permanent magnets of the same variety supplying the field in the magnetron. They are clamped in place and can be removed as required, for example to help with the growth of amorphous rare-earth ferromagnets. The base pressure of the chamber is less than 8×10^{-8} Torr[1]. The substrates cannot be heated.

[1]The original part of the tool (Chamber A) is an American tool, therefore all pressures are measured in Torr, 1 Torr = 1.33 mbar = 133 Pa.

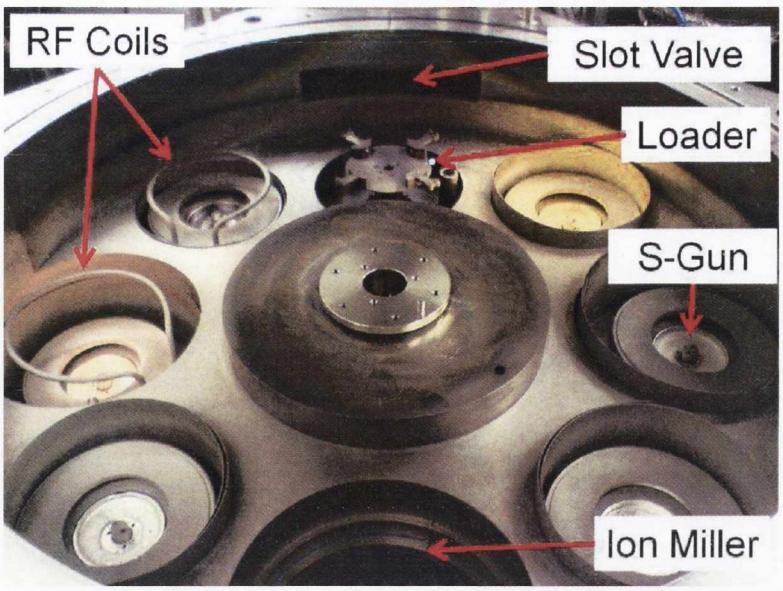

Figure 2.5: Chamber A of the Shamrock with the turntable removed, visible are the magnetron guns, RF coils (the O_2 injection ring was disconnected in this photograph).

In the S-Gun design a solid piece of iron causes the flux to be closed between the center of the target and the edge where a ring of permanent magnets generate the field. Typical sputter pressures are in the range of 10^{-3} Torr with cathode powers of 100 W for Chamber A. Turntable rotation is always set to 44 rpm. Typical growth rates of around 0.01-0.02 nm/s are calibrated by X-Ray reflectivity (XRR) (see section 2.4.1) measurements of a 30 minute deposition on SiO_2 chips. Ion milling in Chamber A is calibrated also by means of XRR and generally with the samples used for growth calibration. The ion miller is programmable and controlled remotely by the Shamrock software. There are two recipes stored in the controller itself, the difference between the two recipes is the accelerating voltage, 500 or 1000 V. The milling rates were calibrated and generally lie in the range of 0.001 to 0.015 nm/s at 500 V accelerating voltage. We tried both 500 and 1000 V and found that for 1000 V the film surface is rougher than for 500 V. Since we want to mill samples uniformly without dramatically changing the roughness we use only 500 V for milling. Typical milling cycles are 300 seconds etching followed by 300 seconds delay to prevent substrate heating. This gives uniform etch rates for Ta, Ru and Cu (typically etched materials). Further details of ion milling in Chamber A can be found in

Appendix B.3.

Growth rates are calibrated each time the chamber is vented and the targets are changed, and are generally consistent.

The Shamrock system is also equipped with a Sparc-LE DC pulser for the reactive sputtering of nitride films, such as aluminium nitride and copper nitride. The Sparc-LE pulser is used to prevent the build up of charge when oxide and nitride (both insulating) species. This is accomplished by reversing the target voltage to neutralise the excess charge before an arc can occur. The target voltage is reversed for 5 μs and is applied to the target every 50 μs. Films grown in pulsed DC mode will have few defects. This has been shown to be the case for Al_2O_3 films [3] where suppression of arcing led to a smoothing of the deposited film and also promoted stoichiometric Al_2O_3 growth. Details of nitride optimisation can be found in B.2. Nitride characterisation and optimisation was performed with the help of James Kally, a summer student from University of California, Santa Barbara during the summer of 2010.

Chamber A is controlled by an industrial OPTO22 MISTIC controller. A PC running Windows 3.11 is used to send commands to the MISTIC unit via token-ring ethernet. The use of the MISTIC controller allows redundancy for the PC which communicates to it. However the MISTIC controller itself has surpassed its industrial use and is no longer replaceable from suppliers. More details are given in Appendix B.

2.2.4 Chamber B

Chamber B is a custom designed chamber built by PLASSYS. It mates to the main Shamrock system through a gate valve mounted on the transfer module (TM). It contains 6 Kurt J. Lesker DC magnetron sputter cluster guns used for metal sputtering and co-sputtering alloy compositions, two RF target facing target (TFT) guns for sputtering insulators and an ion gun for plasma oxidation. A substrate heater allows for depositions at up to 700°C in specially designed Inconel holders. The substrate is not in direct contact with the heater and so in order to improve the heat transfer efficiency we sputter 100 nm of Ta on the backside of the substrate. This improves the infrared absorption of the substrate. The true temperature of the substrate is calibrated using a

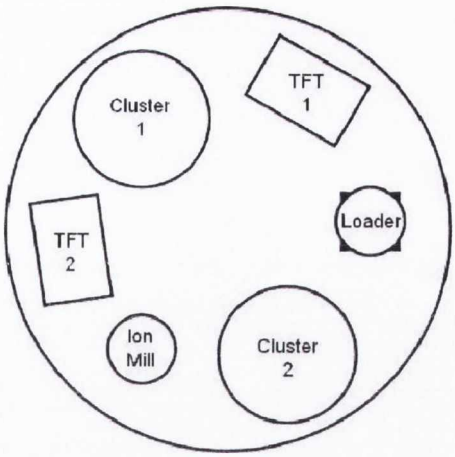

Figure 2.6: Schematic of chamber B

special substrate with thermocouple attached and we obtained calibration curves for substrate temperature versus heater temperature for both backside coated and non-backside coated substrates. Calibration was performed by Dr. Huseyin Kurt who also designed the thermocouple wafer holder used for calibration. Chamber B has a programmable interface based on the Microsoft .NET framework for automatic processing of a single wafer in the chamber, however that wafer must first loaded manually to the chamber. Details of this are given in Appendix B.4. The base pressure is less than 1×10^{-8} Torr. Typical deposition powers are 30-50W for DC cluster guns and 50-100W for TFT guns in Chamber B. Growth rates around 0.01-0.03 Å/s and are calibrated by X-ray reflectivity using fixed time depositions just as they are for Chamber A. The ion gun in Chamber B was found to be unsuitable for ion etching and appeared to only roughen the substrate surface whenever it was used. It can be used for oxidation of layers deposited in the system by sputtering. Within Chamber B there are also O_2 and N_2 gas lines for reactive sputtering. The Sparc-LE pulser is currently not connected to any sputter gun in chamber B but there is no reason why it cannot be connected in line with a gun in this system. The only difference is that a change of connector is required. The power connection to the Lesker guns in chamber B is a co-axial cable whereas the connection to the S-Guns in chamber A is two-core heavy duty mains cable.

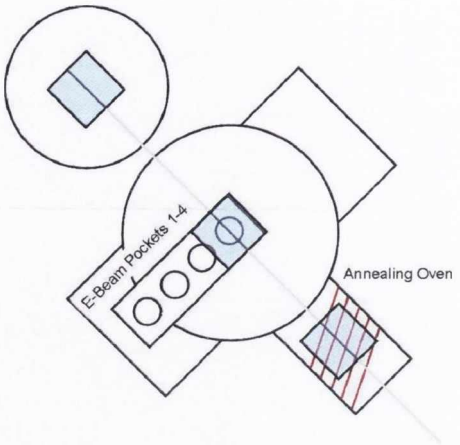

Figure 2.7: Schematic of chambers C and D

2.2.5 Chambers C and D

Chambers C and D form a custom designed ultra high vacuum e-beam evaporator system with one e-beam gun and four evaporation pockets. It was also built by PLASSYS. Chamber C is a transferring loadlock which rotates the wafer holder for handing off to Chamber D's transfer arm. Chamber D is the main process chamber. It houses the e-beam evaporator and a low pressure AJA magnetron sputter gun which can sputter in the range of 10^{-4} Torr using argon gas. There is no facility for reactive sputtering in Chamber D. The wafer transferring arm can also rotate so it is possible to process both sides of a silicon wafer in the Shamrock under vacuum. The wafer flipping facility can be used for processing samples grown on silicon nitride membranes. It also contains an annealing tunnel oven which is capable of heating substrates to 700°C. The annealing oven was designed to accommodate a permanent magnet for magnetic annealing, but at the time of writing it is still under construction in China. The base pressure of the system is less than 2×10^{-10} Torr. Similar to Chamber B, processes can be automated within the chamber using programmable software. The wafer must be loaded manually into Chamber C. Hand-off to Chamber D is automated. Sputtering, wafer flipping and annealing is fully automated, but e-beam evaporation is a manual process and requires the presence of an operator.

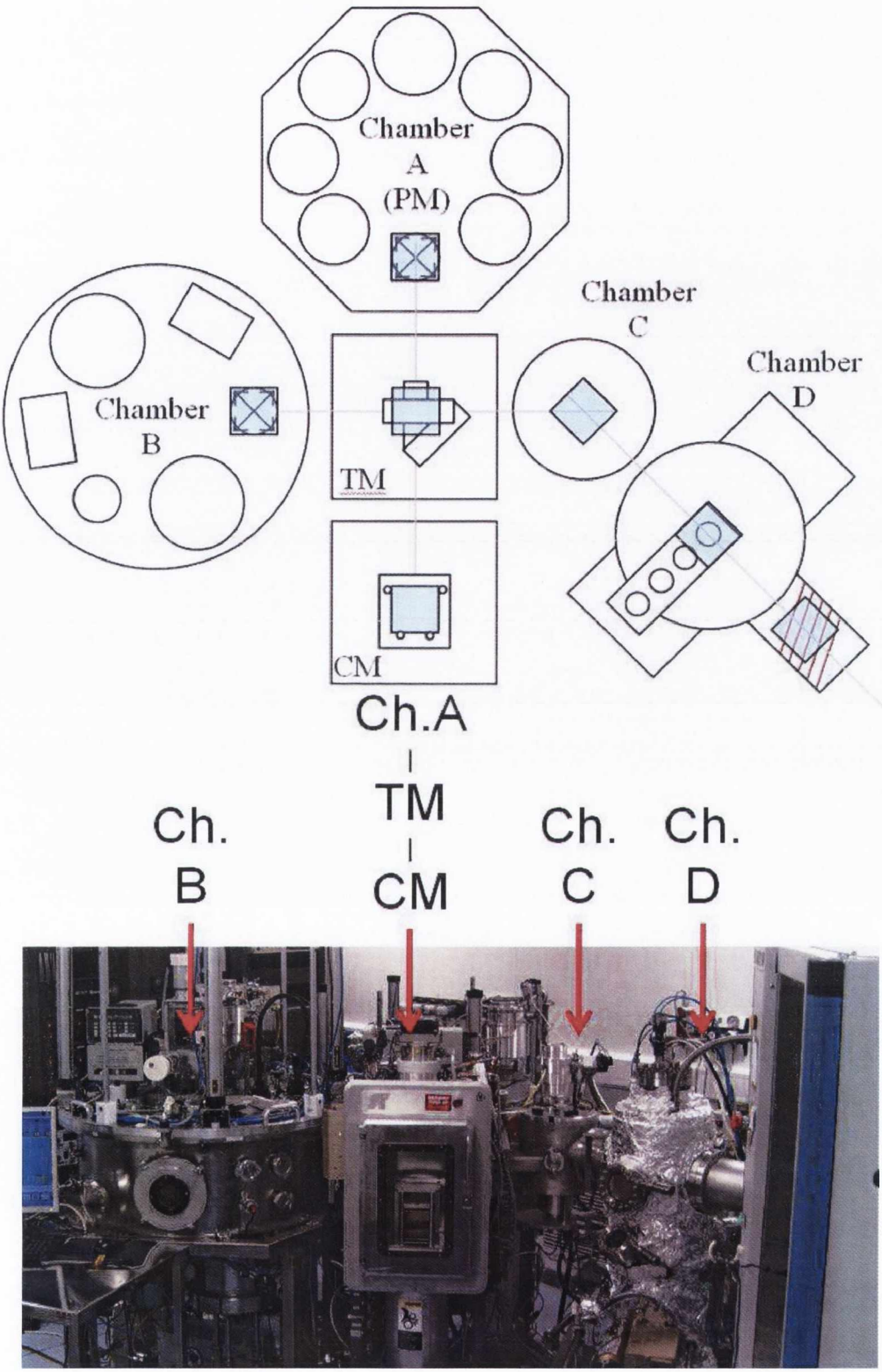

Figure 2.8: Schematic layout and photograph of the Shamrock deposition tool

2.2.6 Transport and Cassette Modules

The transport module (TM) is located at the center of the system and contains a computer controlled Genmark GB3 vacuum robot for wafer transport to either process module. It also contains a Cs thermal evaporation source. The base pressure is below 5×10^{-8} Torr.

The cassette module (CM) loadlock is capable of holding up to 16 wafers and has a base pressure of less that 2×10^{-7} Torr.

The wafer travel within the Shamrock system is depicted in Figure 2.8. The blue square is representative of a wafer contained within a wafer holder and the grey lines represent the movement of the wafer from chamber to chamber. The robot can be controlled automatically by the MISTIC controller which operates Chamber A, or manually via DOS command line in order to use Chambers B, C and D. A list of commands and their functions is given in Appendix B as are troubleshooting in cases of robot crashes. Since the manual control of the robot does not feature any interlocks it is possible to drive the robot into the chamber wall, a closed slot valve or a slot in the cassette which is already occupied. These crashes occur due to user error.

2.2.7 Shamrock Summary

In manual mode, the robot in the TM is capable of transporting wafers directly between process chambers with or without returning wafers to the loadlock. This versatile system allows for multiple sputtering, evaporation, milling, oxidation, flipping and annealing steps on multiple wafers without having to break vacuum. High temperature depositions and *in-situ* annealing are available and currently the only useful facility lacking on the Shamrock tool is *magnetic* annealing.

Software integration between the original system (CM/TM/Chamber A) and the custom chambers (B, C and D) is lacking. The feasibility of integration was investigated via PLASSYS and their software engineer David Loomes. It is possible to integrate the system fully, but it is a costly process and is not necessarily guaranteed to work.

2.2.8 Wafer Dicing

The Disco DAD 3220 is an automatic wafer dicer capable of dicing and scribing various substrates such as Si, MgO, STO. It was used for the preparation of 25.4×25.4 mm^2 chips for sputter deposition as well as extraction of Hall bars after patterning and ion milling (as described in section 2.3.1). The wafer dicer was also used in preparation of samples for magnetometry measurements. The ability to save programs on the dicer meant that all samples prepared by dicing are, for all intents and purposes, identical. The dicer is located in the CRANN cleanroom chase and a manual written by the author can be found in Appendix C.

2.3 Lithography

2.3.1 UV lithography and Ion Milling

In order to pattern sputtered magnetic thin films into useful devices, we employ a standard lithography technique which uses ultraviolet light to modify the chemical resistance of a polymer and allow exposed (or unexposed) polymer to be dissolved in a solvent. Such a pattern transfer technique is used for all the devices presented in this thesis. UV lithography allows for the patterning of devices down to 1 μm sizes. The procedure for lithography using a spin-on photoresist is shown in Figure 2.9. A more detailed review can be found in [4].

Wafer cleanliness and surface treatment are important considerations if one wants to accomplish extremely high resolution lithography. In general the following cleaning process is used; an ultrasonic acetone wash for two minutes followed by an isopropanol rinse for one minute and a blow dry in N_2. This will give a clean surface for photoresist dispensing. Additional cleaning steps can be employed depending on the substrate or process used. For instance, glass substrates are generally cleaned in Pirahna[2] solution before processing. Si wafers can be baked to remove water from the substrate surface. Adhesion promoters can be used (such as HMDS) to dehydrate the substrate surface. This ensures that the photoresist will bind to the wafer surface

[2] a mixture of sulphuric acid and hydrogen peroxide. 3:1 H_2SO_4 and dilute (30%) H_2O_2

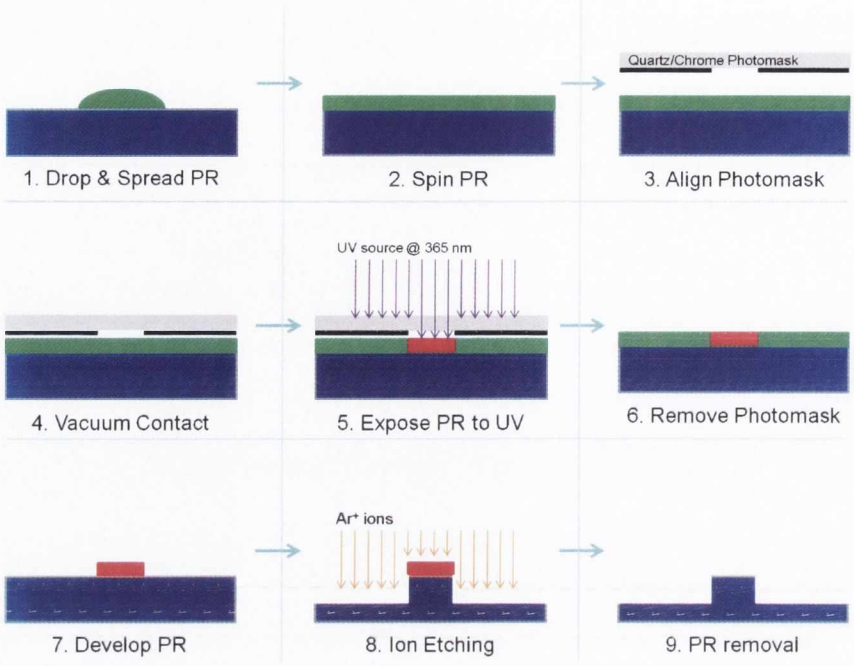

Figure 2.9: Steps involved in ultraviolet lithography patterning, described in detail in the text

rather than the water film.

Photoresist is a liquid suspension of a resin, a photoactive compound and a solvent. The solvent keeps the substance liquid and is driven out prior to exposure. The photoactive compound in the unexposed state inhibits the breakup of the resin in developer, in the exposed state the photoactive compound allows for the dissolution of the resin material.

The steps shown in Figure 2.9 are detailed below:

1. The photoresist (typically Shipley S1813) is drop cast and spreads on the substrate. The quantity dispensed is dependant on the size of the substrate. Too much resist will result in excess resist being spun off, too little will result in streaking/non-uniform coating of the resist. To uniformly coat a 150 mm (6" Si/SiO_2) wafer we dispense 1 mL of S1813.

2. In order to have a uniform layer of photoresist the sample is rotated at high speed around the film normal, the spin speed can be used to control the thickness of the photoresist layer. For high resolution lithography thin photoresists are more desirable so we can have uniform exposure over the entire substrate. Thickness variations can cause differences

in exposure dose, meaning that some areas will be under-exposed whereas other areas will be over-exposed. The thickness versus spin speed curve depends on the photoresist viscosity and, generally, photoresists are offered in a range of viscosities. For S1813, spin speeds of 5000 - 7000 rpm, for duration of 45 s yield film thicknesses between 1.5 and 1 μm. Spinning is accomplished using programmable vacuum spinners located in the Class 100 area of the CRANN cleanroom, at the appropriately called "Spinner Bench". After the resist has been spun, the substrate is baked at high temperature to drive out excess solvent from the photoresist. This process is called *soft-baking*. The drive out of solvent is an important step and can greatly affect the end process. If the baking time is too short, excess solvent will interfere with the exposure of photoresist closer to the substrate. If it is too long, the sensitivity of the photoresist will be higher so that the exposure parameters are no longer valid. If the baking temperature is too high, it is possible to crosslink the polymer chains such that it is desensitised to UV light and in general it is more difficult to remove. This is termed *hard-baking*. [3]

3. The sample is then loaded into the exposure tool, in this case we use the OAI mask aligner located in the Class 100 are of the CRANN cleanroom. The mask aligner is set up for exposure at 365 nm (i-line near-ultraviolet) and this offers a resolution of below 2 μm. Pattern transfer is accomplished using a photomask. The photomask (or reticle) is made of quartz or soda-lime glass and the pattern to be transferred is etched in chrome on one side. Areas with chrome do not permit the transmission of UV light to the photresist whereas areas without chrome do. The substrate is moved such that the target pattern is located over the desired area of interest. This alignment is used for multiple step processing.

4. In order to achieve high resolution the photomask must be moved as close as possible to the photoresist and the substrate. There are three exposure modes on the OAI tool, soft, hard and vacuum contact. Soft contact does not use any mechanical force to press the substrate to the photomask. Hard contact uses N_2 gas to press the substrate against

[3]Some photoresists can be hard-baked (such as nLOF AZ-2070, baked at 250°C) to offer superior chemical resistance. This is most usefully done after developing, in order to create a hard mask.

the photomask. Vacuum contact evacuates the space between the chuck table (where the substrate is placed) and the photomask. Atmospheric pressure then presses the substrate to the photomask. Vacuum contact offers the highest resolution and is the mode we employ here.

5. Once we have good contact between the photomask and the substrate we are ready to expose the photoresist to UV light. The mask aligner is programmable and the final dose to the photoresist is calculated using the beam intensity and the time exposed. The beam intensity is generally in the range of 14-18 mW/cm^2, however this can fluctuate and is measured using a hand-held intensity meter prior to exposure. The exposure dose for S1813 is $\sim$ 50 mJ/cm^2. The dose required depends on several key factors, above all the resist has its own "ball-park" exposure dose. The end user can, however, modify the dose required by choosing different resist thickness and soft-baking times. The entire sample is flood irradiated using a broad beam UV source, the beam being uniform over 150 mm (6"). All of the photomask is illuminated in the one exposure. When the photoresist is illuminated the photoactive compound breaks down. The tool is automatically programmed to expose the sample for a given time with a resolution of 100 ms. Once the exposure is complete the sample is automatically moved out of contact with the photomask. The sample is now ready to be developed [4]

6. The substrate is then placed in a solvent solution for development. During development of positive (negative) resist the areas that are exposed (unexposed) to UV light are dissolved. For S1813 development is performed in Microposit MF-319 for $\sim$ 45 s until a clear pattern is visible on the substrate. The dissolution rate of the exposed photoresist depends on the exposure parameters, such as exposure time (i.e. dose) and softbaking time. In general the time constraint on development is not as stringent. Development between 45 -60 s (until the pattern is visible and excess resist is removed) gives good quality results. Immediately after development samples are placed in de-ionised (DI) water to halt the

[4]some photoresists, such as nLOF AZ-2070, may require a post-exposure bake to stabilise the photoresist before development.

chemical reaction of the developer. The DI rinse has no time limit, allowing optical inspection with a microscope to be carried out.

7. If the pattern transfer to the photoresist is successful we can proceed to ion milling. Here, a broadbeam Ar^+ ion source is used to sputter the material (or device stack) not protected by photoresist. For more information see Appendix A. The broadbeam milling is not selective in terms of materials, but the etch rate is different for different materials. Reactive ion etching (RIE) is selective but it requires particular process chemistries for each material to be etched. RIE is not used here. During this step we have the option to monitor in real-time the ions ejected from the sample using Secondary Ion Mass Spectropy (SIMS). SIMS can be used to determine which layer is being etched and allows us to stop in a particular material layer, or when we have etched down to the Si/SiO_2. SIMS is also used to see the what elements are present in a device stack.

8. The sample is then removed from the ion miller and the photoresist mask is removed using either acetone/isopropanol/N_2 as described earlier or using Microposit resist stripper 1165 which is heated to 80°C. If the resist stripper is used the sample is placed in DI water for at least 60 s to remove the stripper from the substrate. In general, 1165 resist stripper is used when removal of resist is difficult using acetone. It can be used in combination with ultrasonic agitation, but should always be heated at 80°C. The lithography process is now finished and if further lithography steps are required the sample can be re-inserted into the start of the process.

The above steps describe photolithography from the point of view of ion milling. The process can also be accomplished for "lift-off". In a lift-off process deposition takes place after pattern transfer, and after deposition the pattern is removed. This will leave material deposits within the gaps of the pattern. In this thesis all samples were patterned by ion milling with the exception of one, which was defined by lift-off. A manual describing the usage of the Millatron for ion milling is given in Appendix A.

2.3.2 Focused He^+ Ion Beam Patterning

We employ a state-of-the-art Carl Zeiss Helium-Ion Microscope (HeIM) for magnetic patterning of multilayer systems [5]. The HeIM is housed in the CRANN Advanced Microscopy Laboratory (CAML). An image of the HeIM is shown in Figure 2.10. Within the ion column a very fine tip composed of three atoms (known as the trimer) is charged to high positive potential, He gas atoms surround the tip and can be field ionised in the vicinity of the trimer. Once ionised they are accelerated towards the extractor at the base of the column. This field ionisation from the trimer gives a very bright beam approximately one atom wide. This beam of ions is then directed using electromagnetic lenses (found in a typical scanning electron microscope) towards the specimen under investigation. The beam diameter at the sample can be as small as 0.25 nm. The beam is rastered over the specimen and the secondary electrons generated allow an image to be built up. The HeIM offers advantages over traditional electron microscopes. These include negation of surface charging effects (positive charge can be neutralised using an electron flood gun), imaging using backscattered He^+ ions to provide material contrast and accessibility of Rutherford backscattering (RBS) using a nanoscale probe. The main plus point for employing the HeIM is that we have a focused beam of light ions. This can be used for imaging, ion induced modification and even surface milling. We used the focused beam of ions to study the effect of local irradiation damage on the perpendicular magnetic anisotropy of Co/Pt multilayers. Work on the HeIM is featured in Chapter 6 and is conducted in collaboration with Dr. Gavin Behan, the microscope's key operator.

2.4 Characterisation

2.4.1 X-Ray Diffraction

X-Ray diffraction and reflectivity measurements were performed in a Phillips X-Pert Pro system using Cu-Ka radiation of wavelength λ=1.5418 Å. This wavelength is of the order of the interatomic distance. X-rays are diffracted from the planes of a crystallographic sample and we

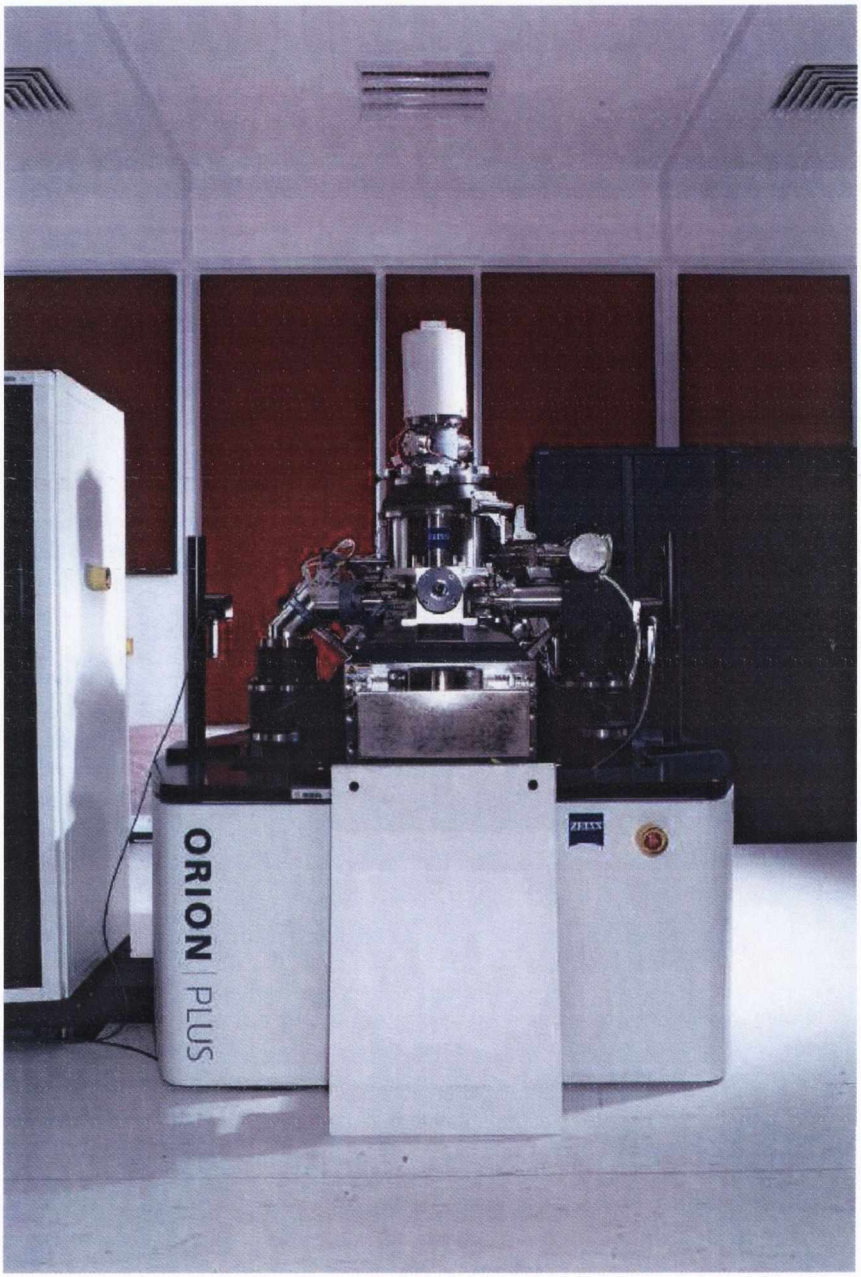

Figure 2.10: The helium ion microscope

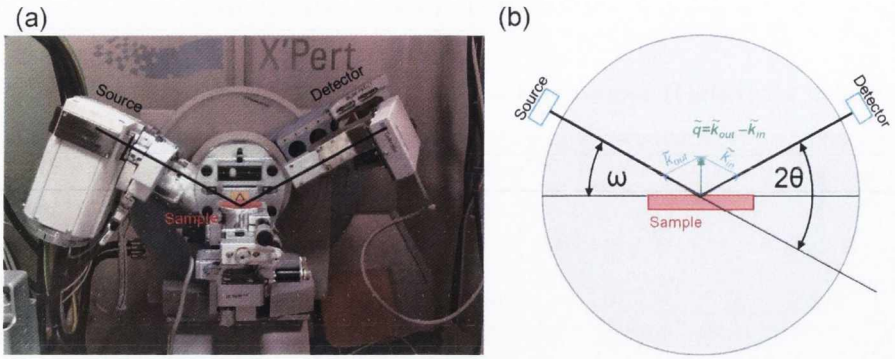

Figure 2.11: (a) Sample stage for the PANalytical XRD with source and X'Celerator detector. (b) Diagrammatic representation of diffraction from a crystalline sample.

will have strong constructive interference when the following condition is met

$$2dsin\theta = m\lambda \tag{2.1}$$

where m is an integer, d is the distance between two crystal planes and θ is half the angle between the beam projected through the sample and the diffracted beam. This is known as Bragg's Law. This allows a diffraction pattern to be built up as the angle is varied around the normal of the reflecting planes.

A photograph of the tool used and a diagram explaining the principle of diffraction from a crystal are shown in Figure 2.11. In reciprocal space, the difference in the outgoing and incoming wavevectors ($\tilde{k}_{out} - \tilde{k}_{in}$) must coincide with another lattice point in reciprocal space. Since the lattice planes are not necessarily parallel to the surface of the sample we define θ as half the angle between the transmitted x-ray beam and the "reflected"[5] beam. We align the diffractometer to the substrate diffraction peak (Si - 69.13°). If we vary the angle 2θ we will obtain a diffraction pattern from the family of lattice planes perpendicular to the film normal (the substrate normal). The peaks obtained in the diffraction pattern will contain information based on the lattice d-spacing. In this way we will obtain diffraction information about the texture (or growth direction of the thin film). As such the FWHM of any diffracted peaks

[5]x-rays are not reflected only diffracted, but we imagine for simplicity that we can have a reflected beam

will yield information based on the grain size *along the film normal*. It is important to note that X-ray diffraction is only useful on crystalline systems, there will be no diffraction pattern from amorphous materials. In order to obtain information about the alignment of the growth texture to the substrate normal we can vary the angle ω while fixing 2θ. In this way we obtain information about the mosaic spread of the texture, i.e. how well aligned the grains are relative to the growth direction.

Further to X-ray diffraction we can also employ X-ray reflectivity to determine, precisely, thin film thicknesses. This is used, for example, to calibrate the growth rates in the Shamrock system. At low angles, above the critical angle (where total external reflectivity occurs) we will have constructive interference pattern based on the distance between the air/film interface and the film/substrate interface. Since there is a change of refractive index and electronic density at the film/air interface and the film/substrate interfaces we will have a change in reflection/transmission at theses interfaces. This will form two coherent sources of reflected beams. These coherent sources will interfere constructively and create an oscillatory pattern based on the Fourier transform of the vertical distance between the two sources. A typical XRR graph is shown in Figure 2.12. The nature of the oscillations can be modelled using: the materials density, which determines the critical angle for total external reflection; the layer thickness, which gives rise to the oscillation frequency as the scanning angle is increased; the layer roughness, which determines the drop in amplitude as a function of angle. Rougher films exhibit a much sharper drop in amplitude of interference with increasing angle than smooth layers. Since the probe wavelength is of the order of an atomic radius the resolution of X-ray reflectivity can be of the order of a monolayer of material. However, the overall layer thickness under investigation should be of the order of tens of nanometers to obtain an interference pattern with enough oscillations to make simulation worthwhile. Typically film thicknesses in the region of 30 - 50 nm can be simulated to within a few angstrom of thickness. In terms of growth rate calibrations this corresponds to an error in growth rate far below 0.1 Å/s.

The oscillation maxima, corresponding to constructive interference, are related to the film

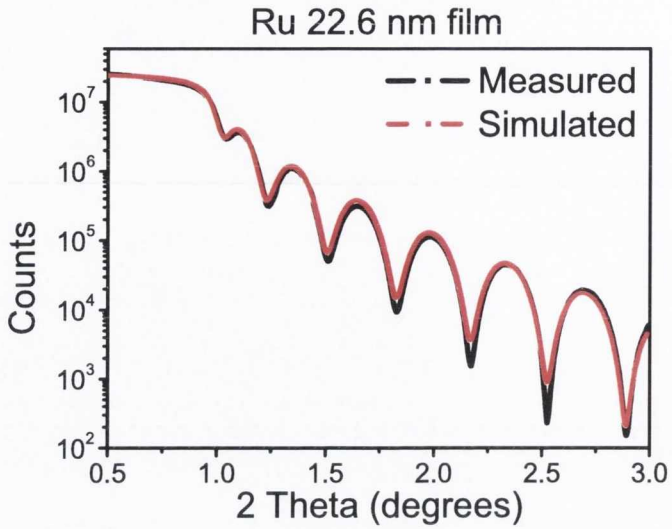

Figure 2.12: Measured and simulated X-ray reflectivity (XRR) curves for a thin film sample of Ru. The simulated fit was obtained using a software package called WinGixa

thickness via a modified Bragg's Law;

$$m\lambda = 2t\sqrt{sin^2\theta - 2\delta} \tag{2.2}$$

where m is the peak order, λ is the wavelength of radiation used, t is the film thickness, θ is the angle between the source and the film and δ is the dispersive refractive index of the film material. We can think that, in the reflectivity case, d from Equation 2.1 is now the distance between the film surface and the substrate.

2.4.2 The R-T Rig

The R-T (resistance-temperature) rig is a home-built measurement setup comprising the following subsystems; an electromagnet, a cryostat, an acquisition computer, a temperature controller and a Keithley 2400 sourcemeter. An image of the system is shown in Figure 2.13.

The base temperature of the cryostat is 12 K, and is attached to a closed cycle helium gas compressor which cools the cold head in the cryostat. The electromagnet is controlled by a Kepco 10 amp bi-polar analogue power supply which is controlled via the acquisition computer.

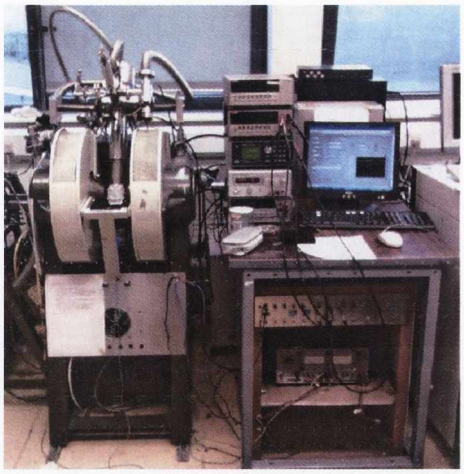

Figure 2.13: The R-T rig located in the CRANN building.

Electrical measurements are made through a Keithley 2400 sourcemeter which is connected via a GPIB to the acquisition computer. Labview software on the computer allows for automated collection of current/voltage/resistance data from the Keithley while sweeping the magnetic field on the electromagnet. The temperature is also controlled via Labview. The maximum field that can be applied in this system is $\pm$ 180 mT. The field is measured using a Hall sensor mounted directly on one pole of the electromagnet. As a result the measured field is the real field and not the calculated field from the power supply. The R-T rig is employed for extraordinary Hall effect measurements throughout this thesis.

2.4.3 Extraordinary Hall Effect

In metals, diffusive transport and scattering leads to resistance. Upon the application of a voltage across a metal conductor, a current will flow. The amount of current that flows is related to the applied voltage via the materials resistivity: this is Ohm's Law and is quite fundamental. The reason this is stated is to introduce, at the beginning of this section, the idea that electrons are scattered inside a metal.

When a current, I_y, is passed through a thin film (with cross-sectional area $A = bd$) and a magnetic field is applied along the film normal the charge carriers experience the Lorentz force,

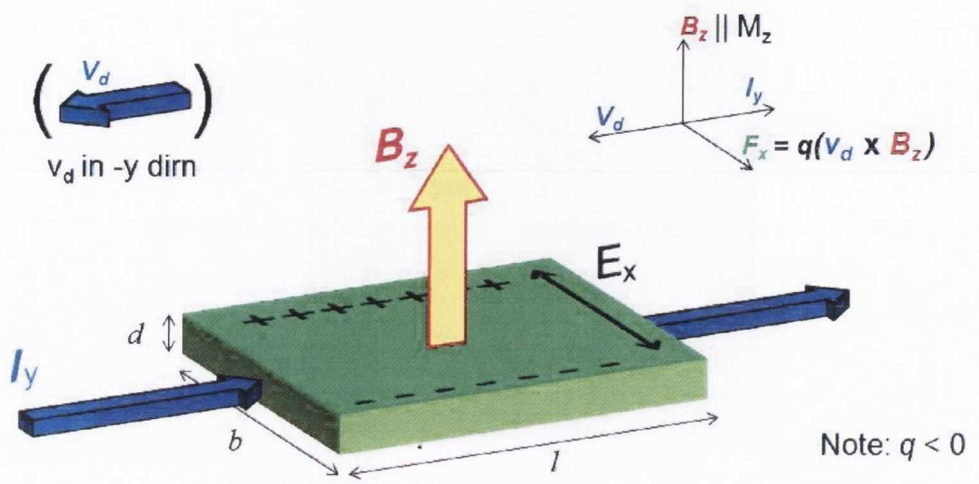

Figure 2.14: The ordinary Hall effect. Charge carriers experience the Lorentz force in a magnetic field resulting in a transverse potential difference. Note in this case electrons are the charge carriers i.e. $q < 0$

$F_x = q(v_d \times \mu_0 \mathbf{H}_z)$, where q is the charge, v_d is the drift velocity (in the y direction) and $\mu_0 \mathbf{H}_z$ is the applied magnetic field along the film normal. This is shown in Figure 2.14. Since the magnetic field is perpendicular to the current this becomes $F_x = qv_d \mu_0 \mathbf{H}_z$ or $F_x = qv_d \mathbf{B}_z$.

When the resulting electric field, qE_x, is large enough to oppose the Lorentz force we will have a static potential difference across the thin film, perpendicular to the current. This means that

$$qE_x = -qv_d \mathbf{B}_z \tag{2.3}$$

The current density associated with the flowing current is $J_y = I_y/A$ is proportional to the charge carrier density n by $J_y = nqv_d$. Substituting v_d into equation 2.3, we obtain

$$nq = -\frac{J_y \mathbf{B}_z}{E_x} \tag{2.4}$$

Since $J_y = I_y/A$ and the electric field E_x is equal to V_x/b this becomes

$$nq = -\frac{I_y \mathbf{B}_z b}{V_x A} \tag{2.5}$$

In an experimental setup we can measure the transverse resistance $R_{xy} = V_x/I_y$. The transverse resistivity is given by $\rho_{xy} = R_{xy}A/b$. Therefore equation 2.5 becomes

$$nq = -\frac{\mathbf{B}_z b}{R_{xy}A} = -\frac{\mathbf{B}_z}{\rho_{xy}} \Longrightarrow \rho_{xy} = -\frac{1}{nq}\mathbf{B}_z \Longrightarrow \rho_{xy} = R_H \mathbf{B}_z \tag{2.6}$$

we define a quantity called the Hall co-efficient, R_H, equal to $-1/nq$. If we plot the transverse resistivity ρ_{xy} against $\mathbf{B}_z$, the slope yields a value for $1/nq$. Since in metals n is considerably larger than q it can be seen that R_H is quite small. It is possible to fabricate a magnetic field sensor based on the Hall effect. They are generally fabricated using semiconductor materials where R_H is larger, since n is lower.

In transition metal ferromagnets, however, there is a much larger contribution to the transverse resistivity, which is called the extraordinary Hall effect. It is a result of spin dependent scattering of the carriers and spin-orbit coupling. The contribution of the extraordinary Hall effect is much larger than the ordinary Hall effect and dominates the resistance in transition metal ferromagnets. Since the carrier density in metals is so large the ordinary Hall effect is small.

In order to take this into account we modify equation 2.6 to include a contribution proportional to the magnetisation component in the field direction, M_z.

$$\rho_{xy} = R_H \mathbf{B}_z + R_S M_z \tag{2.7}$$

where R_S is the extraordinary Hall co-efficient. Unfortunately there is no simple expression for R_S and it is treated, in this thesis, as a phenomenological proportionality constant. The origins of the extraordinary Hall effect are discussed below.

In transition metal ferromagnets the electronic transport is due to both s and d electrons. Due to the hybridisation of the s and d orbitals, the s electrons can scatter into the d band and vice versa. Since the filling of the d band is responsible for transition metal magnetism and they also partake in conduction we have a coupling between the electrical and magnetic properties. Though we cannot measure the absolute value of magnetisation (as ρ_{xy} is proportional to M_z by the constant R_S), we can use the extraordinary Hall effect measurement to determine the

magnetic switching characteristics of a film as a function of field field.

The scaling factor R_S is inferred from comparisons between magnetisation measurements and the transverse voltage measured. For the extraordinary Hall effect the relationship of the transverse resistivity, ρ_{xy}, to the longitudinal resistivity, ρ_{xx} is found to vary across different materials and devices. This relation is generally assumed to be of the form $\rho_{xy} \propto \rho_{xx}^{\beta}$, where β is a number usually between 1 and 2. The extraordinary Hall effect can originate from several scattering mechanisms, skew scattering, quantum side-jump or intrinsic deflection which stems from a quantum mechanical *Berry* phase [6]. Both skew scattering and the quantum side jump are extrinsic scattering processes. For skew scattering, an extrinsic mechanism the scattering angle is dependant on the spin direction when an electron scatters off an impurity. It is due to spin-orbit interaction during scattering [7]. The quantum side jump mechanism causes a direct displacement of the electron inversely proportional to the mean free path. In materials with a small mean free path the quantum side jump should dominate [8]. For skew scattering R_S is linearly proportional to the longitudinal resistivity, and for quantum side jump it is proportional to the square of the longitudinal resistivity i.e. $\rho_{xy} \propto \rho_{xx}$ or $\rho_{xy} \propto \rho_{xx}^2$. The intrinsic deflection was proposed in 1954 by Karplus and Luttinger [9]. When an electric field is applied to a metal there is a change of the electron group velocity in the direction perpendicular to the field. This electric field is the field that drives the current I_x not the electric generated by the Lorentz force E_y. In a ferromagnet, the contribution to the group velocity is nonzero when summed over all the occupied band states and can therefore contribute to the Hall resistivity. This mechanism will give $\rho_{xy} \propto \rho_{xx}$. In multilayer films there is still debate about which mechanism is dominant [10, 11, 12, 13, 14, 15].

The extraordinary Hall effect is primarily used to observe the coercivity of a multilayer with perpendicular magnetic anisotropy (PMA) [16] and also layers with both in-plane and out-of-plane components [17] [18]. The saturation Hall resistivity can be used to quantify a change in magnetisation M_z. For instance, in systems that are modified externally (such as by ion irradiation) we can relate a change in Hall resistivity to a change in M_z. This is justified as we make no judgement to the magnitude of change only that the magnetisation has decreased.

An excellent review of the EHE and its origins in alloys and thin films can be found in Ref. [6].

2.4.4 SQUID Magnetometry

Although the extraordinary Hall effect can be used to characterise the magnetisation switching of the z-component of magnetisation, it is unable to give a direct value for the total magnetisation of the sample. To measure the magnetisation we employ a Quantum Design Superconducting QUantum Interference Device (SQUID) magnetometer. SQUID is a non-destructive measurement and both in-plane and perpendicular-to-plane components of the magnetisation can be determined. SQUID measurements in this thesis are primarily used to determine the anisotropy field and the saturation magnetisation of magnetic materials under investigation. All of the SQUID data were obtained by Dr. M. Venkatesan.

Bibliography

[1] Grachev, S.Yu., Tichelaar, F.D., Janssen, G.C.A.M. *Journal of Applied Physics* **97**(7), 1–4 (2005).

[2] Kelly, P.J., Arnell, R.D. *Vacuum* **56**(3), 159 – 172 (2000).

[3] Kelly, P.J., Abu-Zeid, O.A., Arnell, R.D., Tong, J. *Surface and Coatings Technology* **86-87**(Part 1), 28 – 32 (1996).

[4] Campbell, S.A. *The Science and Engineering of Microelectronic Fabrication.*

[5] Postek, M.T., Vladar, A.E., Kramar, J., Stern, L.A., Notte, J., McVey, S. volume 931, 161–167, (2007).

[6] Nagaosa, N., Sinova, J., Onoda, S., MacDonald, A.H., Ong, N.P. *Reviews of Modern Physics* **82**(2), 1539–1592 (2010).

[7] Smit, J. *Physica* **24**(1-5), 39–51 (1958).

[8] Berger, L. *Physical Review B* **2**(11), 4559–4566 (1970).

[9] Karplus, R., Luttinger, J.M. *Physical Review* **95**(5), 1154–1160 (1954).

[10] Zhang, S. *Physical Review B* **51**(6), 3632–3636 (1995).

[11] Canedy, C.L., Li, X.W., Xiao, G. *Physical Review B - Condensed Matter and Materials Physics* **62**(1), 508–519 (2000).

[12] Song, S.N., Sellers, C., Ketterson, J.B. *Applied Physics Letters* **59**(4), 479–481 (1991).

[13] Vavra, W., Lee, C.H., Lamelas, F.J., He, H., Clarke, R., Uher, C. *Physical Review B* **42**(7), 4889–4892 (1990).

[14] Sato, H., Kumano, T., Aoki, Y., Kaneko, T., Yamamoto, R. *Journal of the Physical Society of Japan* **62**(2), 416–419 (1993).

[15] Khatua, P., Majumdar, A.K., Temple, D., Pace, C. *Physical Review B - Condensed Matter and Materials Physics* **73**(9), 1–7 (2006).

[16] Guo, V.W., Lu, B., Wu, X., Ju, G., Valcu, B., Weller, D. *Journal of Applied Physics* **99**(8), 08E918 (2006).

[17] Wong, S.-K., Chia, B.H., Srinivasan, K., Law, R., Tan, E.-L., Tan, H.K., Sbiaa, R., Piramanayagam, S.N. *Journal of Applied Physics* **106**(9), 093904 (2009).

[18] Lindemuth, J., Dodrill, B. *IEEE Transactions on Magnetics* **40**(4 II), 2191–2193 (2004).

Chapter 3

Magnetic Anisotropy of Thin Films

"Stand in line"

- Andy Cairns, Vocalist/Guitarist, Therapy?

3.1 Anisotropy

Anisotropy is the term used when the magnetisation of a ferromagnet or an antiferromagnet has a preferred orientation. That is the magnetisation will lie along an *easy axis* at zero field[1].

A example is a permanent magnet with high uniaxial magneto-crystalline anisotropy. This high anisotropy ensures that the magnetisation stays along the same direction for a long time; high anisotropy means large thermal stability. The magnetic recording industry requires high anisotropy (for thermal stability) but also requires a reasonable switching field (higher anisotropy means a higher magnetic field is required to switch the magnetisation direction).

The uniaxial anisotropy energy density is given by the expression

$$\varepsilon_a = K_1 sin^2\theta + K_2 sin^4\theta + K_3 sin^6\theta \tag{3.1}$$

with θ being the angle between the easy axis and magnetisation (Figure 3.1), but this is often simplified to the leading order term $K_1 sin^2\theta$, where K_1 is the anisotropy energy density. The

[1] sometimes, in tetragonal or hexagonal crystals, there may be two or three experimental easy axes

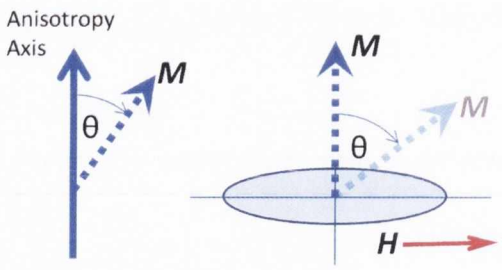

Figure 3.1: (left) The angle theta is defined as the angle between the magnetisation vector and the anisotropy axis. (right) An example of a film with uniaxial anisotropy.

units of K are J/m^3.

If K_1 is positive, the anisotropy energy is maximum when $\theta = \pi/2$ i.e when the magnetisation is saturated perpendicular to the anisotropy axis. It is minimum when $\theta = 0$ and the magnetisation is saturated along the anisotropy axis. A simple depiction of the anisotropy axis and the magnetisation is shown in Figure 3.1 and the response of the magnetisation to a field **H** applied perpendicular to the anisotropy axis is shown on the right. As the field is applied, the magnetisation **M** subtends a larger angle with the anisotropy axis. When the magnetisation is deflected from the easy axis, a demagnetising field is created. This demagnetising field serves to return the magnetisation to the easy axis. The demagnetizing energy when the magnetisation is saturated along the *hard axis* is $\varepsilon_{demag} = \frac{1}{2}\mu_0 V N M_s^2$ where N is the demagnetising factor, V is the volume and $\mathbf{M}_s$ is the saturation magnetisation. The field required to saturate the magnetisation along the hard axis (perpendicular to the anisotropy axis where $\theta = \pi/2$) is called the *anisotropy field*, $\mathbf{H}_a$, in MA/m and $\mu_0\mathbf{H}_a$ is in Tesla. Minimising the energy in the system ensures the magnetisation points along the easy axis. Figure 3.2 shows easy and hard axis magnetisation data for YCo_5, a hexagonal compound possessing uniaxial magnetic anisotropy along the c-axis. A field along the c-axis easily saturates the film, whereas a field of 12 MA/m (15 T) is required to saturate the magnetisation perpendicular to the easy axis[1]. Another example is shown in Figure 3.3. In this thin film case a sandwich of Pd/Co/Pd exhibits perpendicular anisotropy when the Co layer is ultra-thin. At larger Co thickness the anisotropy stemming from the interfaces is unable to compete with the demagnetising field which increases with volume, turning the easy asix in-plane.

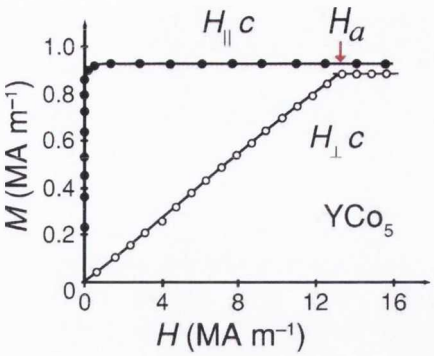

Figure 3.2: Magnetisation as a function of applied field in single crystal YCo_5. $\mathbf{H}_a$ is the anisotropy field [2]

Magnetic anisotropy can arise from three different sources: the shape anisotropy (section 3.1.1) which arises from the macroscopic shape of the magnet; the magneto-crystalline anisotropy (section 3.1.2) which arises from the spin-orbit interaction and couples the magnetisation to the crystal; the magneto-elastic anisotropy (section 3.1.3) which is is due to strain of the magnetic material when grown on substrates with a different lattice constant. Magneto-elastic anisotropy is a form of magneto-crystalline anisotropy arising from a direct deformation of the unit cell. For the context of this thesis we will discuss these contributions in terms of the effective anisotropy K_{eff}

$$K_{eff} = K_V + 2K_S/t \tag{3.2}$$

where K_V and K_S are the volume (bulk, thickness independent) and surface (interface, thickness dependent) anisotropies, respectively, and t is the film thickness. The multiplier 2 is due to the fact that there is two interfaces on either side of the thin film. Typical values for K_V and K_S are 1 MJ/m^3 and 1 mJ/m^2.

3.1.1 Shape anisotropy

Shape anisotropy results from the magnetic dipolar interaction: it is determined by the sample shape and is therefore not an intrinsic property. The shape anisotropy of an object can be

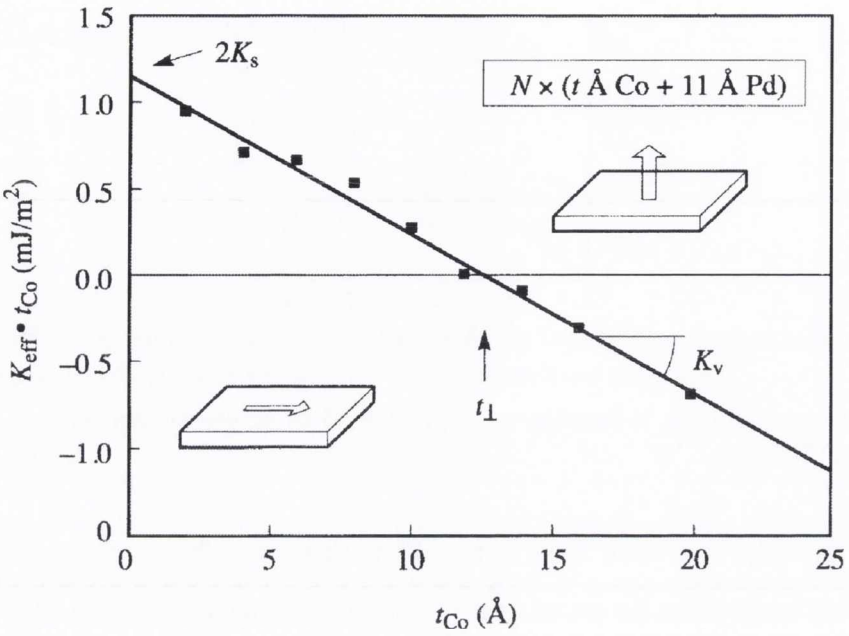

Figure 3.3: Effective anisotropy (K_{eff}) times Co thickness versus Cobalt thickness [3].

defined, for example, by lithography in a patterning process (see section 2.3). The magnetic dipole interaction is a long range interaction and gives rise to the demagnetizing field $\mathbf{H}_d$, given by

$$\mathbf{H}_d = -\overline{\overline{N}}\mathbf{M} \tag{3.3}$$

where $\overline{\overline{N}}$ is a tensor that is dependant on the geometry of the object, and $\mathbf{M}$ is the magnetisation. The principal components of $\overline{\overline{N}}$ are N_x, N_y and N_z, and the tensor satisfies the condition $\mathrm{tr}(\overline{\overline{N}}) = 1$. For an ellipsoid of revolution $N_x = N_y \neq N_z$. For a thin film, $N_x = N_y = 0, N_z = 1$ This shape anisotropy tends to make the magnetisation of the thin film object lie in the plane and not along the film normal.

The origin of shape anisotropy lies in the demagnetizing field. The demagnetizing field opposes the direction of magnetisation within the magnet. As the magnetisation is tilted from the anisotropy axis the demagnetizing field increases via equation 3.3. This is because any deviation from $\theta = 0$ implies a demagnetizing field exists. The demagnetizing field, $-\mathbf{M}sin\theta$, is maximum when the magnetisation is perpendicular to the thin film, when θ=$\pi/2$, and must

be overcome to saturate the film along that direction. The magnetostatic energy of a film in its demagnetizing field is given by

$$\varepsilon_{sh} = \frac{1}{2}\mu_0 V N M_s^2 \tag{3.4}$$

where μ_0 is the permeability of free space, V is the volume, N is the demagnetizing factor and M_s is the saturation magnetisation. A small object can be approximated as an ellipsoid of revolution. Spheres and thin films can be worked out from the ellipsoid. The shape anisotropy, K_{sh}, for an ellipsoid of revolution, is defined as energy difference per unit volume between the easy and hard directions.

From [1],

$$\varepsilon_{sh}/V = K_{sh} = \frac{1}{4}\mu_0 M_s^2 (1 - 3N) \tag{3.5}$$

For a sphere, where $N = 1/3$, $K_{sh} = 0$. This is a consequence of the high symmetry of a sphere. Magnetisation can point along any radius in the sphere and the demagnetizing field is equal. For a thin film, $N = 1$ perpendicular to the film normal and 0 for all other directions. The shape anisotropy energy density in this case is then $(K_{sh,N=0} - K_{sh,N=1})$,

$$K_{sh} = -\frac{1}{2}\mu_0 M_s^2 \tag{3.6}$$

This implies that, due to shape alone, the magnetisation in thin films should be confined to the film plane, where the demagnetizing field is minimum.

For thin film with magnetisation 1.1 MA/m, the shape anisotropy is -0.726×10^6 J/m^3. This magnetisation corresponds approximately to that of a thin film of the amorphous alloy $Co_{40}Fe_{40}B_{20}$ which is investigated in Chapter 4. For a thin film of Co ($M_s = 1.4$ MA/m) the shape anisotropy is -1.31×10^6 J/m^3. This energy must be countered in order to orient the magnetisation perpendicular to the plane. In contrast the magneto-crystalline anisotropy of Co is 0.5×10^6J/m^3, so that the magnetisation of a Co film lies in-plane even when the c-axis is perpendicular to the film.

3.1.2 Magneto-crystalline Anisotropy

The spin-orbit interaction, the interaction that couples the electronic spin to the orbital motion of the charged nucleus around the electron in the electronic rest frame, gives rise to the magneto-crystalline anisotropy. Spin-orbit coupling is represented by $\xi \mathbf{L} \cdot \mathbf{S}$, where ξ is the spin-orbit constant, **L** is the orbital angular momentum and **S** is the spin angular momentum. As a result of the spin-orbit interaction, the crystal symmetry will affect the magnetisation direction. This results in an anisotropy axis stemming from the *3d* orbital motion with respect to the crystal axes. For the bulk the anisotropy originates in the crystal structure. In simple cubic cells the magneto-crystalline anisotropy is low due to the high symmetry of the cubic cell. In non-symmetric cells, such as the hexagonal closed packed structure the magnetisation tends to lie along the c-axis. The c/a ratio in these cells becomes very important in obtaining high anisotropy. The hexagonal YCo_5 shown in Figure 3.2 is an example of a high magneto-crystalline anisotropy material. Highly ordered $L1_0$ alloys of CoPt and FePt also exhibit high magneto-crystalline anisotropy [4] [5].

The magneto-crystalline anisotropy from the interface can be different from the bulk. Néel calculated this purely surface anisotropy to be of the order 1 mJ/m^2 (1 ergs/cm^2) [6]. It is always included in K_S. In the bulk, it is possible to have band structure due to the extended nature of the material. This is no the case at the interface where there is no longer a continuum of atoms. At the interface the *d* electrons become more localised to the atomic cores, and the electron energy levels becoming more atomic like. Also at the interface there can be the possibility to have a larger orbital moment. The electron orbitals can be affected by a break in symmetry [7] and can be pushed into the plane, giving a moment out of the plane. In simple cubic systems, with low magneto-crystalline anisotropy in the bulk, the magneto-crystalline anisotropy at the interface can be very large. An example of this is the high perpendicular anisotropy observed in the Co/Ni system [8]. The magneto-crystalline anisotropy contributions are on the order of 10^6 J/m^3 [9]. The sharpest interfaces give the strongest interfacial anisotropies. In that respect, attention must be paid to interface preparation.

Ab initio calculations are useful in determining the magneto-crystalline anisotropy but are

not trivial [9]. Modern calculations have been especially useful in the study of the electric field control of magnetic anisotropy where the anisotropy of free standing Fe layers on MgO have been calculated [10][11][12][13] and compare favourably with experimental data points.

3.1.3 Magneto-elastic Anisotropy

The magneto-elastic anisotropy arises when a magnetic film is exposed to a stress, e.g from a lattice mismatch with adjacent crystalline materials in a multilayer. Its energy is given by

$$K_{me} = \frac{3}{2}\lambda_s \sigma \tag{3.7}$$

where λ_s is the magnetostriction constant, and σ is the applied stress in N/m^2, which is related to the dimensionless strain, ε, via $\sigma = E\varepsilon$ where E is the bulk modulus. The magneto-elastic anisotropy is a result of the deformation of the unit cell. It is therefore a form of magneto-crystalline anisotropy. The contribution from the deformation of the unit cell can be expressed in terms of the change in aspect ratio of the unit cell, the c/a ratio for instance. There is also reports that the deformation is not confined to magnetic materials, but can be observed in Pt [14]. Such a deformation in Pt could lead to a change in the magneto-elastic anisotropy in a Pt based magnetic multilayer, though it is noted the effect is very small.

When the lattice mismatch is small, the lattice constants of the material will grow or shrink to accommodate the mismatch. One material will be under compressive strain, the other under tensile strain. This lattice strain will exist up to a critical thickness, t_c, above which it becomes energetically favourable for dislocations to relieve the strain on the layer. In the region below t_c the anisotropy is said to be in the *coherent* regime, while above t_c it is said to be in the *incoherent* regime.

When the strain is uniform over the layer, the entire volume will experience the strain. This occurs below t_c when there are no dislocations. In the coherent regime the contribution will only be to the volume anisotropy K_V. This is shown in Figure 3.4 (a).

Above t_c, dislocations are introduced to accommodate the lattice mismatch. This means that

the contribution to the anisotropy is dependent on the thickness (Figure 3.4) and will contribute to the surface anisotropy K_S.

The lattice mismatch between to materials A and B is given by

$$\eta = (a_B - a_A)/a_A \tag{3.8}$$

where a_A and a_B are the in-plane lattice constants for materials A and B respectively. In terms of layer A (the magnetic layer for example) the equation 3.7 becomes $K_{me} = \frac{3}{2}\lambda_s E_A \varepsilon_A$.

It has been shown that above and below the critical thickness, t_c, the contribution of K_{me} will change from a volume to surface type contribution [15][16]. From [16] specifically; below t_c, $\varepsilon = -\eta$ and above t_c, $\varepsilon = -\eta t_c/t_A$, where t_A is the thickness of the magnetic layer.

This leads to two types of magneto-elastic contributions, volume and surface, originating from the coherent and incoherent regimes respectively,

$$K_{me,V}^{coh} = \tfrac{3}{2}\lambda_s E_A \eta \qquad K_{me,S}^{inc} = \tfrac{3}{2}\lambda_s E_A \eta t_c \tag{3.9}$$

The magnetoelastic anisotropy contributes only to the volume anisotropy below t_c and to the surface anisotropy above t_c when a defect in the lattice occurs. It should be noted that $K_{me,S}^{inc}$ will be divided by the magnetic layer thickness t_A in order to be included in K_{eff} (equation 3.2), such that its contribution to K_{eff} will be $= \frac{3}{2}\lambda_s E_A \eta t_c/t_A$. The dependency on thickness of these contributions are shown in Figure 3.4. It is possible to calculate the contributions from equation 3.9. Below we will do this for a typical bilayer of Co and Pd in both the coherent and incoherent regimes.

The lattice parameter of Pd is 3.89 Å and for *fcc* Co it is 3.51 Å [17]. This gives a a lattice mismatch value of $\eta = 0.11$ according to equation 3.8.

For Co, Young's modulus is 209×10^9 Pa and the magnetostriction constant is measured to be 6×10^{-5}. This gives $K_{me,V} = 2.07 \times 10^6$ J/m^3. If we combine this with the shape anisotropy we calculated in section 3.1.1 ($K_{sh} = -1.31 \times 10^6$ J/m^3) the effective anisotropy becomes, $K_{eff} = K_{sh} + K_{me} = 0.76 \times 10^6$ J/m^3. It should be noted the sign of K_{eff} corresponds

to perpendicular anisotropy. We have only assumed abrupt "perfect" interfaces.

Above t_c, the magnetoelastic anisotropy will contribute to the surface anisotropy, not the volume. In this case the interfacial contribution of a Co thin film with a critical thickness of, say $\sim 3 \times 10^{-10}$ m (3Å) (1 ML) is 0.52 mJ/m^2. This positive contribution serves to stabilise the perpendicular anisotropy.

Experimentally, as thickness is increased the surface anisotropy is weakened. Above a critical thickness (which corresponds to $K_{eff} = 0$) the magnetisation will no longer lie along the film normal, but in the plane of the film, see Figure 3.3. This will happen at a crossover thickness, which we will call $t_\perp$. In order to determine this thickness we will rearrange equation 3.2 and set $K_{eff} = 0$. This gives

$$t_\perp = \frac{-2K_S}{K_V} \tag{3.10}$$

K_V in this case will be the shape anisotropy (-1.31×10^6 J/m^3) and K_S will be the interfacial anisotropy above t_c (0.52×10^{-3} J/m^2). This implies that $t_\perp$ is 0.8 nm (8 Å). In general it is found that the perpendicular anisotropy survives to greater thicknesses. We have only considered so far the contributions from shape and magneto-elastic anisotropy. As mentioned previously, the magneto-crystalline anisotropy also contributes to the effective anisotropy.

It is possible to use the relationship $K_{eff}.t = K_V.t + 2K_S$, to determine the thickness dependant (interfacial) and thickness independent (volume) contributions. The straight line graph that will be give as shown in Figure 3.3 will be used to analyse the contributions K_V and K_S. K_V corresponds to the slope of the straight line fit and K_S is given by the intercept with the y-axis.

Figure 3.4 shows the different responses of the strain (ε) and the anisotropy thickness product $K_{eff}.t$ to changes in thickness. Figure 3.4 (a) shows the evolution of lattice mismatch induced strain around t_c. The film is uniformly strained (below t_c) and relaxes with the inclusion of dislocations (above t_c). Figure 3.4 (b) shows the change in the anisotropy thickness product. We have not discussed the variable K_N which is the Néel contribution to interface anisotropy [6]. This is discussed in section 3.1.2. K_N is summed with the strain induced magnetoelastic

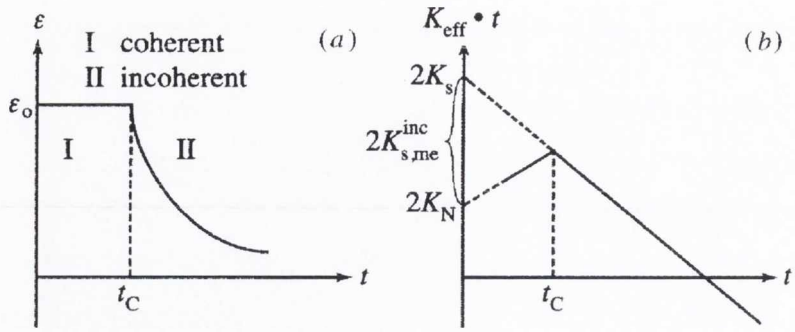

Figure 3.4: Magneto-elastic anisotropy above and below the critical thickness t_c. (a) The contribution to the strain ε, (b) The contribution to the anisotropy energy times layer thickness ($K_{eff}.t$) [3].

contribution $K^{inc}_{me,S}$.

In order to separate the contributions to K_S from strain induced anisotropy and the Néel type anisotropy, it is necessary to explore a system that allows for both coherent and incoherent growth modes. Cu/Ni is such a system: here the Néel anisotropy and the magneto-elastic anisotropy have opposite contributions to the overall anisotropy [18]. This leads to the graph shown in Figure 3.4 where there is a clear kink in the $K_{eff}.t$ vs. t curve. The interfacial contributions K_N and K_S can be extrapolated from fits like Figures 3.3 and equation 3.7.

We will explore amorphous systems in Chapter 4. In the case of amorphous alloys, it should not be possible to have a lattice mismatch since the alloy by definition has no crystal structure. In reality, these alloys should exhibit short range order at very small length scales (less than 1 nm).

In the Pd/CoFeB/Pd system magnetostriction and the elastic modulus have been measured. λ_{CoFeB} can be taken as $\sim 5 \times 10^{-6}$ [19][20] and E to be 160 GPa [20]. If we use these values and take t_c to be 1 nm we can get K_{me} in terms of the lattice mismatch, $K_{me} = 1.2 \times 10^{-3} \times \eta$ mJ/m^2. A "mismatch" of 1% at the interface can give 12 μJ/m^2. In [21], simulations which assumed elevated temperature during growth lead to thermal stresses at the interface after cooling to room temperature. This can give rise to magneto-elastic anisotropy. They estimated the temperature to be 400 K during growth.

3.2 Determination of K_V and K_S

The easiest way to calculate the anisotropies is from graphs of $K_{eff}.t = K_V.t + 2K_S$, as shown in Figure 3.3. K_S can be determined from the intercept and K_V can be calculated from the slope. It is generally impossible to properly account for surface morphology and K_S can not generally be broken into its constituent contributions i.e. magneto-crystalline or magneto-elastic. The determination can be made based to other factors, such as lattice mismatch. For example; the PMA in Co/Ni is magneto-crystalline in origin due to the small lattice mismatch, whereas in Co/Pd it is magneto-elastic due to the large mismatch. The origin of anisotropy contributions is important in analysing experimental results. In the systems studied in this thesis the anisotropy has differing origins: for Pd/CoFeB/Pd the anisotropy is believed to be magneto-elastic due to thermal stress; for the MgO/CoFeB/Pd and MgO/CoFeB/Pt the origin is unclear but believed to be magneto-crystalline due to oxygen bonding; for Pt/Co/Pt the origin is mostly magneto-elastic due to the lattice mismatch induced stress. In Co/Pd systems the magneto-elastic contribution dominates. During analysis we will simply state the contributions to the surface and volume anisotropies and compare their values. The effective anisotropy K_{eff} is calculated from easy and hard axis magnetisation measurements where we determine the anisotropy field $\mathbf{H}_a$ and the saturation magnetisation $\mathbf{M}_s$

$$\mu_0 \mathbf{H}_a = \frac{-2K_{eff}}{M_s} \tag{3.11}$$

This analysis should only be applied when it is straightforward to apply the field along the easy axis and hard axis. For systems with an arbitrary anisotropy axis the magnetisation must be measured along and perpendicular to that axis. This can be difficult experimentally, so we focus on systems with strong perpendicular anisotropy. The typical orders of magnitude for K_V and K_S are 1 MJ/m^3 and 1 mJ/m^2, respectively.

Bibliography

[1] Coey, J.M.D. *Magnetism and Magnetic Materials*. (2010).

[2] Alameda, J.M., G. D. L. R. L. Q. *Journal of Applied Physics* **52**(3), 2079–2081 (1981).

[3] Johnson, M.T., Bloemen, P.J.H., Den Broeder, F.J.A., De Vries, J.J. *Reports on Progress in Physics* **59**(11), 1409–1458 (1996).

[4] Farrow, R.F.C., Weller, D., Marks, R.F., Toney, M.F., Cebollada, A., Harp, G.R. *Journal of Applied Physics* **79**(8 PART 2B), 5967–5969 (1996).

[5] Daalderop, G.H.O., Kelly, P.J., Schuurmans, M.F.H. *Physical Review B* **44**(21), 12054–12057 (1991).

[6] Néel, Louis. *J. Phys. Radium* **15** (4), 225–239 (1954).

[7] D urr, H.A., Van Laan, G.D., Vogel, J., Finazzi, M., Goedkoop, J.B. *IEEE Transactions on Magnetics* **34**(4 PART 1), 1201–1203 (1998).

[8] Daalderop, G.H.O., Kelly, P.J., Den Broeder, F.J.A. *Physical Review Letters* **68**(5), 682–685 (1992).

[9] Daalderop, G.H.O., K. P. S. M. *Physical Review B* **41**(17), 11919–11937 (1990).

[10] Niranjan, M.K., Duan, C.-G., Jaswal, S.S., Tsymbal, E.Y. *Applied Physics Letters* **96**(22), 222504 (2010).

[11] Duan, C.-G., Velev, J.P., Sabirianov, R.F., Zhu, Z., Chu, J., Jaswal, S.S., Tsymbal, E.Y. *Physical Review Letters* **101**(13), 137201 (2008).

[12] Zhang, H., Richter, M., Koepernik, K., Opahle, I., Tasnadi, F., Eschrig, H. *New Journal of Physics* **11**, 043007 (2009).

[13] Shimabukuro, R., Nakamura, K., Akiyama, T., Ito, T. *Physica E: Low-Dimensional Systems and Nanostructures* **42**(4), 1014–1017 (2010).

[14] Weissmuller, J., V. R. K. D. Z. P. W. R. G. H. *Science* **300**(5617), 312–315 (2003).

[15] Van Der Merwe, J.H. *Journal of Applied Physics* **34**(1), 123–127 (1963).

[16] Chappert, C., Bruno, P. *Journal of Applied Physics* **64**(10), 5736–5741 (1988).

[17] Marcus, P.M., Moruzzi, V.L. *Solid State Communications* **55**(11), 971–975 (1985).

[18] Jungblut, R., Johnson, M.T., Aan De Stegge, J., Reinders, A., Den Broeder, F.J.A. *Journal of Applied Physics* **75**(10), 6424–6426 (1994).

[19] Aoshima, K., Hong, J., Kanai, H. *IEEE Transactions on Magnetics* **36**(5 I), 3226–3228 (2000).

[20] Wang, D., Nordman, C., Qian, Z., Daughton, J.M., Myers, J. *Journal of Applied Physics* **97**(10), 1–3 (2005).

[21] Jung, J.H., Lim, S.H., Lee, S.R. *Applied Physics Letters* **96**(4), 042503 (2010).

Chapter 4

Perpendicular magnetic anisotropy in CoFeB/Pd bi-layers

"as long as I can annoy you it is a success"

- Dr. Zhu Diao, an expert on stress

4.1 Introduction

There has been renewed interest recently in multilayer thin films possessing perpendicular magnetic anisotropy (PMA). These systems possess high uniaxial anisotropy along the film normal. Previously there was a focus on rare earth - transition metal alloys films, such as TbCoFe or GdCoFe in order to further advance magneto-optical recording [1]. This was followed by a shift to multilayer structures, such as $[Co/Pt]_n$ and $[Fe/Pt]_n$ [2]. Multilayer films offer better oxidation resistance, and have a higher signal in terms of magneto-optical (MO) recording. However MO recording suffers from a fundamental limit which prevents scaling to submicron dimensions.

The research from MO recording did have merits. The reason these layers are under investigation lately is because systems with PMA hold great promise for the research fields of spin transfer torque [3], high density magnetic recording [4] and electric field control of magnetic anisotropy [5].

In transition metal multilayers, magneto-elastic strain and interface anisotropy of ultra-thin layers add to the bulk magneto-crystalline anisotropy (see section 3.1). This gives rise to PMA. The effective anisotropy, K_{eff}, is well described in terms of volume and surface components (see equation 3.7). In layered structures, the effective anisotropy energy is an interplay between the volume anisotropy, K_V, and the surface anisotropy, K_S. Generally K_V for transition metal ferromagnets such as Fe, Co and Ni favours an in-plane easy axis, whereas K_S favours an easy axis perpendicular to the film plane (see Figure 3.3). By controlling precisely the layer thicknesses, one can tailor K_{eff} [6]. If K_{eff} is positive the easy axis will be perpendicular to the plane of the thin film.

CoPt and FePt alloys can also form tetragonal $L1_0$-ordered structures which possess extremely high bulk magneto-crystalline anisotropy, 4.5 MJ/m^3 and 6.6 MJ/m^3 respectively [7].

In order to form these phases a high annealing temperature and effective seed layers are required [8]. Multilayer structures have the benefit of possessing high perpendicular anisotropy at room temperature. This originates from the interfaces, rather than the bulk and does not require high temperature post-annealing in order to be realised.

For the case of spin transfer torque, these multilayers can provide a way to lower the critical current density for magnetisation switching, j_c. For in-plane magnetised films the current required for switching is given by [3]

$$J_{c0} = \frac{2e}{\hbar}\frac{\alpha}{\eta}\mu_0 M_s.t(H + H_{a||} + M_s/2)$$

whereas for a magnetic volume with perpendicular anisotropy the switching current is

$$J_{c0} = \frac{2e}{\hbar}\frac{\alpha}{\eta}\mu_0 M_s.t(H + H_{a\perp} - M_s)$$

Here α is the Gilbert damping parameter; η is the spin-transfer torque efficiency; t is the magnetic layer thickness; H is the applied field; $H_{a||}$ and $H_a \perp$ are the in-plane and out-of-plane anisotropies; M_S is the saturation magnetisation of the magnetic layer.

For the in-plane case, the magnetisation precesses about the demagnetizing field, and as a

result the averaging of the energy of this precession leads to the factor of 1/2 in front of the demagnetizing field $\mathbf{M}_S$ [9] [10]. The demagnetizing field term $\mathbf{M}_S/2$ is the largest term. The anisotropy field $\mathbf{H}_{a||}$ is small. The effective anisotropy is the sum of the in-plane anisotropy field $H_{as||}$ and the demagnetizing field. However, in the perpendicular case, the anisotropy field is of the same order of magnitude as the demagnetizing field, as seen in Chapter 3. As a result of this the magnetisation dynamics are different [3].

The effective anisotropy is given by the difference of the perpendicular anisotropy field $H_{a\perp}$ and the demagnetizing field. In the in-plane case the shape anisotropy must be overcome also, thereby making the switching process using perpendicular electrodes more efficient than the case of in-plane [3].

Perpendicular films have also been under investigation to see the effect of an electric field on the electronic structure of the interface (the electric field control of magnetic anisotropy) [11][5]. This is investigated in Chapter 5.

PMA can be investigated directly by means of a magnetometer such as a SQUID, but also by two indirect experimental techniques, magneto-optical Kerr effect (MOKE) [11] and extraordinary Hall effect (EHE) [12]. MOKE is an optical measurement technique which exploits different refractive indices for left and right hand circularly polarised light in a magnetic medium. However it is not sensitive to magnetisation below a certain depth, determined by the optical absorption. Extraordinary Hall effect has the advantage that, as an electrical measurement, it will probe the entire sample thickness (where the resistance of each layer and the interfaces are summed as parallel resistances). It is very sensitive to the component of magnetisation perpendicular to the film normal as discussed in section 2.4.3. This technique has been used extensively as a means to detect changes in ferromagnetism in dilute magnetic semiconductors by Hideo Ohno's group in Tohoku University Japan and more recently for detecting changes in magnetic anisotropy in a ferromagnet [13].

In multilayer thin films, the effective anisotropy (as discussed in section 3.1) can be analysed in the context of two anisotropy contributions, namely the volume anisotropy K_V and the surface

anisotropy K_S. This is approximated as

$$K_{eff} = K_V + 2K_S/t \tag{4.1}$$

where t is the magnetic layer thickness. The crossover thickness from in-plane to perpendicular anisotropy is given by $t = -2K_S/K_V$. In order to obtain the effective anisotropy we need to know the anisotropy field, $\mathbf{H}_a$, which is the field required to saturate the multilayer along the hard axis. We obtain K_{eff} from $\mathbf{H}_a$ via

$$\mu_0 \mathbf{H}_a = \frac{2K_{eff}}{M_s} \tag{4.2}$$

where M_s is the saturation magnetisation, see Figure 3.2.

We investigated the perpendicular anisotropy in CoFeB/Pd layers for the study of the effect an electric field on anisotropy. In order to make any qualitative judgement on any change of anisotropy induced by surface charging we first characterised the perpendicular anisotropy in ultra-thin single layers of CoFeB and Co. We then added an insulator directly in contact with the CoFeB layer to charge the interface. Samples were grown with the following structure; Si/SiO_2/underlayer/FM/cap. The underlayers used were Ta (5) /Pd (5) and MgO (1.4) (thicknesses in nm). FM layers were Co and $Co_{40}Fe_{40}B_{20}$. Pd was used as a cap layer.

4.2 Experimental methods

Samples were deposited by sputtering in the Shamrock Chamber A (see section 2.2.2) on 1" square Si wafers with 500 nm of thermally grown SiO_2. All growth rates were calibrated by fixed-time depositions and XRR thickness measurements, as described in section 2.4.1. Samples were generally unpatterned and extraordinary Hall effect measurements were performed using the geometry shown in Figure 4.1. Measurements were conducted in the R-T rig (described in section 2.4.2.

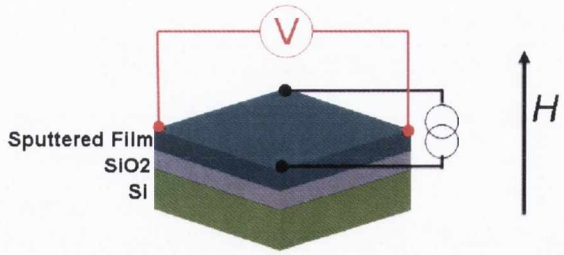

Figure 4.1: Schematic of the EHE measurement geometry. The film being measured was unpatterned and was 1" square. Samples were then measured in the R-T rig. The field was applied perpendicular to the film plane.

4.3 Buffer layer dependence

As outlined in section 3.1 the magnetic anisotropy is sensitive to the crystallographic structure. There have been strong differences in both surface and volume contributions to K_{eff} reported [14]. Therefore control of the crystal structure is required for each system under study.

We chose to grow a single Co layer on differing underlayers to verify this critical dependence on crystal structure. As reported before [6], Co/Pd multilayers have the highest PMA when they are oriented *fcc* [111] axis perpendicular to the plane of the film. Figure 4.2 shows EHE loops for a single 0.6 nm Co film on differing underlayers.

The results are dramatic. When grown directly on SiO_2 no perpendicular easy axis is observed, indicating that Co and Pd do not orient in the [111] direction. In order for Co to grow in the [111] direction it requires a [111] template. The underlying SiO_2 layer is amorphous.

Inserting a Ta buffer layer does not help stabilise the oriented *fcc* structure, the 5 nm Ta underlayer may also be poorly crystallised. The growth of a Pd interlayer on the Ta layer, however, does stabilise the PMA. Pd will grow in the [111] direction when grown on a Ta seed layer. This will give a [111] template for subsequent Co growth which will induce the stable *fcc* [111] growth of Co. This gives large perpendicular anisotropy, evidenced directly by the nice square hysteresis loop shown in Figure 4.2.

When grown directly on SiO_2, Pd (and most other metals) tends to grow firstly in the 3D island-mode. These islands grow and then form a continuous layer and is known as the Volmer-Weber growth mode [15]. The insertion of the Ta buffer layer allows for continuous [111]

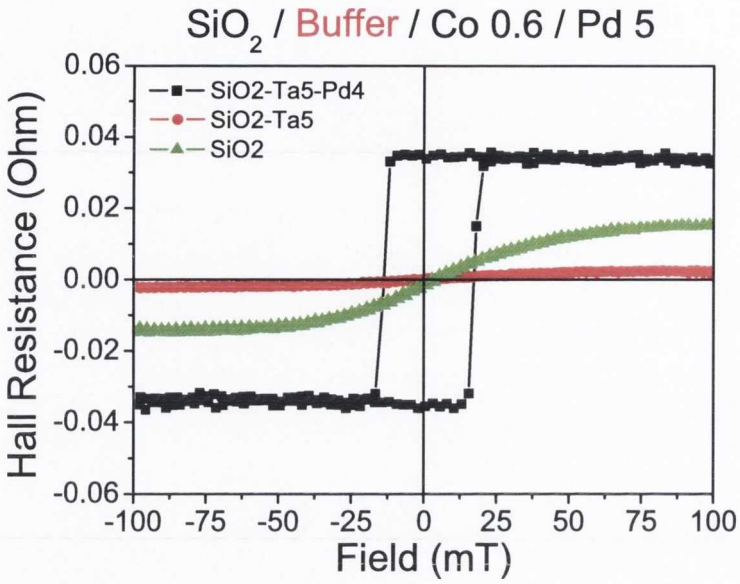

Figure 4.2: Buffer layer dependence of out of plane magnetisation in Co/Pd single film

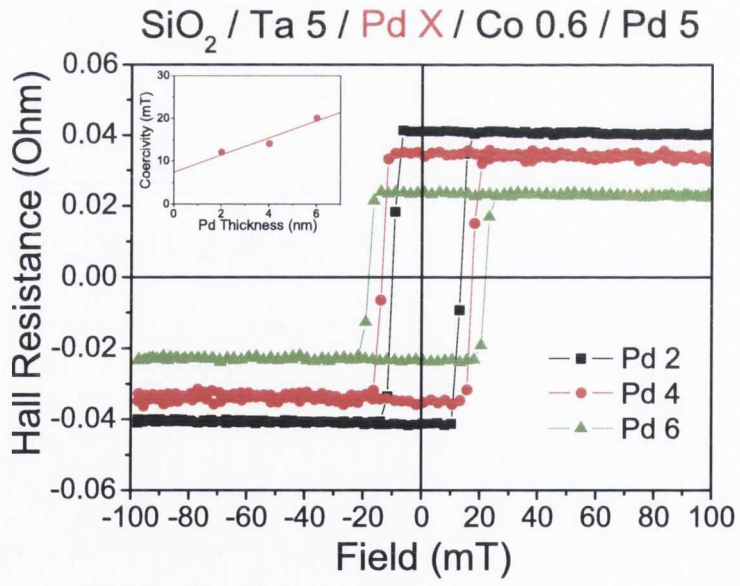

Figure 4.3: Pd underlayer thickness dependence of a Pt *t* / Co 0.6 nm / Pd 5 nm film. Increasing the underlayer thickness promotes better (111) texture (the applied . Inset: Coercivity as a function of Pd underlayer thickness with a linear fit

growth of Pd. It can be seen from this that the Pd underlayer is required for fully remanent PMA in the Co thin film system.

If we now vary the thickness of the Pd layer, as shown in Figure 4.3, we can see that we can vary the coercivity of the Co layer. The Hall resistance increases at lower Pd thickness due to increased current shunting through the Co layer. We attribute this increase in H_c to the improvement in [111] texture of Co as the Pd thickness is increased. The improved texture enhances the quality of the Co/Pd interface and leads to a larger interfacial anisotropy. In section 3.1.3 we calculated the anisotropy for a layer of Co grown on Pd assuming perfect and abrupt interfaces for both the coherent and incoherent regimes. Even though the system is in the incoherent regime, the lattice mismatch (11 %) will still induce a strain on the Co layer and lead to an interfacial anisotropy of 0.52 mJ/m^2 (see section 3.1.3).

4.4 Ferromagnetic layer thickness dependence

Next we vary the thickness of the Co layer; we can see from Figure 4.4 that the coercivity drops as the Hall resistance increases. We see an increase in Hall resistance due to the increase of magnetic material, but we also have less current shunting through the non magnetic layers. The increase in coercivity can be explained in terms of the competition between K_V and K_S, the volume and surface anisotropy respectively. At small thicknesses K_S will dominate the effective anisotropy, but as the thickness is increased the surface anisotropy contribution will fall off linearly as a function of t. This can be seen as a linear fall of the coercivity in Figure 4.4 inset. The high coercivity is an indication of the high quality of the interfaces in our sputtered Co/Pd layers. The extrapolated crossover thickness $t_\perp$ is about 1.3 nm. The crossover thickness correlates well to literature values of 1.1 nm for polycrystalline and 2 nm for epitaxial superlattices [16].

We also deposited $Co_{40}Fe_{40}B_{20}$ as the ferromagnetic metal in the Ta/Pd/FM/Pd sandwich. Due to the high boron content of this layer, the alloy is expected to be amorphous in the as-deposited state [17] regardless of the substrate.

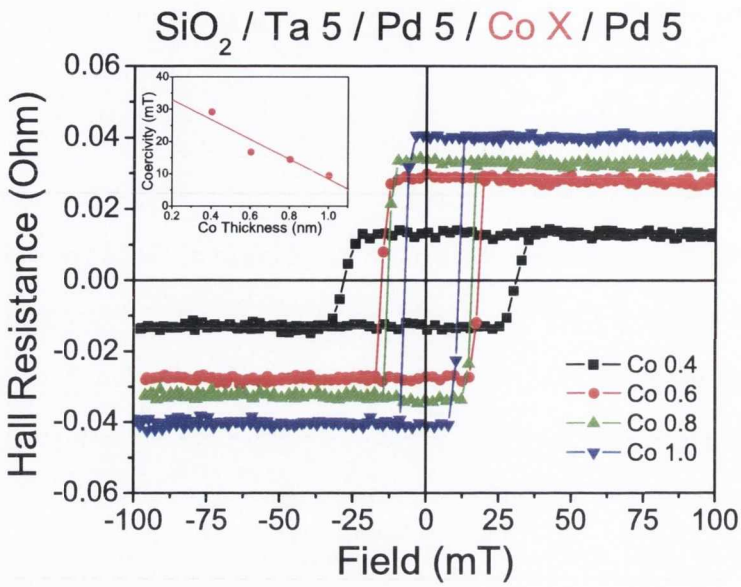

Figure 4.4: Ferromagnetic Co thickness dependence of Ta/Pd/Co/Pd. Increasing the Co thickness the coercivity falls linearly, due to increasing K_V contribution to the effective anisotropy (the applied field is along the film normal). Inset: Coercivity as a function of Co thickness with a linear fit

The results of the single layer are shown in Figure 4.5. It is clear from the EHE loops that between 0.6 nm and 0.8 nm there is a loss of the perpendicular anisotropy. The large dips observed at 0.8 nm and 1.0 nm are due to the in-plane anisotropic magnetoresistance (AMR) which is a signal of in-plane magnetic anisotropy [18]. It is possible that the magnetisation is not fully in-plane and that the magnetisation is pointing at some angle with respect to the film normal. Sharp switching in the EHE measurement indicates a strong perpendicular easy axis. If, however, the easy axis is along some arbitrary axis then H_c should increase and the hall resistance should continue to increase after H_c and saturate when the magnetisation has been saturated along the film normal. The lack of slope after H_c in Figures 4.4 and 4.5 indicate that we have an easy axis along the film normal, and not some arbitrary axis.

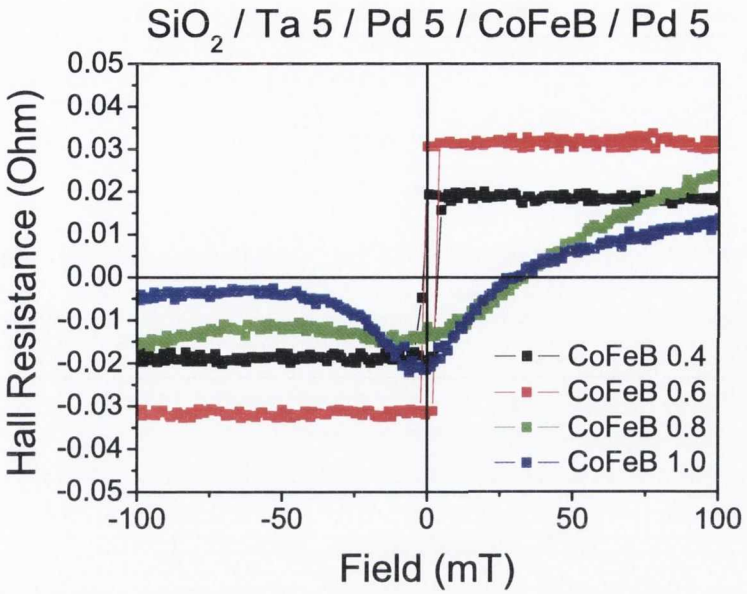

Figure 4.5: CoFeB thickness dependence of Ta/Pd/CoFeB/Pd. The coercvity falls to zero at a thickness of approx 0.7 nm. The applied field is along the film normal

4.5 Magnetisation Data

In order to fully quantify the anisotropy of the system it is necessary to obtain, from SQUID magnetometry measurements, the anisotropy field H_a. Magnetisation data from SQUID measurements is shown in Figure 4.6 for differing CoFeB thicknesses. Measurements were made with the field applied in the plane of the sample and with the field perpendicular to the sample. Samples were cut to 4×4 mm^2 for perpendicular measurements and 6×6 mm^2 for parallel measurement using an automatic wafer dicing saw (see section 2.2.8). The magnetic moment was divided by the magnetic volume (i.e. total CoFeB thickness) to determine the magnetisation of each sample.

The literature value of $\mathbf{M}_S$ value for $Co_{40}Fe_{40}B_{20}$ is 1.1 MA/m in the as-deposited state [19]. However we see an elevated value of approximately 1.5 MA/m, which could be explained by an induced moment on the Pd atoms adjacent the CoFeB layer. Harzar *et al.* [20] observed an increase in the saturation magnetisation was observed as Co thickness was reduced in Co/Pd multilayers. They found an increase of $\mathbf{M}_S$ from 1.4 MA/m (157 emu/g) to 2.2 MA/m (250

emu/g). If we assume that we can induce a moment in the Pd layer, we can use the literature value of $\mathbf{M_S}$ (1.1 MA/m) to determine the magnetisation of the Pd layer (0.4 MA/m) as $M_{measured} = M_{CoFeB} + M_{Pd}$. We have two interfaces with Pd, so assuming equal induced moments in each we have 0.2 MA/m for one interfacial monolayer.

Taking the density of Pd to be 1.2 $\times 10^4$ kg/m^3 and a molecular weight of 106.42 g/mol, we can use the following conversion to determine the μ_B per Pd atom,

$$\mu_B/formula = \mathbf{M} \times \frac{5585 \times \rho}{M_r}$$

where ρ is the density and M_r is the molecular weight.

The induced moment per Pd atom is 0.63 μ_B[1]. This is within the range of the induced moment of 0.4 μ_B on Pd in the Pd/Co/Pd system [21] and 1.2 μ_B $\pm$ 0.6 in the Au/Co/Pd/Au system [22].

For $Co_{40}Fe_{40}B_{20}$ with $\mathbf{M}_S$ we obtain 1.34 μ_B per $Co_{40}Fe_{40}B_{20}$ unit.

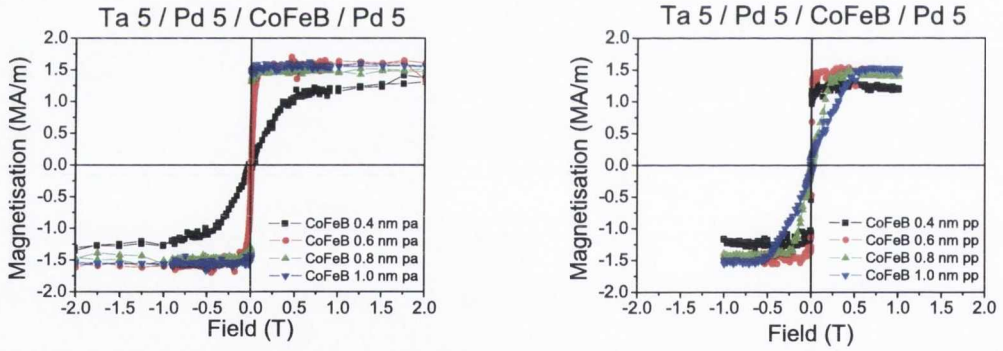

Field parallel to the sample plane

Field perpendicular to the sample plane

Figure 4.6: SQUID measurements for differing CoFeB thickness sandwiched in Ta/Pd/CoFeB/Pd.

We take the experimentally determined saturation magnetisation of CoFeB from each thickness (~1.5 MA/m) to work out the effective anisotropy and determine the interfacial and volume contributions, K_V and K_S. Using the anisotropy field H_a we can determine K_{eff}. We then plot

[1] this is the moment induced on one Pd monolayer

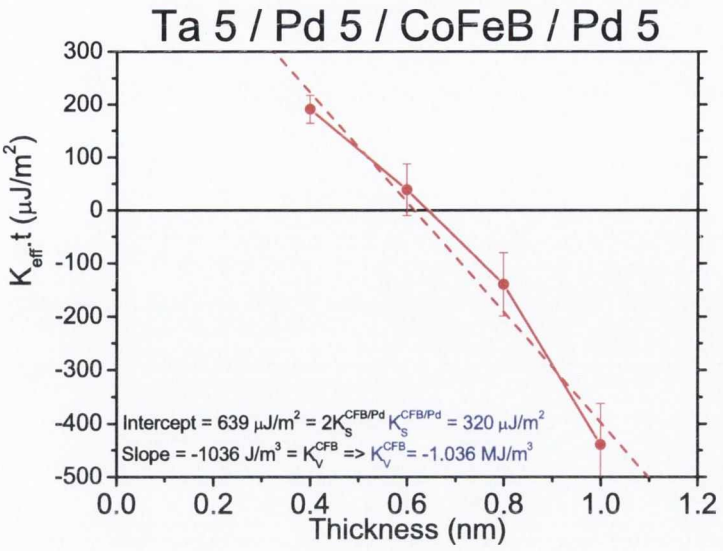

Figure 4.7: Effective anisotropy thickness product versus CoFeB thickness for the Pd/CoFeB/Pd sandwich.

the anisotropy thickness product versus thickness in Figure 4.7. We obtain a surface anisotropy energy of 0.32 $\pm$ 0.03 mJ/m^2, which is less than that of the Co/Pd interface [23]. We obtain a volume anisotropy of -1.05 $\pm$ 0.08 MJ/m^3. This is difficult to compare to Co, due to the amorphous nature of the CoFeB layer. Engel *et al.* showed that the volume anisotropy in Co depended greatly on the crystal structure of the Co layer [16], [14], ranging from -0.5 to -4.5 MJ/m^3, whereas the surface anisotropy was 0.63 mJ/^{2} regardless of crystal structure.

In Chapter 3 we calculated the shape anisotropy through equation 3.4. For a saturation magnetisation of 1.5 MA/m, K_{sh} is equal to -1.35 MJ/m^3. We can compare this to the volume anisotropy from Figure 4.7, -1.05 MJ/m^3. The values obtained from the slope and the calculated shape anisotropy are quite close.

The amorphous nature of the CoFeB layer would also imply that there should be no magneto-elastic contribution to the effective anisotropy, since we cannot obtain a lattice mismatch we cannot induce a growth related stress. However simulations, [24], yield that there can be thermal stresses in multilayer structures, see also section 3.1.3. These stresses could account for the difference between the calculated shape anisotropy and the volume anisotropy from Figure 4.7.

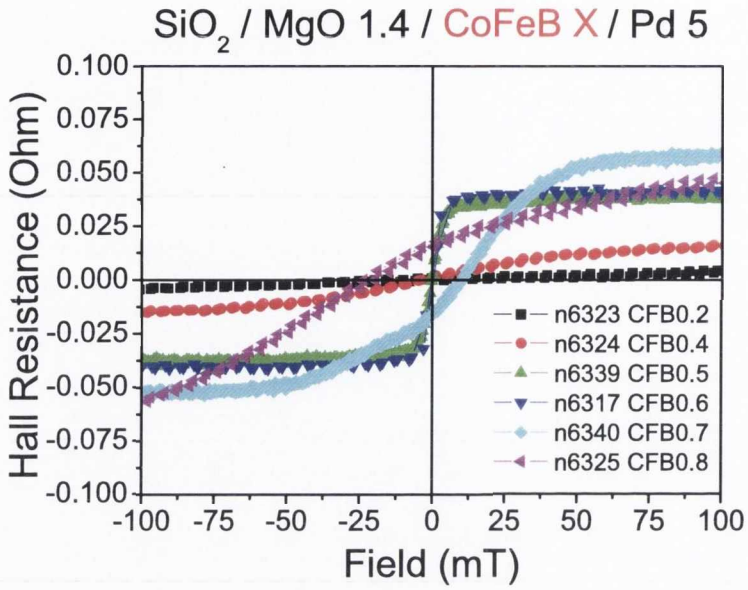

Figure 4.8: Room temperature extraordinary Hall resistance versus CoFeB thickness for the MgO/CoFeB/Pd sandwich

4.6 MgO/CoFeB/Pd

Since the CoFeB layer is amorphous, the interfacial anisotropy should also be independent of the underlayer as we cannot have strong magneto-elastic stress. If we replace the lower Pd layer (or the upper Pd layer) we would expect to obtain the same contribution as from a single interface. We replaced the Ta/Pd underlayer with a seed layer of MgO, a material commonly found in magnetic tunnel junctions.

We varied the CoFeB thickness in the MgO/CoFeB/Pd system. The effect of replacing the lower Pd by MgO was the loss of coercivity in the magnetic layer; often a signature of superparamagnetism. An EHE plot of data for different CoFeB thicknesses is shown in Figure 4.8. It is possible for a layer to possess perpendicular anisotropy while still being superparamagnetic. The magnetisation will simply fluctuate between two configurations on the perpendicular axis. It is clearly noticeable that there is a perpendicular easy axis at 0.5 and 0.6 nm. The distortion of the curve at t = 0.7 and t = 0.8 nm stems from AMR in the CoFeB layer, indicating that the magnetisation is in-plane. This is consistent with CoFeB grown on MgO as seen in Refs. [25] and

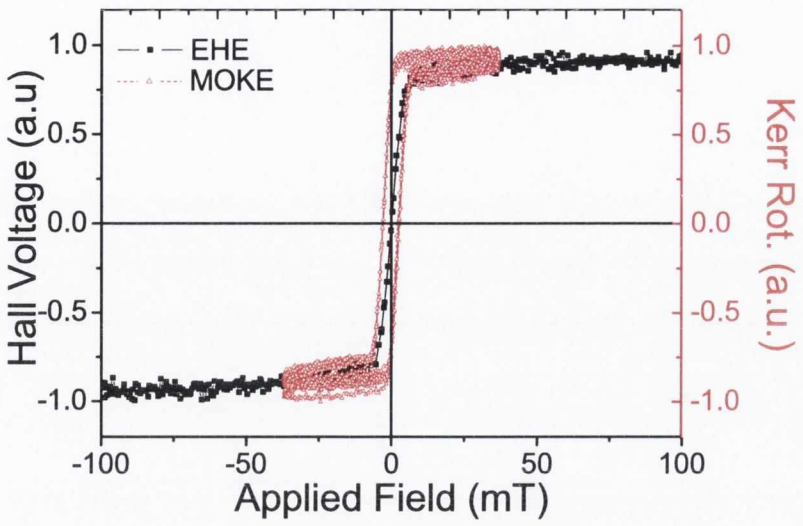

Figure 4.9: Comparison of magneto-optical Kerr effect and extraordinary Hall effect loops for the MgO/CoFeB/Pd sandwich.

[26], where CoFeB is expected to stay superparamagnetic up to a thickness of 1 nm. The CoFeB layer should be superparamagnetic at all thicknesses investigated here. It is clear that a perpendicular easy axis exists which we believe is induced by the Pd layer. Recently, a high quality MgO interface is believed to give very high anisotropies [13] [27]. The MgO grown directly on SiO_2 is not of very high quality (see Figure 4.10), so we infer that the anisotropy in this system is originating from the CoFeB/Pd interface. This system is ideal to investigate the electric field modification of anisotropy. The origin of the anisotropy in this system is ambiguous: it could be magneto-elastic due to thermal stress during growth; or it could be magneto-crystalline due to the bonding of oxygen at the MgO interface; the induced moment on Pd suggests that there could be a magneto-crystalline contribution to the anisotropy.

If we look at MOKE loops (shown in Figure 4.9) for the MgO /CoFeB 0.6 / Pd 5 nm sample we can see a small coercivity and some remanence. The frequency of the field sweep in the MOKE setup is 387 Hz. This implies that on the $\sim$ ms timescale the magnetisation is blocked. In the EHE measurement (where the field is swept over the course of a few minutes) it is not.

A superparamagnetic particle will display paramagnetic behaviour above its blocking tem-

perature, T_B, [28]. This temperature is determined by the particles anisotropy energy ($K_{eff}V$) in relation to the thermal energy k_bT The blocking temperature is also function of the measurement time. If the measurement time is small enough, such as in the MOKE measurement above, the particle can become blocked and exhibit hysteresis.

By conducting low temperature measurements we determined the blocking temperature, T_B, of the superparamagnetic CoFeB to be $\sim$ 230 K from electrical EHE measurements at differing temperatures. Below T_B the superparamagmetic CoFeB exhibits ferromagnetic behaviour (i.e. it has hystersis).

We can also approximate the blocking temperature from the MOKE measurement. T_B is also dependant on measurement time, τ_m. It is clear from Figure 4.9 that, for the high frequency MOKE measurement, the CoFeB layer is blocked (i.e. its blocking temperature for that frequency of measurement is above 300 K).

We can determine the blocking temperature as a function of frequency using the following

$$T_B = \frac{\Delta E}{ln(\tau_m/\tau_0)k_b} \tag{4.3}$$

where ΔE ($=K_{eff}.V$) is the energy barrier detemined by the anisotropy and the volume of the superparamagnetic particle, τ_m is the measurement time, τ_0 is the attempt time (taken to be $\sim 10^{-9}$ seconds[2]) and k_b is Boltzmann's constant.

Taking τ_m to be 1/387 which is the time taken for a full sweep from -100 to 100 mT, and taking T_B at 350 K[3] we obtain ΔE to be $4361.k_b$.

If we now use this value of ΔE to calculate T_B when the measurement time is considerably increased $\sim$ 60 seconds. The we get T_B equal to 176 K. The value obtained from sample cooling and using a fixed measurement time was 230 K.

To investigate the crystal structure of MgO we grew samples with a thick underlayer, MgO 30 / CoFeB 0.6 / Pd 5 nm, and investigated the crystal structure by high angle XRD. A weak [001] texture was observed from the rocking curve. This indicates that our grains are not well

[2]the attempt time is related to the FMR frequency, in the region of a few GHz

[3]the marked hysteresis means that T_B of the CoFeB layer is above room temperature

orientated with respect to each other. The extraordinary Hall effect response was the same, with a sharp switch about zero field. From the rocking curve data the FWHM was 6°. From the 2θ data the FWHM was 0.71°.

Using the 2θ FWHM and Scherrers formula,

$$t = \frac{K\lambda}{B\cos\theta} \tag{4.4}$$

where t is the grain size in the direction normal to the sampling plane, K is a geometrical constant (which we take as 0.9), λ is the wavelength of radiation used (in our case 0.154 nm, B is the FWHM in radians and θ is the diffraction angle. From the FWHM data we obtain t = 9.6 nm for 30 nm of MgO. Since the overall thickness of the MgO layer is 30 nm, it is clear that the [001] texture is not pronounced throughout the layer. The [001] texture of MgO implies that the CoFeB layer grows amorphous as seen in the case of MgO magnetic tunnel junctions [29]. The rocking curve gives an indication of the misorientation of the grains in the layer, the FWHM here is 6° which means our grains are not well orientated with respect to each other.

Similarly, to investigate the crystal structure of the Pd layer, we deposited a sample with a thick Pd layer, MgO 1.4 / CoFeB 0.6 / Pd 15 nm, and examined the crystal structure by XRD. A strong [111] texture was observed from the rocking curve which is consistent with the appearance of PMA in the system. From equation 4.4 we obtain t = 11 nm. The grains are almost comparable with the thickness of the layer indicating the strong [111] orientation of the Pd layer. The FWHM of the rocking curve was 5.2° which indicates that the mosaic spread of the layer is similar to that of the MgO. This is to be expected since the misorientation of the grains will generally follow from the MgO buffer layer. In terms of the extraordinary Hall effect response, no qualitative difference was found with either the thick MgO or the thick Pd layer. The XRD data from the rocking curves are shown in Figure 4.10.

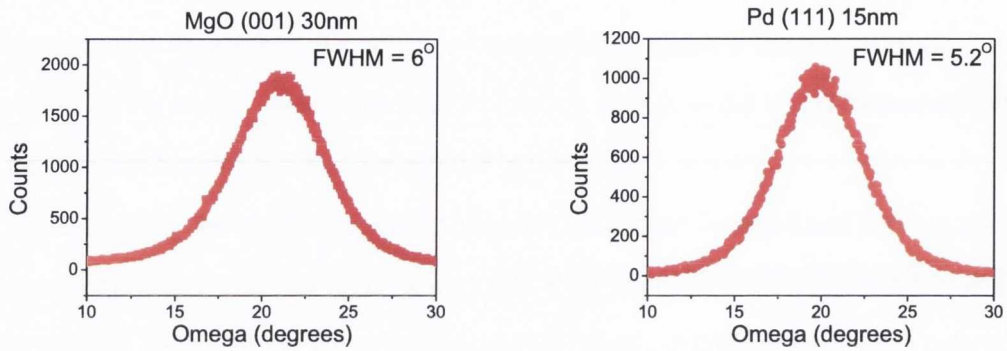

Figure 4.10: Rocking curve and FWHM for thick MgO and Pd layers

4.7 Conclusion

Clear evidence is found for perpendicular magnetic anisotropy in the Pd/CoFeB/Pd bi-layer system up to a CoFeB thickness of 0.6 nm. From room temperature magnetisation data the interfacial anisotropy was found to be 0.32 mJ/m^2 and the volume anisotropy was -1.0 MJ/m^3.

Using M_S and equation 3.4 we find a shape anisotropy of -1.35×10^6 J/m^3. For the contribution of magneto-elastic to the effective anisotropy we would use equation 3.7, but due to the amorphous nature of CoFeB there should be no stress on the film. For the case of CoFeB sandwiched by an MgO buffer and a Pd cap layer, we find a superparamagnetic easy axis along the film normal. There is a contribution from the CoFeB/Pd interface which gives a superparamagnetic easy axis at 0.5 - 0.6 nm.

X-ray studies showed a weak [001] texture in the MgO seed layer and a strong [111] texture in the Pd layer. The [001] MgO seed layer allows for the amorphous growth of CoFeB, whereas the [111] texture of the Pd layer gives rise to the perpendicular anisotropy seen when the CoFeB layer is 0.5 - 0.6 nm. The superparamagnetic nature of the CoFeB was investigated by low temperature EHE measurements and the blocking temperature was determined to be 230 K. The blocking temperature, T_B, of the MgO/CoFeB/Pd system in high frequency fields lies above room temperature.

In the sputtered MgO/CoFeB/Pd system, where the CoFeB layer is amorphous, the CoFeB

appears to be superparamagnetic at room temperature. From the blocking temperature measurements we can estimate the size of the superparamagnetic entity. The energy barrier ($K_u.V$) at the blocking temperature is equal to $k_b.T_B$. Assuming an anisotropy value between 10^3 and 10^6 we obtain a superparamagnetic volume between 14 nm^3 and 1.4 nm^3. Since our deposited layer was 0.6 nm thick, the lower value of 1.4 nm^3 seems reasonable for 3D island like growth of out CoFeB layer. Thus it seems from the evidence from EHE measurements and the above estimation that the CoFeB layer is in fact superparamagnetic on MgO.

Bibliography

[1] Sakurai, Y., Onishi, K., Numata, T., Tsujimoto, H., Saiki, K. *IEEE Transactions on Magnetics* **MAG-19**(5), 1734–1736 (1983).

[2] Lassri, H., Abid, M., Krishnan, R., Fnidiki, A., Teillet, J. *Journal of Magnetism and Magnetic Materials* **172**(1-2), 61–68 (1997).

[3] Mangin, S., Ravelosona, D., Katine, J.A., Carey, M.J., Terris, B.D., Fullerton, E.E. *Nature Materials* **5**(3), 210–215 (2006).

[4] Hellwig, O., Hauet, T., Thomson, T., Dobisz, E., Risner-Jamtgaard, J.D., Yaney, D., Terris, B.D., Fullerton, E.E. *Applied Physics Letters* **95**(23), 232505 (2009).

[5] Maruyama, T. and Shiota, Y. and Nozaki, T. and Ohta, K. and Toda, N. and Mizuguchi, M. and Tulapurkar, A. A. and Shinjo, T. and Shiraishi, M. and Mizukami, S. and Ando, Y. and Suzuki, Y. *Nature Nanotechnology* **4**(3), 158–161 (2009).

[6] Carcia, P.F. *Journal of Applied Physics* **63**(10), 5066–5073 (1988).

[7] Coey, J.M.D. *Magnetism and Magnetic Materials*. (2010).

[8] Farrow, R.F.C., Weller, D., Marks, R.F., Toney, M.F., Cebollada, A., Harp, G.R. *Journal of Applied Physics* **79**(8 PART 2B), 5967–5969 (1996).

[9] Sun, J.Z. *Physical Review B - Condensed Matter and Materials Physics* **62**(1), 570–578 (2000).

[10] Katine, J.A., Albert, F.J., Buhrman, R.A., Myers, E.B., Ralph, D.C. *Physical Review Letters* **84**(14), 3149–3152 (2000).

[11] Weisheit, Martin and Faehler, Sebastian and Marty, Alain and Souche, Yves and Poinsignon, Christiane and Givord, Dominique. *Science* **315**(5810), 349–351 JAN 19 (2007).

[12] Fowley, Ciaran and Decorde, Nicolas and Oguz, Kaan and Rode, Karsten and Kurt, Huseyin and Coey, J. M. D. *IEEE Transactions on Magnetics* **46**(6), 2116–2118 JUN (2010).

[13] Endo, M. and Kanai, S. and Ikeda, S. and Matsukura, F. and Ohno, H. *Applied Physics Letters* **96**(21) MAY 24 (2010).

[14] Johnson, M.T., Bloemen, P.J.H., Den Broeder, F.J.A., De Vries, J.J. *Reports on Progress in Physics* **59**(11), 1409–1458 (1996).

[15] Campbell, C.T. *Surface Science Reports* **27**(1-3), 1–111 (1997).

[16] Engel, B.N., England, C.D., Van Leeuwen, R., Nakada, M., Falco, C.M. *Journal of Applied Physics* **69**(8), 5643–5645 (1991).

[17] Cardoso, S., Cavaco, C., Ferreira, R., Pereira, L., Rickart, M., Freitas, P.P., Franco, N., Gouveia, J., Barradas, N.P. *Journal of Applied Physics* **97**(10), 1–3 (2005).

[18] Gerber, A., Milner, A., Karpovsky, M., Lemke, B., Habermeier, H.-U., Tuaillon-Combes, J., Ngrier, M., Boisron, O., Mlinon, P., Perez, A. *Journal of Magnetism and Magnetic Materials* **242-245**(PART I), 90–97 (2002).

[19] Hayakawa, J., Ikeda, S., Lee, Y.M., Sasaki, R., Meguro, T., Matsukura, F., Takahashi, H., Ohno, H. *Japanese Journal of Applied Physics, Part 2: Letters* **44**, L1267–L1270 (2005).

[20] Harzer, J.V., Hillebrands, B., Stamps, R.L., Güntherodt, G., England, C.D., Falco, C.M. *Journal of Applied Physics* **69**(4), 2448–2454 (1991).

[21] Pasyuk, V.V., Lauter, H.J., Johnson, M.T., den Broeder, F.J.A., Janssen, E., Bland, J.A.C., Petrenko, A.V., Gay, J.M. *Journal of Magnetism and Magnetic Materials* **121**(1-3), 180–184 (1993).

[22] Beauvillain, P., Chappert, C., Grolier, V., Mégy, R., Ould-Mahfoud, S., Renard, J.P., Veillet, P. *Journal of Magnetism and Magnetic Materials* **121**(1-3), 498–502 (1993).

[23] Purcell, S.T., Johnson, M.T., McGee, N.W.E., Zeper, W.B., Hoving, W. *Journal of Magnetism and Magnetic Materials* **113**(1-3), 257–263 (1992).

[24] Jung, J.H., Lim, S.H., Lee, S.R. *Applied Physics Letters* **96**(4), 042503 (2010).

[25] Feng, G., Van Dijken, S., Coey, J.M.D. *Journal of Applied Physics* **105**(7), 07C926 (2009).

[26] Jiang, L., Naganuma, H., Oogane, M., Ando, Y. *Applied Physics Express* **2**(8), 083002 (2009).

[27] Ikeda, S., Miura, K., Yamamoto, H., Mizunuma, K., Gan, H.D., Endo, M., Kanai, S., Hayakawa, J., Matsukura, F., Ohno, H. *Nature Materials* (2010).

[28] Brown, W.F. *Physical Review* **130**(5), 1677–1686 (1963).

[29] Yuasa, S., Suzuki, Y., Katayama, T., Ando, K. *Applied Physics Letters* **87**(24), 1–3 (2005).

Chapter 5

Electric Field Control of Magnetic Anisotropy

"Bricks and mortar, that's all we are"

- Aidan Byrne, freelance philosopher

5.1 Introduction

Magnetism in transition metals arises due to spin splitting of partly filled $3d$-orbitals. Ferromagnetism is therefore a phenomenon that arises from the electronic band structure of the transition metals Fe, Co and Ni. The number of electrons determines the magnetic properties in these transition metals and their alloys. The ability to control the electronic structure by controlling the bandfilling opens a new pathway to influence the magnetic properties of materials. This can pave the way to faster, low-power devices that use electric fields to manipulate magnetically stored information (either alone or with a combination of other switching techniques). Recently there have been some interesting experiments which use electric fields to modify the magnetic anisotropy in transition metal based devices. [1] [2] [3]. These experiments all involve a capacitor-like structure where at least one of the plates is a ferromagnet. This allows for electric field control of the magnetic properties by charging the surface of the plate material,

thereby altering the bandfilling. In a parallel plate capacitor, the charge on the plates is given by $Q = CV$, where Q is the charge per unit area and C is the capacitance. Capacitance is equal to $\varepsilon A/d$ where ε is the permittivity of the dielectric, A is the surface area of the plate and d is the thickness of the dielectric material between the two plates. When one plate of the capacitor is an ultra-thin ferromagnet, charging the capacitor will charge the ferromagnet/dielectric interface. Provided the ferromagnet is thin enough to give a high interface/volume ratio the charging can cause a significant change in the bandfilling and hence control the anisotropy. The amount of charge added to one atom of the ferromagnetic material at the interface is then

$$Q = \frac{\varepsilon S}{d} V \tag{5.1}$$

where S is the surface area for one atom, and d is, again, the dielectric thickness. For calculating S, if the system is cubic we can use the lattice constant of the ferromagnetic material, a, to determine the area, assuming one magnetic atom per unit cell.

Daalderop *et al.* calculated the magnetocrystalline anisotropy energy (see section 3.1), in ordered $L1_0$ transition metal alloys [4]. These $L1_0$ alloys exhibit strong uniaxial anisotropy. Anisotropy energy as a function of bandfilling, q, shows that the addition or subtraction of electrons can modify the anisotropy energy and the magnetic easy axis. In the case of FePt, an increase in q causes a decrease in anisotropy energy, eventually favouring in-plane easy axis when q is increased by one. For the case of FePd, an increase in q initially causes an increase in anisotropy energy then a decrease. The calculations are shown in Figure 5.1.

Ideally, it seems that integrating such a material into a capacitor structure would allow, very simply, for control over the band filling. It is not possible to influence the bulk material due to the screening effect in metals. When a electric field is applied to a metal, the build up of charges at the metal surface screens the electric field from the rest of the metal. As a result the effect of an electric field in a ferromagnetic material is confined solely to the surface and penetrates the first few monolayers until completely screened. The penetration depth is the Thomas-Fermi screening length, given by $\lambda_N = (e^2\rho/\varepsilon_0)^{-1/2}$ where ρ is the density of states at the Fermi level

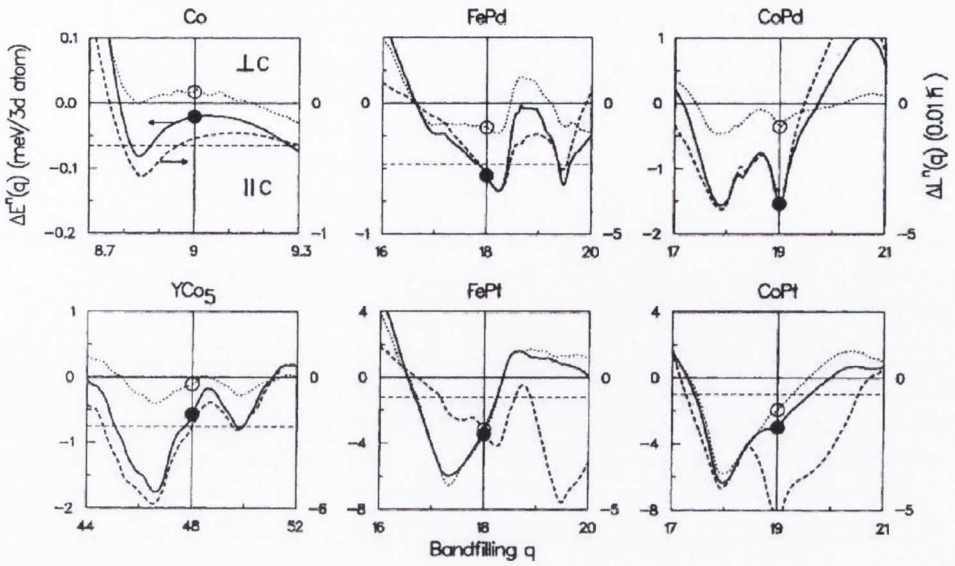

Figure 5.1: Magnetocrystalline anisotropy calculations as a function of bandfilling. The anisotropy axis is defined relative to the c-axis. As q is changed the anisotropy energy changes and the anisotropy axis can be in-plane, perpendicular to the c-axis (After [4]).

and ε_0 is the permittivity of free space. The number of electrons that can be added or removed from the surface also depends on the dielectric properties of the material used.

Therefore it would be necessary to be sure that the ferromagnetic films thickness is comparable to the screening length. Zhang showed that the spin polarisation and exchange constant J in a ferromagnet has an influence over this screening length [5]. As a result the electric field can, in fact, alter the spin polarisation at the ferromagnet surface. An accumulated moment at the interface builds up due to the fact that the electronic potential seen by spin-up and spin-down electrons is different.

From [5],

$$\lambda = \left\{ \frac{e^2}{\varepsilon_0} \frac{\rho^{\uparrow} + \rho^{\downarrow} + 4J\rho^{\uparrow}\rho^{\downarrow}}{1 + J(\rho^{\uparrow} + \rho^{\downarrow})} \right\}^{-1/2}$$

For materials with high J and high spin polarisation the screening length is larger than that of a normal metal. The authors then calculate the screening length for Ni, Co and Fe. As well as inducing charge in the interface atoms there is also an induced magnetisation. Any change in the magnetic moment can impact the anisotropy (section 3.1.1). The induced moments *per*

atom in the interface layer of Ni, Co and Fe were +0.12 $V_a/(t + 14.4)$, +0.088 $V_a/(t + 24.0)$ and -0.044 $V_a/(t + 20.8)$, where V_a is the applied voltage and t is the dielectric thickness in Å. If we were to apply 100 V applied voltage across a 200 nm dielectric layer the corresponding accumulated moment would be $\sim$ +0.005 μ_B per Ni and Co atom, and $\sim$ -0.0025 μ_B per Fe atom. Niranjan *et al.* later proposed that the spin-dependent screening effect would lead to changes in magneto-crystalline anisotropy at the interface [6].

Thus, in the calculated case an electric field applied to the surface of a ferromagnetic metal can impact the shape anisotropy by changing $\mathbf{M}_S$ and the magneto-crystalline anisotropy through the bandfilling. It is stressed that these arguments are only valid in the limit close to the screening length (1 monolayer). An electric field can never exist inside the bulk of a metal.

Nakamura *et al.* calculated the magneto-crystalline anisotropy of Fe[001] monolayers and found that the application of an electric field can modify the density of states about the Fermi level [7]. They find that one monolayer of Fe will favour out of plane magnetisation and that the application of an electric field can modify the orbital angular momentum and thus the anisotropy. They used *ab initio* calculations to determine the effect of an electric field on the band structure of the surface of an Fe monolayer, as well as Fe/MgO and MgO/Fe/MgO, where the hybridisation of Fe and O at the Fe/MgO interface was found to promote positive magneto-crystalline anisotropy energy [8].

Zhang *et al.* calculated the effect of charging surfaces in $L1_0$ materials, such as FePt and FePd, by density functional theory [9]. They determined that the effect of surface charging leads to a similar change in FePt as in CoPt. However the change in magneto-crystalline anisotropy in thin CoPt layers should be much greater than in FePt layers, because the bulk magneto-crystalline anisotropy in CoPt is less than FePt so the relative change will be larger. K_1 has values of 4.5 MJ/m^3, 6.6 MJ/m^3 and 1.8 MJ/m^3 for CoPt, FePt and FePd respectively. They showed that an electric field will modify the magneto-crystalline anisotropy by a finite value.

The calculations and predictions detailed above have shown that an electric field, applied to the surface of a ferromagnetic material, can modify the anisotropy as well as the magnetisation by causing a change in the electron density. This is a surface charging effect, caused by the pres-

ence of the electric field. The change in surface charge leads to an effect on the magnetisation and the magneto-crystalline anisotropy. It is noted that the magnetoelectric effect discussed here is different from that mediated by piezoelectric strain, as seen in multiferroic materials [10].

In 2007, Weisheit *et al.* experimentally demonstrated the controllable change of coercivity in $L1_0$-ordered FePt and FePd thin films by applying an electric field in an electrochemical cell [1]. A thin FePt (or FePd) layer formed one plate of the capacitor structure, while a Pt counter electrode was the other plate. For the case of these $L1_0$-ordered materials, adding electrons to the interface of FePt with the electrolyte served to lower the coercivity and in the case of FePd adding electrons had the opposite effect, increasing the coercivity. The calculations by Daalderop *et al.* for FePt and FePd showed that (Figure 1. in Ref. [4]) increasing the bandfilling from $q = 18$ to $q = 19$ should cause a decrease in K_{eff} for $L1_0$ FePt but for the case of $L1_0$ FePd we should see an initial increase followed by decrease after $q = 18.25$. For the amount of electrons added per unit cell in this case (0.015 electrons) the calculations and the experiment agree.

In 2009, Maruyama *et al.* demonstrated control of magnetic anisotropy in Fe upon an application of an electric field within a solid state capacitor structure [2]. In this case, the electric field was applied across 10 nm of MgO and a 1,500 nm thick spin-on dielectric layer of polyimide. The thick polyimide was used to provide a pin-hole free dielectric. One plate of the capacitor was formed with a few monolayers of Fe (below 0.6 nm in thickness) grown on atomically smooth [001] ordered Au, the other plate of the capacitor was indium-tin-oxide (ITO), a transparent conductor. This atomically smooth Au layer allowed for the growth of a continuous Fe monolayer whose band structure could be calculated. Calculations matched the experimental results [7]. More recently the Suzuki group demonstrated electric-field assisted magnetic switching using $Fe_{80}Co_{20}$ [11]. For this they first set their magnetic field to a value below the coercivity under conditions of elevated anisotropy (negative voltage) and switched the magnetisation by inverting the voltage bias. When the FeCo thickness was chosen correctly it was possible for the authors to switch "on and off" the PMA i.e. have a 100 % remanence when the FeCo/MgO surface was positively charged and have 0 % remanence when negatively charged.

All of these studies were all conducted using optical techniques, primarily by magneto-optical Kerr effect (MOKE) [1], [2], [11] but also Brillouin light scattering, [12]. In the cases of [2], [11] and [12] the electric field was applied across a 1500 nm thick polyimide layer. In their Au/Fe/MgO [2] system and Au/FeCo/MgO [11] system, the addition of electrons to the ferromagnetic/insulator interface served to decrease K_{eff}.

At present, only two references exist using extraordinary Hall effect as a detection mechanism for control of the magnetic properties of thin ferromagnetic films [13] and [3]. The group of Hideo Ohno in Japan have been using EHE to observe anisotropy changes in dilute magnetic semiconductors for many years [14]. As reported in Ref. [3] they were able to stabilise the perpendicular anisotropy in the $Co_{40}Fe_{40}B_{20}$ structure by annealing and manipulate the coercivity via applied electric field. The induced anisotropy is attributed to the hybridisation of Fe-O orbitals at the CoFeB/MgO interface, however the origin of PMA in this system is still not fully understood. What is known is that the B will not diffuse into high quality MgO barriers [15], so it will diffuse towards the Ta interface. With annealing the Ta layer does not crystallise (due to boron diffusion within it) and therefore it should not induce any magneto-elastic anisotropy in this system (see section 3.1). It seems therefore that the anisotropy in the system originates solely as a result of the CoFeB/MgO interface. Nevertheless, in this system the authors were able to observe a change in the perpendicular coercivity of CoFeB in electric fields up to 350 MV/m. Subsequently this interesting PMA material was integrated successfully into a magnetic tunnel junction (MTJ), the first perpendicular MTJ to have an all [001] texture. Strong [001] textured MgO is necessary for the high tunnel magnetoresistance (TMR) ratios observed in state-of-the-art MTJ's. Thus, the [001] texture of the MgO/CoFeB interface is therefore attributed also to the appearance of perpendicular anisotropy. In the Ta/CoFeB/MgO system, the addition of electrons to the ferromagnet served to decrease K_{eff}.

All of the above mentioned electric field experiments focused on [001] oriented Fe thin films or alloys containing Fe. There is, however, one report in the literature of a change in anisotropy upon application of electric field in a system that does not contain Fe [16].

Zhou *et al.* applied up to 3 V between a hard disk drive write head and the hard disk in a

System	Deposition Method	Fe-based?	Negative charging	Source
$L1_0$ FePt	MBE	Yes [001]	$K_{eff} \downarrow$	[1]
$L1_0$ FePd	MBE	Yes [001]	$K_{eff} \uparrow$	[1]
Au/Fe 2 ML/MgO	MBE	Yes [001]	$K_{eff} \downarrow$	[2]
Au/$Fe_{80}Co_{20}$/MgO	MBE	Yes [001]	$K_{eff} \downarrow$	[11]
CoCrPt	Sputtering	No [0001]	$K_{eff} \downarrow$	[16]
Ta/$Co_{40}Fe_{40}B_{20}$/MgO	Sputtering	Yes [001]	$K_{eff} \downarrow$	[3]

Table 5.1: Summary of different systems where electric field induced anisotropy changes are observed. The effect of negatively charging the interface of the ferromagnet and the insulator is given in the fourth column.

typical recording system [16]. They observed an improvement in signal to noise ratio when the written data was read back. This is attributed to a lowering of the coercivity during writing of the individual grains on the disk. The lower coercivity might be due to electric charge trapping at grain boundaries which locally lower K_{eff}. The edges with lower K_{eff} assist the switching of rest of the grain volume. Despite the fact that this was an indirect measurement of a change in coercivity the significant point is that the recording medium is a CoCrPt film i.e. there is no Fe present. The systems is hexagonal with a [0001] texture. Given this result it seems the band filling of any material can be altered by the charging of a thin film and this band filling subsequently affects the magnetisation. They indicated through simulated switching that the coercivity should reduce by $\sim$30 % in an applied electric field of 300 MV/m. There were no subsequently published experiments on non-Fe-based systems. In the CoCrPt granular system, the addition of electrons to the ferromagnet served to decrease K_{eff}.

Table 5.1 summarises, briefly, the various systems where an electric field has been shown to modify the magnetic anisotropy. The material composition of the system is given in the first column, the deposition method for the ferromagnetic layer is given in the second column, whether the system is Fe-based and the texture of the layers is given in column three, finally the effect of negatively charging the ferromagnet/insulator interface on the effective anisotropy (or coercivity) is given in the fourth column. The source is given in the fifth column.

There is also an electric field effect reported using the Stanford Linear Accelerator (SLAC), where the authors observe the distortion of the magnetic switching induced by an ultra-short

electron bunch [17]. The electromagnetic field of the electron bunch leaves a characteristic domain switching pattern in the plane of the sample which is investigated by scanning electron microscopy with polarisation analysis (SEMPA). Previously the authors had used longer pulse lengths to probe magnetisation switching and precession on the ps time scale. The switching of a 10 nm thick $Co_{70}Fe_{30}$ film was investigated. The magnetic switching of a 10 nm thick $Co_{70}Fe_{30}$ layer as seen on the ps time scale was distorted when the pulse length was reduced to the fs time scale. This is attributed to the increased electric field at the smaller time scale creating a transient anisotropy axis. The authors simulated their results with the electric and magnetic fields from the electron bunch used in the experiment and found that the pattern produced could be approximately matched. In their paper, they say that the electric field only distorts the electron valence cloud which indirectly changes the magnetisation through spin-orbit coupling. From Figure 2 in Ref. [18] the idea is that a pulsed electric field can cause a rotation of the magnetisation about a new anisotropy axis, the short duration of the pulse means that a full precession cycle is not completed. If the magnetisation precesses through the hard axis, when the electric field is removed it should relax back along the easy axis but pointing in the opposite way.

Full magnetisation switching using only electric fields has not been demonstrated, and as just mentioned it may only be possible with pulsed fields [19] [18]. Using a pulsed field to modify the direction of the anisotropy axis can cause switching through precession. Although the switching has been simulated, in order to cause magnetic switching we must have precession, which can only happen about an effective magnetic field. It is the cross product of the magnetisation with the effective field that causes a torque which is necessary for reversal. In the system where the magnetisation is not along the charge induced anisotropy axis switching is only realised if we have precession about the anisotropy axis. It is therefore not clear if surface charging with an electric field alone might allow for switching, even in the pulsed case. The effect of an electric field only affects the anisotropy energy, and as the anisotropy energy is changed the anisotropy axis will change. The anisotropy axis in turn dictates where the magnetisation vector will point. The electric field can cause switching between in-plane

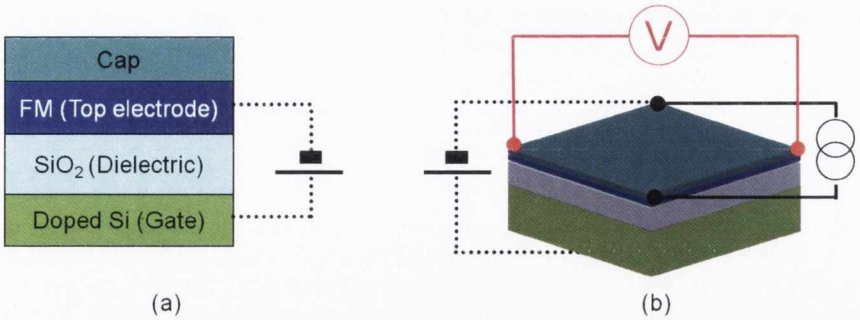

Figure 5.2: (a) Device structure for electric field measurements, the FM and doped Si form a capacitor across the SiO_2 dielectric layer. For the systems presented here we use a thin MgO buffer layer between the FM and the SiO_2. (b) EHE measurement geometry, the magnetic field is applied perpendicular to the film plane.

and out-of-plane anisotropy, but it can not directly switch the direction of magnetisation. The application of an electric field does not change the stability of the magnetisation direction along the anisotropy axis, i.e. the stability of both magnetisation directions parallel or antiparallel to the anisotropy axis are not affected.

In this chapter we set out to obtain a system that is suitable for the investigation of the electric field effect. Our solid state capacitor structure is shown in Figure 5.2 (a). In this system we can introduce any material as the top electrode. In all previous works the material under investigation has formed the bottom electrode. Materials with and without PMA, and even nonmagnetic materials can be investigated. To this end we deposit our samples on highly doped silicon and use the thermal oxide as a dielectric layer. This is the ideal solution in the Shamrock system because the typical insulators we deposit (MgO, Al_2O_3 and SiO_2) do not retain their dielectric properties when sputtered as thick layers. As an example, the insulating properties only exist for MgO when the RF-sputtered thickness is below 10 nm. We are free to deposit an additional (thin) material such as MgO, Al_2O_3 or AlN as a dielectric buffer layer on the SiO_2.

5.2 Experimental Methods

Samples were deposited by sputtering in the Shamrock Chamber A and B (see section 2.2.2) on highly doped Si wafers with 200 nm of thermally grown silicon dioxide serving as the dielectric material. All growth rates were calibrated by fixed-time depositions and XRR thickness measurements, as described in section 2.4.1. The geometry of the sample structure is shown in Figure 5.2. It is a solid state capacitor similar to that used in [11] and [3]. A thin MgO buffer layer was used to simulate a typical magnetic tunnel junction. One side of the capacitor is a thin film ferromagnet, for example Fe or CoFeB. The detection mechanism was the extraordinary Hall effect (described in 2.4.3) and the measurement geometry is shown in the right of Figure 5.2 (b).

The following samples were investigated, thickness in parentheses is in nanometers:

n++ Si / SiO_2 (200) / MgO (1.4) / Fe (t) / Pt (5)

n++ Si / SiO_2 (200) / MgO (2) / CoFeB (1) / Pt (3)

n++ Si / SiO_2 (200) / MgO (1.4) / CoFeB (0.6) / Pd (5)

n++ Si / SiO_2 (200) / MgO (2) / CoFeB (0.6) / Pd (5)

The samples were patterned into either 2 μm Hall bars by UV lithography (section 2.3.1) or to 3×3 mm^2 squares by direct laser lithography in the Heidelberg DLW66 tool in the Class 100 area of the CRANN clean room. The patterned devices were then extracted by wafer dicing (section 2.2.8). Transport measurements were conducted in the R-T rig (section 2.4.2) at room temperature and at the base temperature of the cryostat (12 K).

The electric field was applied between a scratched contact made to the highly doped silicon and the metal layers. A good contact to the Si was confirmed using two scratched contacts and checking electrical continuity between the two. A positive voltage implies that we are adding electrons to the MgO/CoFeB interface and a negative voltage implies we are removing electrons form the MgO/CoFeB interface. The 500 nm SiO_2 typically broke down above 500 MV/m ($\pm$100 V on the sample). In order to protect against high voltage discharges through the

end user all room temperature measurements were conducted inside a shielded box which was earthed directly to protective ground. For low temperature measurements, the signal ground was supplied by the current source signal low. Inside the cryostat it was not possible to connect to protective ground. Therefore in the low temperature case the applied voltage was kept below the highest voltage applied at room temperature, to prevent equipment damage.

5.3 MgO/Fe/Pt

In order to attempt to replicate the results of Maruyama *et al.* [2] we deposited the following stack on highly doped silicon wafers

$$\text{n++ Si / } SiO_2 \text{ / MgO / Fe } t \text{ / Pt}$$

where t = 0.4, 0.6, 0.8 and 1.0 (nm). The MgO was chosen to obtain a [001] texture of the Fe layer and the Pt cap was chosen to help stabilise any perpendicular anisotropy. Samples were deposited onto 25.4×25.4 mm^2 wafers. MgO was deposited in Chamber B, while Fe and Pt were deposited in Chamber A. After MgO deposition samples were held under high vacuum in the loadlock for approximately 30 minutes (the time required to deposit MgO on all wafers). The Fe and Pt layers were then deposited in Chamber A. Total time for processing all of the samples was about 1 hour.

The extraordinary Hall effect (EHE) curves, for 2 μm Hall bars, at room temperature are shown in Figure 5.3. There is no visible hysteresis in any Fe thickness, indicating that there is no strong perpendicular anisotropy in the as-deposited state. This is due to the large shape anisotropy of Fe. With $\mathbf{M}_S$ of 1.7 MA/m the shape anisotropy (which must be overcome in order to stabilise the perpendicular easy axis and give hysteresis) is quite large, $K_{sh}=\frac{1}{2}\mu_0\mathbf{M}_S^2$ = 1.8 MJ/m^3. As the Fe thickness is increased beyond 0.4 nm we begin to see anisotropic magnetoresistance (AMR) peaks consistent with an in-plane magnetic easy axis. The AMR will appear whenever the magnetic easy axis is not aligned with the applied field axis. It can be seen upon inspection of Figure 5.3 there is a change of slope for the 0.4 nm Fe layer, this is attributed

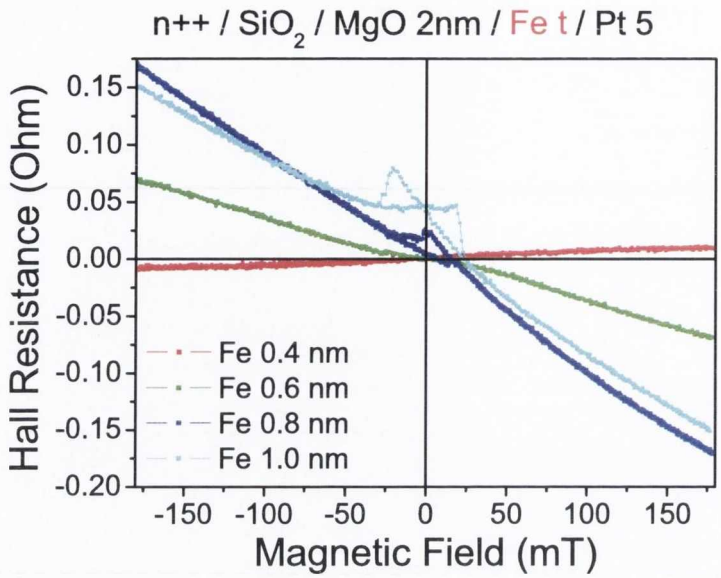

Figure 5.3: EHE curve responses for differing Fe thickness's in the MgO/Fe/Pt system. The field was applied perpendicular to the film plane. The sign change of the slope for Fe 0.4 nm is described in the text.

to a change in the Hall response of Fe nanoparticles and the presence of the MgO interface. It is possible that the different interfaces of Fe will give different signs of the extraordinary Hall coefficient [20] [21].

Figure 5.4 also shows the effect on the EHE curve of an electric field applied over 200 nm of SiO_2. The magnetisation along the perpendicular axis can be saturated at high field (<200 mT). The EHE signal is small because most of the current flows through the Pt cap layer. We applied a maximum field of 0.5 V/nm or 500 MV/m. There is no change in either the saturation field of the 0.4 nm Fe layer or the slope of the Hall response within the noise or error of the measurement. The authors of Ref. [2] observed a change in slope of the Kerr effect hysteresis loop upon application of an electric field. In their case the Fe was a continuous layer, with well defined [001] growth on atomically smooth Au.

For all thicknesses of Fe (Figures 5.4 to 5.7) we can see no electric field effect on the anisotropy of the material. A change in anisotropy would be indicated by either the appearance of coercivity or a change in slope of the EHE curve about zero field. It is noted that the electric

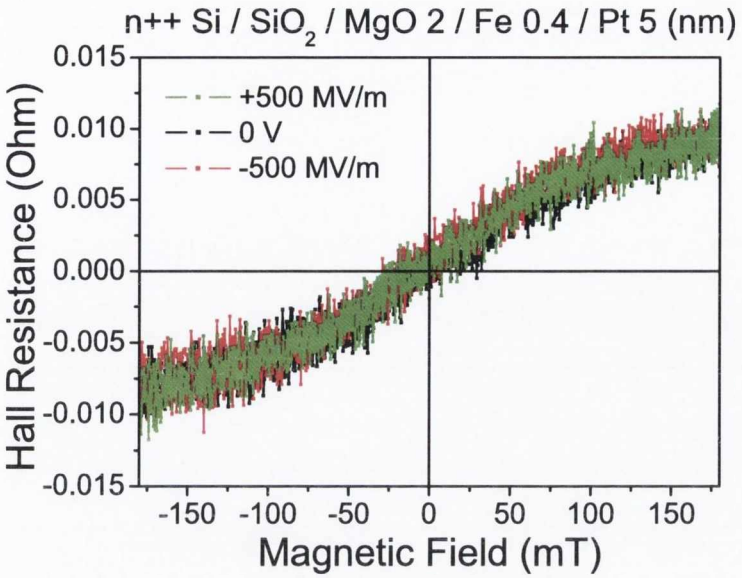

Figure 5.4: EHE curve responses for differing voltages applied to the MgO / Fe 0.4 nm / Pt system. The magnetic field is applied perpendicular to the film plane

field applied is quite large, larger than was applied in the case of [2]. There, the authors apply a maximum electric field of 130 MV/m and observe a change in the anisotropy of their thin Fe film. They also calculate that 200 V applied in their system corresponds to a change of 0.0017 electrons per Fe atom.

This was calculated using the following equation

$$Q = \frac{\varepsilon_0 \varepsilon_{MgO} \varepsilon_{Polymide} a_{Fe}^2}{\varepsilon_{MgO} d_{polyimide} + \varepsilon_{Polyimide} d_{MgO}} V \tag{5.2}$$

where the dielectric constants are ε_{MgO} = 9.8, $\varepsilon_{Polyimide}$ = 3.4, the lattice parameter a_{Fe} is 0.286 nm and the layer thickness's are d_{MgO} = 10 nm and $d_{polyimide}$ = 1500 nm. 200 V was the maximum voltage they applied.

Using the same equation but substituting the dielectric constant and thickness of SiO_2, ε_{SiO_2} = 3.9 d_{SiO_2} = 200 nm, at 100 V we obtain 0.0075 electrons per Fe atom. However, since there is no discernible change in perpendicular magnetic anisotropy from the EHE measurement we cannot comment on this. In our system the use of thermally grown SiO_2 as a dielectric allows

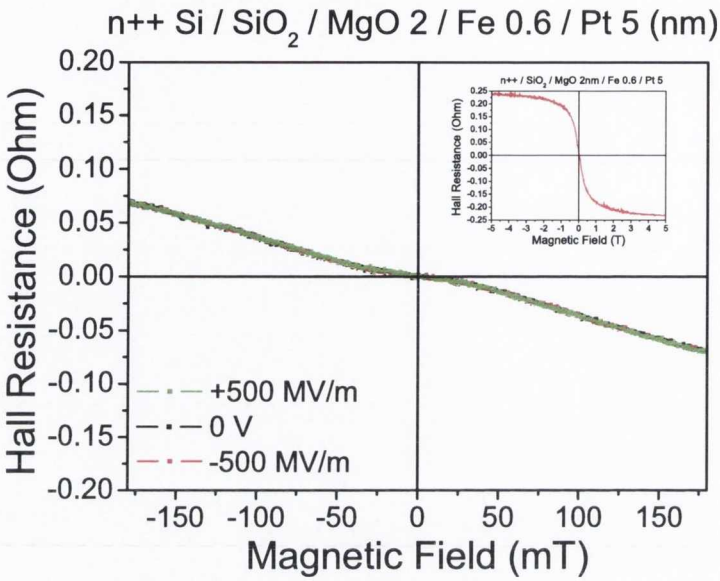

Figure 5.5: EHE curve responses for differing voltages applied to the MgO / Fe 0.6 nm / Pt system. The inset shows high field extraordinary Hall effect. The magnetic field is applied perpendicular to the film plane

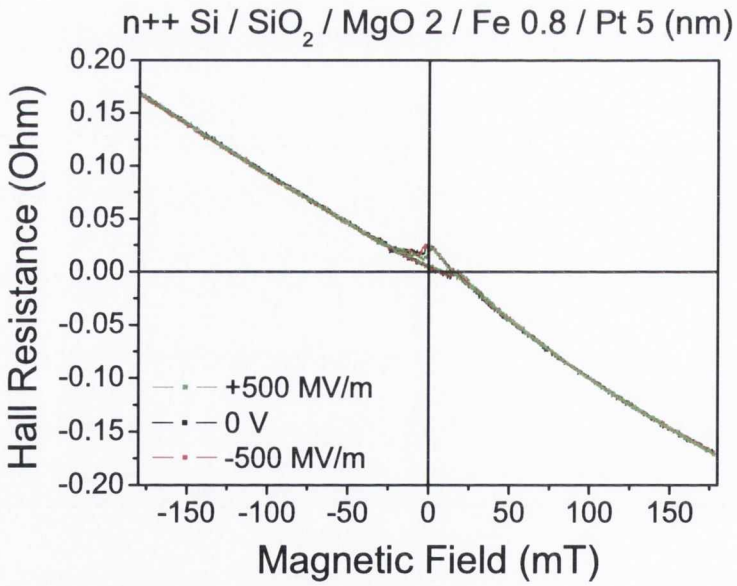

Figure 5.6: EHE curve responses for differing voltages applied to the MgO / Fe 0.8 nm / Pt system. The magnetic field is applied perpendicular to the film plane

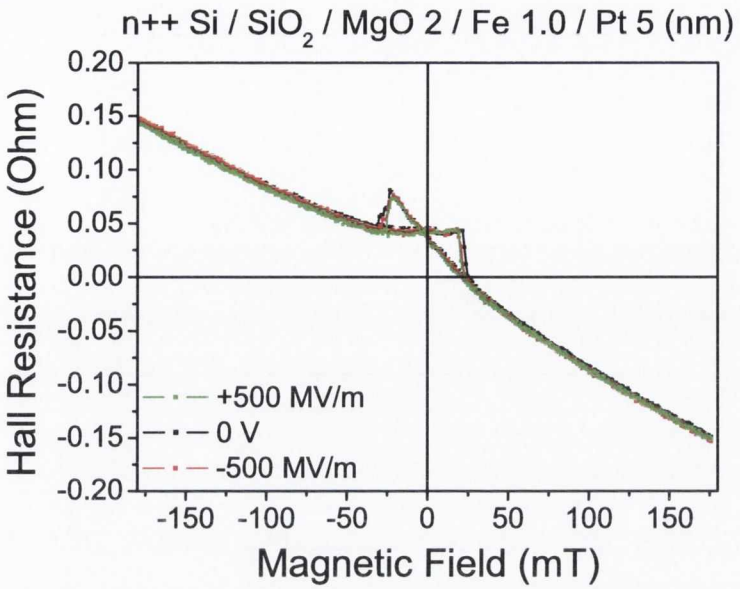

Figure 5.7: EHE curve responses for differing voltages applied to the MgO / Fe 1.0 nm / Pt system. The magnetic field is applied perpendicular to the film plane

for greater charge than the spin-on polyimide dielectric, which allows for a greater number of electrons per atom to be induced. However, the growth of metal on insulator is an issue; it has been shown that Fe on MgO grows in 3D island-like (Volmer-Weber) growth, with a percolation threshold of 1.0-2.0 nm [22]. The fact that the Fe is not a continuous layer might impact both the PMA, due to the lack of continuous interface with the MgO and Pt layers, and the electronic structure of the Fe. For electronic bands to form we assume a continuous layer in which we have a free electron gas and a 'sea' of ionic cores. Since the Fe grows as isolated islands, instead of having a thin continuous layer, we will have tall islands. The total volume of the deposited layer will be the same but if it is broken into islands the surface area to volume ratio is reduced. In Ref. [2] the effect was large because the Fe layer was two atoms thick and continuous, meaning that the interface area was very large. In the case of a continuous thin film it is possible to calculate the shape, magneto-elastic and magneto-crystalline anisotropies. A continuous layer has well defined volume and interface contributions to K_{eff}. In the case of a discontinuous layer precise dimensions of the islands are not known making calculations, even of shape anisotropy, difficult, as the demagnetising tensor N depends on the particle geometry (see section 3.1). In

our case only the atoms at the interface (and perhaps one layer beyond that) will be affected by the interfacial charging caused by applied the applied electric field. The atoms on the top of the island away from the insulating MgO will not see the electric field due to the screening effect from the interface atoms. There was no appearance of coercivity or change in the slope of the EHE curve. If the anisotropy is modified then we would see a change of the field required to saturate the Fe layer just as in Ref. [2]. Therefore we conclude that we do not see any significant change in anisotropy as a function of applied electric field in our MgO/Fe/Pt system.

Our results could be due to the lack of a good interface between MgO and Fe and the high surface area to volume ratio. The thickness in Ref. [2] was varied by means of a wedge during deposition, this provided a gradual change from 2 to 4 monatomic layer coverage over a 20 mm lateral distance. This provides a very precise way of altering the thickness, something the electric field effect (and PMA) has been shown to be sensitive to (see [2], [11], [3] and Chapter 3). Deposition in the Shamrock system is not so precise. Since the growth rate is low ($\sim$ 0.01 nm/s) and the minimum time require for uniform coverage if a 4" wafer is 15 seconds, we can control the thickness to at least 0.15 nm. Also due to the planetary motion, a wedge system cannot be implemented. Each sample must be grown independently and therefore thicknesses were increased in 0.2 nm steps. Any thickness variation below this is not experimentally controllable within Chamber A of the Shamrock.

We believe the lack of an electric effect is due to the island-like growth of Fe on MgO, rather than the inability to apply an electric field. Any charge applied to the highly doped Si will spread uniformly throughout the layer and the interface of the Fe islands on the MgO should be charged uniformly. We therefore chose to change the ferromagnetic material to one that has a better chance of forming a continuous layer on an insulating film. This is a consequence of the sputtering method. Better results might be obtained with e-beam evaporated Fe which is closer to the MBE growth used in [2].

5.4 MgO/CoFeB/Pt

Since the problem of surface wetting and the continuous nature of the Fe layer was an issue, we tried structures known to show PMA when grown on MgO. As-deposited $Co_{40}Fe_{40}B_{20}$ on MgO will be amorphous due to the high boron content [23] and also it can form continuous layers at smaller thicknesses than Fe. At 1 nm $Co_{40}Fe_{40}B_{20}$ forms a continuous layer on MgO. Nistor *et al.* showed it was possible to realise PMA in the MgO/CoFeB/Pt system by annealing [24]. This was attributed to the optimum oxidation of the MgO/CoFeB interface upon annealing, similar to the case of Pt/Co/AlO_x [25]. That is, the strong anisotropy is believed to originate from the MgO/CoFeB interface. This is similar to the Ref. [3] where the PMA of Ta/CoFeB/MgO was attributed to oxidation of Fe at the CoFeB/MgO interface. We deposited the following structure by sputtering:

n++ Si / SiO_2 / MgO / CoFeB 1.0 / Pt

The MgO was deposited by RF sputtering in Chamber B of the Shamrock sputtering tool. The $Co_{40}Fe_{40}B_{20}$ layer was deposited by DC sputtering also in Chamber B. The Pt cap layer was deposited in either Chamber A or Chamber B depending on the availability of the Pt target. In the as-deposited state there was no observable PMA. The constant slope is from the ordinary Hall effect and the symmetric peaks around zero of the EHE measurement for the as-deposited state are from the anisotropic magneto-resistance (AMR) [26]. The presence of AMR in the perpendicular measurement indicates in-plane magnetisation. The EHE curve is shown in Figure 5.8. High temperature annealing was performed in a vacuum furnace at 350 °C in an applied field of 800 mT for one hour. Upon annealing the sample exhibited a perpendicular easy axis (see Figure 5.8). Upon annealing at 350 °C we have sharp switching about zero with 100 % remenance, the coecivity is less than 1 mT, see Figure 5.8. We take H_c to be 0.4 mT from Figure 5.9.

XRD data for the as-deposited and annealed cases is presented in Figure 5.12. In the as-deposited state (black line) we can see Pt [111] at 39.8°and MgO [001] at 42°. Upon annealing at 350°C we notice that the Pt [111] peak is shifted to higher angle and the intensity is reduced.

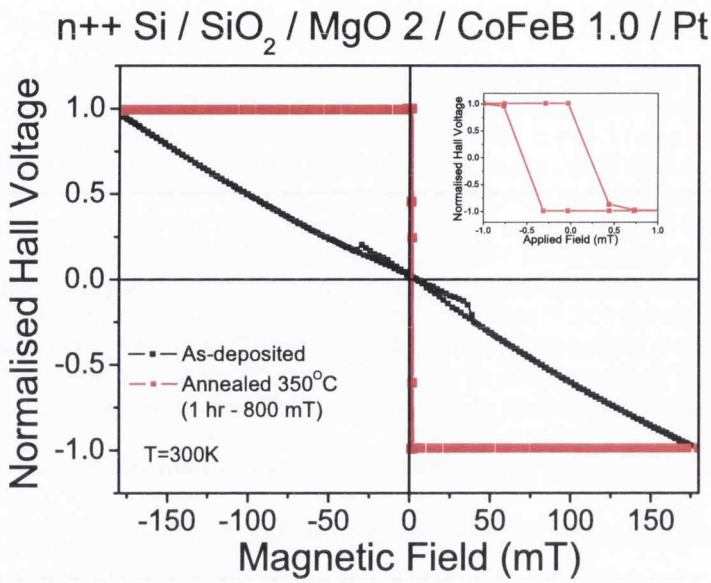

Figure 5.8: EHE curves for MgO/CoFeB/Pt in the as-deposited state and after annealing at 350°C. The inset shows the low field hysteresis loop in the annealed case. The magnetic field is applied perpendicular to the film plane

We attribute this to B diffusion into the Pt lattice which causes a change in the d-spacing of the Pt unit cell as the boron will substitute the Pt atoms. Also upon annealing the MgO [001] peak disappears, meaning that there is no improvement of the MgO texture upon annealing on SiO_2. We also can see a very weak CoFe [110] reflection after annealing, this indicates the crystallisation of CoFeB has occurred. It is possible that the CoFeB is not crystallising with a [110] texture but the [001] peak is not accessible as is it under the Si substrate peak. Offset ω-angle XRD scans were not performed. However, by adjusting ω it is possible to scan around the Si peak at 69.13°without seeing the intense substrate reflection. The presence of the CoFe[110] peak indicates only that the CoFeB has crystallised i.e. B has gone out of it. XRD is discussed in more detail later.

Pt can also help stabilise the PMA, however XRD shows that the Pt [111] intensity is reduced, suggesting that B diffuses into that layer. As CoFeB crystallises the B must get out: B does not diffuse into our barriers [15] and so diffuses into the Pt layer, the change in d-spacing indicated that the B has substituted a Pt in the lattice. The lack of a sharp interface implies that

the anisotropy from the CoFeB/Pt interface is weakened. This implies that the PMA is originating from the MgO/CoFeB interface and not from the Pt interface. Although a detailed study of the interfaces is not performed here, we conclude that in the annealed sample

1. MgO [001] texture is not improved
2. The CoFeB/Pt interface is diffuse
3. CoFeB crystallises with a weak [110] texture

It is not obvious if we have Fe[001] at the interface. However the PMA could be stabilised by oxygen bonds at the CoFeB/MgO interface [24] [25].

We applied electric fields from -500 MV/m to +500 MV/m across the SiO_2/MgO insulating layers in order to try to observe a change in coercivity. The sample was first measured at zero voltage several times ($\sim$ five repeats). Then the voltage was increased to +10 V and the measurement was taken again (five times). The polarity of the voltage was switched and the measurement repeated. The voltage was then increased and another five measurements were taken. This allowed for us to eliminate variations of the anisotropy over time (if any arose) and also to eliminate effects from sample heating. The results obtained with the electric field applied are shown in Figure 5.9.

We find that the EHE loops are modified but it is difficult to quantify the change as the stepping of the electromagnet in our system could not be reduced below 0.25 mT. The coercivity is taken to be 0.4 mT at zero applied electric field. The effect seen in Ref. [3] was a 0.3 mT change, modulated through similar electric fields. It would be better to use Helmholtz coils rather than an electromagnet [3].

The modification at positive electric fields (+500 MV/m) is to decrease the coercivity (K_{eff} $\downarrow$), whereas negative electric fields (-500 MV/m) seem to enhance the coercivity (K_{eff} $\uparrow$). This is consistent with Refs. [1] [2] and [3]. If we compare the literature between the studies of [24] and [3] where the stabilisation of PMA was realised with and without Pt respectively we might conclude that the nature of the interface with MgO in both systems is different. In fact, in the latter it was suggested that the anisotropy originates solely from the MgO/CoFeB interface and

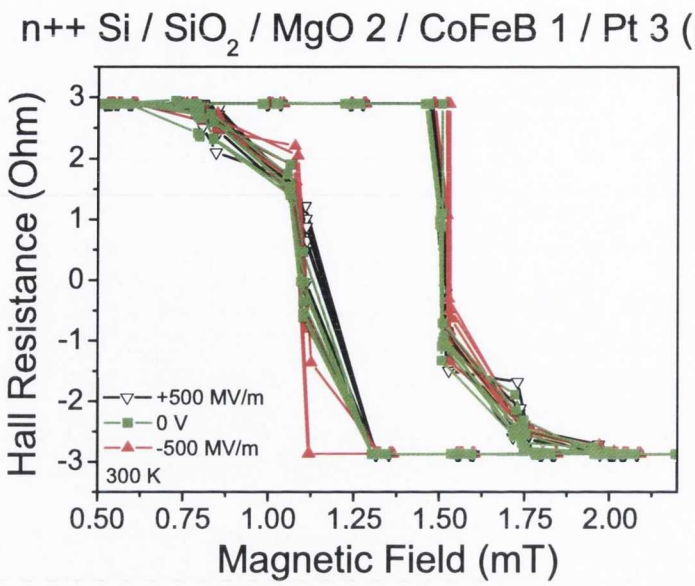

Figure 5.9: Hall resistance loops as function of applied electric field for MgO 2 / CoFeB 1 / Pt 5 annealed at 350°C. The magnetic field and electric field are both applied perpendicular to the film plane

is due to Fe-O bonds. Since the electric field effect is observable in both systems we conclude that the nature of the PMA is the same in both cases and that it originates solely from the MgO/CoFeB interface.

However to be sure the effect was real, since our experimental resolution was 0.25 mT (and the change reported in Ref. [3] was 0.3 mT), we cooled the sample to 12 K to investigate the effect of an electric field. We applied the same electric fields to the layer. The EHE curves at +500 MV/m and -500MV/m are shown in Figure 5.10. We repeated each measurement a number of times (as in the room temperature measurement) to average the result.

The variation of the coercivity with applied field is repeatable and reproducible, the change in coercivity between maximum and minimum applied electric field is 2 mT. This corresponds to a change of 2%. We find that the coercivity increased at negative electric fields and decreased at positive electric fields. The error stemming from the stepping of the magnetic field is seen clearly in Figure 5.10, where the resolution of the measurement is $\sim$0.5 mT. Nevertheless we can see that the coercivity switch for -500 MV/m is shifted significantly compared

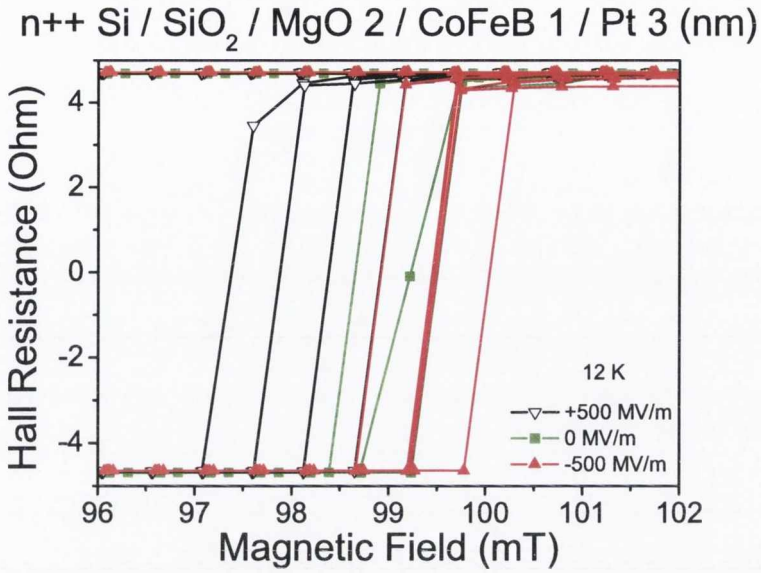

Figure 5.10: Magnetic switching as a function of applied electric field at low temperature (12 K) for MgO/CoFeB/Pt after annealing at 350°C. When the MgO/CoFeB interface is negatively charged the coercivity is decreased. When it is positively charged the coercivity is increased. The magnetic field is applied perpendicular to the film plane

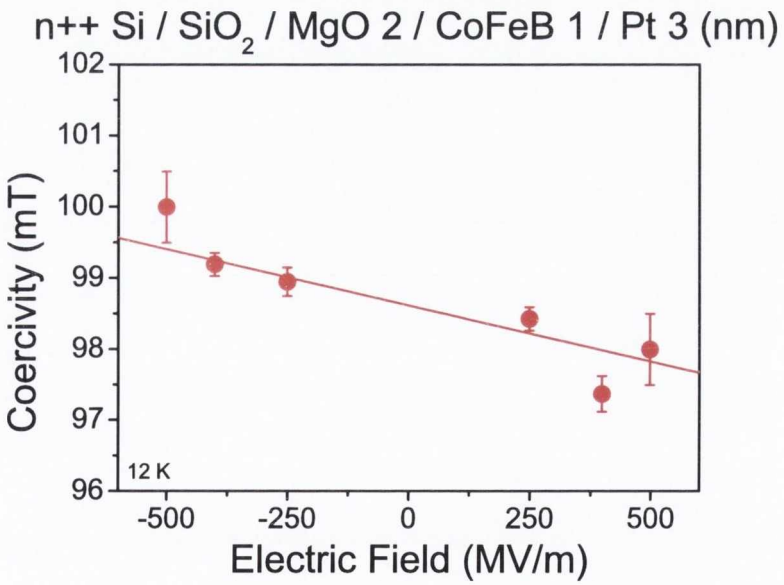

Figure 5.11: Electric field dependence of the coercivity of annealed MgO/CoFeB/Pt at 12 K.

to +500 MV/m. The change in coercivity as a function of applied electric field is shown in Figure 5.11. The slope of the curve is consistent with the results presented in [2] and [3]. We therefore attribute this change to the change in anisotropy of the CoFeB/MgO interface rather than the CoFeB/Pt interface. This CoFeB/Pt interface is not expected to provide any interfacial anisotropy in this case as B diffusion means the interface is less sharp. The CoFeB/Pt interface is not expected to be affected at all by the electric field due to the screening effect of the 1 nm thick CoFeB layer. Any PMA from the CoFeB/Pt interface should be magnetoelastic in origin and related to strain, electric field induced strain will be symmetric with applied field. The result is also in agreement with Ref. [1], where the authors see a decrease when the FePt electrode is negative (when the gate voltage is positive). As electrons are added from the CoFeB/MgO interface the perpendicular anisotropy is reduced. When electrons are removed then anisotropy is enhanced. This is also consistent with the calculations in [7], where the electric field at a Fe/vacuum interface was calculated. During the application of the applied electric field the leakage current was below 1 nA, taking the resistance of the multilayer stack to be in the kΩ range the power dissipated within the sample due to leakage is below 10^{-15} W.

If we compare the magnitude of the electric field modification seen at low temperature and room temperature we can see the percentage change is not comparable. At low temperature the effect is ~2%, if this were the same at room temperature the the change we should observe is 0.008 mT. Although the data at room temperature is not quantifiable, we can be sure that the change of coercivity is greater than 0.008 mT.

It is also necessary to compare both the MgO/CoFeB/Ta and MgO/CoFeB/Pt cases. Both undergo annealing in a perpendicular field at 350 °C for one hour. The crystal structure is different in both cases. The CoFeB and MgO in Ref. [3] possesses strong [001] texture, as shown by high tunnel magnetoresistance values when the layers were included in a magnetic tunnel junction [27]. The MgO/CoFeB/Pt electrode has not yet, however, produced such high values. This is due to the lack of [001] texture in these systems [28]. Given the similar electric field effects at the interface we can conclude that the strong [001] texture is not a necessity for observation of electric field modification of anisotropy.

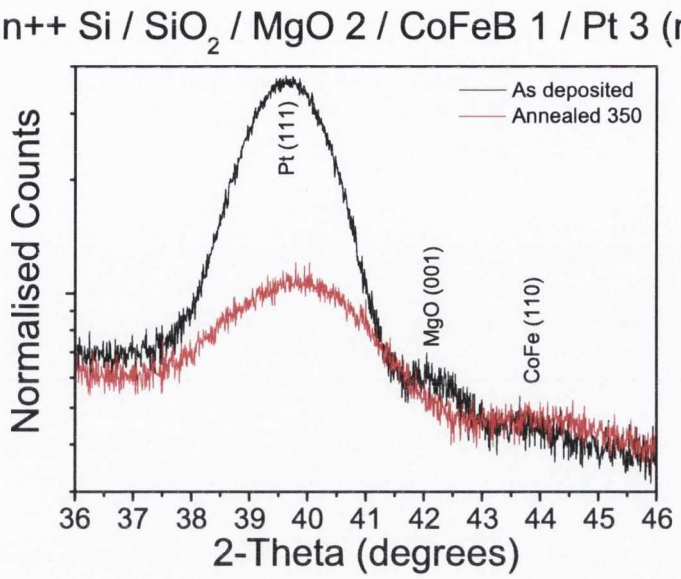

Figure 5.12: XRD data for MgO/CoFeB/Pt in the as-deposited state and after annealing at 350°C

The change in coercivity was 10% in Ref. [3], whereas in our case it is 2% at low temperature and not quantifiable at room temperature (though a 10% change would correspond to a change of 0.04 mT). If there was any alloying of the CoFeB/Pt interface we would expect to see the same response as in Ref. [1] (which we do indeed see). If the degree of O bonding at the interface is the key issue then the stabilisation of the PMA in this system would also give rise to the changes seen with electric field. We also present 2θ data on the as-deposited and annealed samples in Figure 5.12. The reason we think that the effect is stemming from the MgO interface are;

1. XRD data indicates that the Pt [111] texture is reduced, this would reduce any magnetoelastic strain, so upon annealing the PMA from the CoFeB/Pt interface is weakened.

2. The electric field should be screened within a few angstrom of the MgO/CoFeB interface and so cannot penetrate to the CoFeB/Pt interface.

Since the PMA from the CoFeB/Pt is magnetoelastic in origin we do not expect an electric field to change this, however FePt alloying would result in magneto-crystalline anisotropy which

could be affected by electric field, but the electric field still has to penetrate 1 nm into the CoFeB layer. This distance is too large given the calculated screening lengths from Ref. [5]. Therefore we argue that the electric field effect (and also the PMA) is originating solely from the CoFeB/MgO interface.

Oxidation at the CoFeB/MgO interface is believed to be the origin of the induced PMA in these systems [24] [3]. It is stressed that the system here is different to the other systems in the literature and there is no direct evidence of [001] Fe. The XRD measurements indicate that there is weak [110] CoFe texture present and that the CoFeB/Pt interface is rougher upon annealing, and that there is no improvement in [001] MgO texture. Despite the fact that the authors of both studies found high PMA in both systems a systematic study of the capping or buffer layer was not performed. Here we present data on Pt capping thickness while fixing the CoFeB thickness at 1 nm.

5.4.1 Pt thickness dependence of PMA in MgO/CoFeB/Pt layers

The following samples were grown

$$\text{Si / SiO}_2\text{ / MgO / CoFeB 1.0 / Pt } t$$

where t = 0, 0.5, 1, 2, 3 and 4 nm. The magnetisation switching was investigated by magneto-optical Kerr effect. We find that there is a dependence of the PMA on thickness and annealing temperature.

The samples were annealed at different temperatures from 50 to 400 °C in steps of 50 °C. The data set for samples annealed at 400 °C is shown in Figure 5.13.

From the figure we can see a clear dependence on the Pt cap thickness, due to the effect on the PMA on the capping layer thickness which we attribute to different B diffusion rates. Magnetic tunnel junctions have shown dependence on capping materials in terms of thickness [29]. They suggested the rise and fall in TMR in that system to the optimum oxidation of the CoFeB/MgO interface and the strain induced by the Ta/Ru cap as the annealing temperature was increased. In our system we attribute the rise of oxidation at the MgO/CoFeB interface and

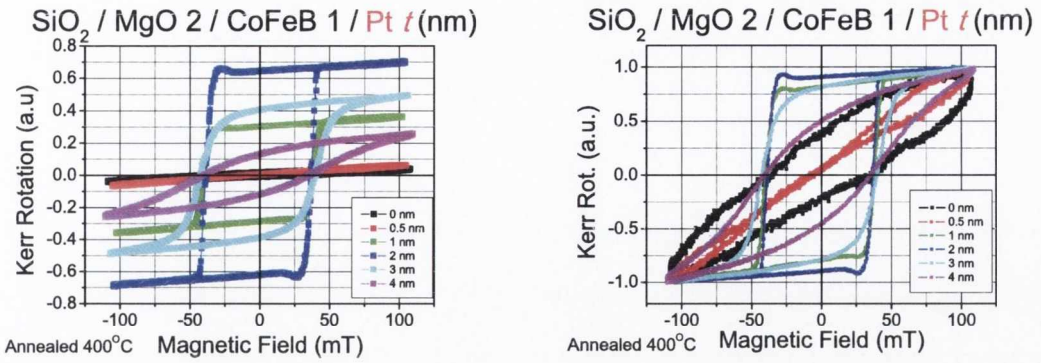

Figure 5.13: Relative and normalised MOKE loops for MgO 2 / $Co_{40}Fe_{40}B_{20}$ 1 / Pt t annealed at 400 °C

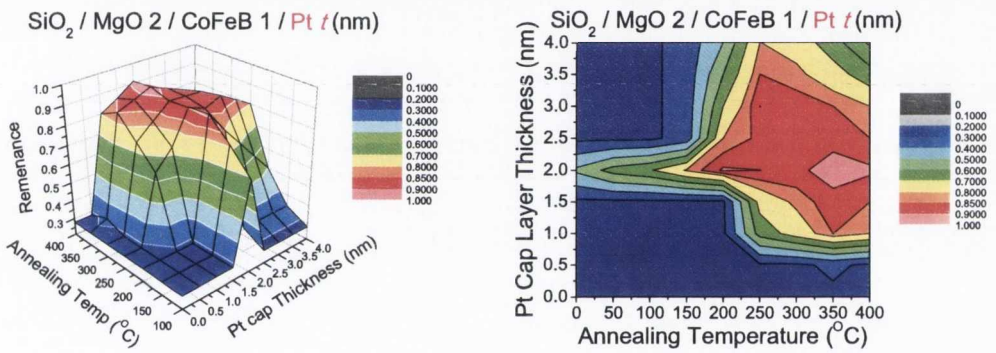

Figure 5.14: Pt capping layer thickness versus annealing temperature versus perpendicular remanence for MgO 2 / $Co_{40}Fe_{40}B_{20}$ 1 / Pt t

the fall of strain induced by the CoFeB/Pt interface due to B diffusion into Pt. The high PMA from this system is due to the interface of MgO and CoFeB [30]. If the PMA is indeed due to the oxidation of the CoFeB/MgO interface and the movement of B away from MgO, then the capping layer and its thickness should affect the magnetic anisotropy.

A full plot of the Pt capping thickness versus annealing temperature versus perpendicular remanence (normalised between 0 and 1) is shown in Figure 5.14.

As is clearly visible from the contour plot, a 2 nm Pt cap layer allows for the stabilisation of anisotropy at a range of temperatures 250 - 400 °C. We relate this to the B diffusion in the

system and the stress that the Pt layer can induce on the crystallised CoFe and the MgO layer.

The high temperature annealing allows B to diffuse out of the layer and for the bonding of Fe and O orbitals at the MgO interface to stabilise the PMA.

We therefore attribute the effect of the electric field to the change of the electronic density at the surface of the CoFeB layer at the MgO/CoFeB interface.

5.5 MgO/CoFeB/Pd

In Chapter 4 we investigated the perpendicular anisotropy in CoFeB/Pd bilayers for the purposes of investigating the electric field control of anisotropy in the MgO/CoFeB/Pd system. We obtained an interfacial anisotropy of 320 $\mu J/m^2$. The following structure

$$n++ \text{ Si / } SiO_2 \text{ / MgO / CoFeB 0.6 / Pd}$$

exhibits a perpendicular easy axis at room temperature in the as-deposited state. The room temperature EHE response of a 2 μm Hall bar is shown in Figure 5.15. The response is that of, what appears to be a superparamagnetic and discontinuous layer with no coercivity or hysteresis. In this sample we applied up to voltages from -100 V (-500 MV/m) to +100 V (+500 MV/m) and observed no change in the anisotropy of the device at room temperature. A change in anisotropy would manifest itself as a change in slope of the EHE response.

As the sample exhibited hysteresis below the blocking temperature (see section 4.6) we cooled the sample down to 12 K and performed the experiment again. The sample geometry in this case is a 3×3 mm^2 area not a 2μm Hall bar. This method was used due to lack of ion milling capabilities at the time of growth. Low temperature data taken at 12 K (the base temperature of the cryostat on the R-T rig) is shown in Figure 5.16. The coercivity is considerably increased ($\sim$ 140 mT) upon cooling as we are now below the blocking temperature T_B. Here the anisotropy-volume product, $K_{eff}.V$, is now greater than the thermal energy $k_b.T$, where T is the measurement temperature, and the sample now exhibits hysteresis.

We find that the coercivity is decreased at negative voltages and increased at positive voltages. Under negative voltage the CoFeB interface with MgO is positively charged and under

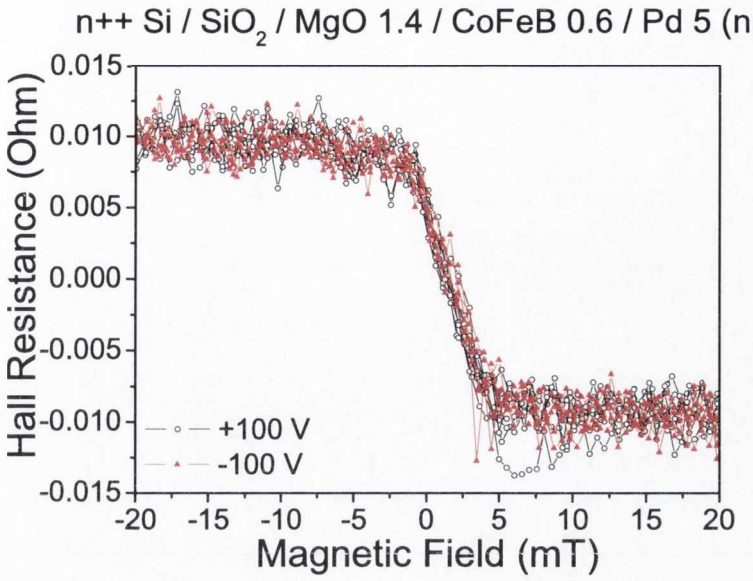

Figure 5.15: Room temperature EHE response of as-deposited MgO/CoFeB/Pd

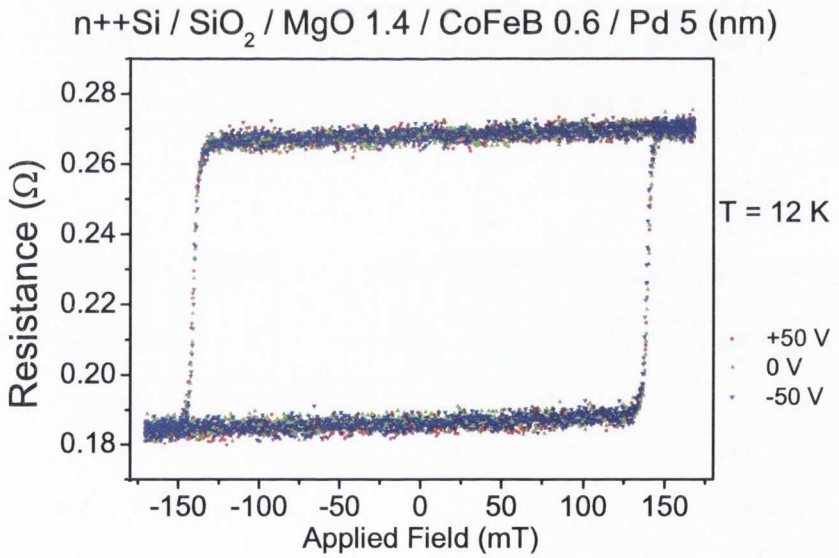

Figure 5.16: EHE loops as at different applied voltages in the as-deposited MgO/CoFeB/Pd system at 12 K

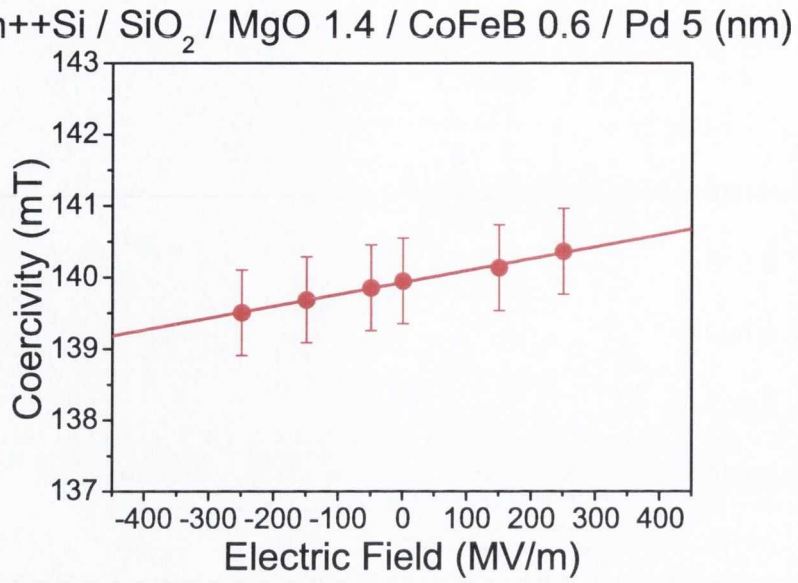

Figure 5.17: Coercivity as a function of applied electric field in the as-deposited MgO/CoFeB/Pd system at 12 K

positive voltage the interface is negatively charged. This is opposite to the case of the annealed MgO/CoFeB/Pt (as discussed in the previous section). A plot of coercivity with applied electric field is graphed in Figure 5.17. Although the change is not as dramatic as that shown in Figure 5.9, there is a change of the coercivity as a function of applied electric field. The change is very slight, so in order to determine if the effect was in fact real and not an artefact of the measurement setup the measurements were repeated with freshly grown samples. The samples show a variation in the low temperature coercivity and blocking temperatures but a perpendicular easy axis is still observed at room temperature and at low temperatures. All repeated samples exhibited superparamagnetic behaviour at room temperature and showed hysteresis upon cooling to 12 K in the cryostat. Two, nominally identical, sample repeats are shown in Figure 5.18. The variation in coercivity could be due to the island like growth of CoFeB on MgO, and slightly different deposition rates. Changes in blocking temperature and coercivity at low temperature suggests that the superparamagnetic volume in each case is different, as the blocking temperature is related to the anisotropy volume product $K_{eff}.V$. The following trend is observed within the sample set, when the coercivity is low the associated electric field response is also low.

Despite the differences in the coercivity, we find that an electric field appears to modify the anisotropy in the same fashion as in the first sample i.e. at positive electric fields (where the CoFeB/MgO interface is charged with excess electrons) the PMA is enhanced. Again, this system is not an ordered alloy but since we have Fe and Pd in contact at the interface of CoFeB/Pd and the response is similar to Ref. [1], we can speculate that the perpendicular anisotropy is originating at the CoFeB/Pd interface. If the PMA was due to the MgO/CoFeB interface we would expect the response of both systems would be the same i.e. adding electrons to the CoFeB layer decreases the PMA.

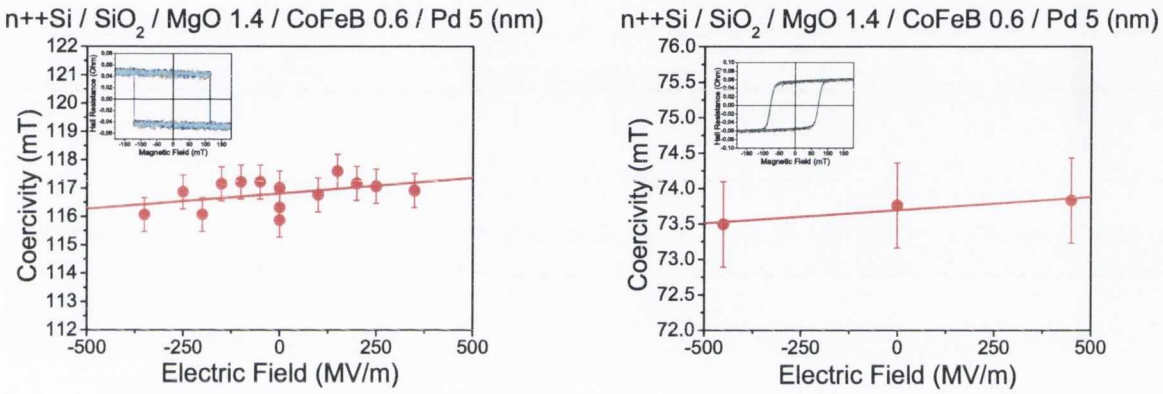

Figure 5.18: Low temperature EHE and electric field effect responses of nominally identical MgO/CoFeB/Pd Hall bars. Insets show the full EHE loops of both samples. The different sign of the EHE response is due to the sample mounting in the cryostat, samples are mounted back to back so the field is in the opposite direction in the graph on the left, hence the opposite EHE response.

It is surprising that there is not a bigger effect when H_c is low. The perpendicular anisotropy, K_{eff}, is close to zero. In this case a small change in induced anisotropy might cause switching of the easy axis to in-plane.

In this unannealed system, the only Fe-O or Co-O that could form would be due to dangling O bonds on the MgO surface during growth. Elevated temperatures during growth could also cause some annealing during deposition. Since the first sample was patterned by lift-off there was no annealing. The repeated samples (shown in Figure 5.18) were patterned into 2 μm Hall bars by a combination of UV lithography and ion milling. During processing, these samples

were annealed at 120 °C in order to cure the photoresist. This heating could also be responsible for the lower coercivity seen in the samples.

It is not completely clear if the electric field only modifies the MgO interface or if it is possible for the field to penetrate 0.6 nm of CoFeB and affect the bandfilling near the CoFeB/Pd interface. The screening length calculated by Zhang [5] is of the order of 1-2 Å for Fe and Co. It might therefore be possible to affect the CoFeB/Pd interface in this ultra-thin layer. If the PMA is due to oxygen bonds as in the MgO/CoFeB/Pt then the effect should be exactly the same. The fact that the electric field induced response is opposite suggests that, in this system, the effect is not related to the nature of the MgO interface.

5.6 Conclusions

We investigated the electric field effect [1] on magnetic thin film layers possessing perpendicular anisotropy. For the case of MgO/Fe/Pt we were unable to realise the perpendicular anisotropy, or use an electric field to modify the in-plane anisotropy. For the case of MgO/CoFeB/Pt (annealed at 350°C) we did observe a change of the coercivity as a function of applied electric field at room temperature and low temperature. The coercivity (and hence magnetic anisotropy) was increased when the MgO/CoFeB is depleted of electrons, consistent with results from [2] and [3]. We find no evidence for [001] texture at the MgO/CoFeB interface which suggests that the electric field induced change in anisotropy does not require [001] textured Fe.

For the case of MgO/CoFeB/Pd we observed no coercivity at room temperature, where the film appears to be superparamagnetic. We did observe coercivity below the blocking temperature (220 K). We also observed a change in the magnetic anisotropy at low temperatures. The coercivity was decreased when the MgO/CoFeB interface depleted, whereas it was increased when interface was charged. The differing sign of CoFeB/Pt and CoFeB/Pd correspond to the trend seen in Ref. [1] in relation to $L1_0$ ordered FePt and FePd. It is clear that we do not have the $L1_0$ structure in our case, however we may have a structure similar to that just at the interface of CoFeB with either Pt or Pd. It is necessary to first determine the origin of the PMA in

both cases and then the effect of an electric field can be quantified. We have demonstrated that Fe [001] is not necessary for the modification of the PMA (i.e. the MgO/CoFeB/Pt system) and also that it appears the effect can be seen in the as-deposited state (i.e. the MgO/CoFeB/Pd).

For the case of MgO/CoFeB/Pt it would be prudent to compare differing Co/Fe ratios to see if the effect is enhanced with higher Fe content. The effect of electric field modulation of induced anisotropy from [3] and [27] has not been systematically studied yet. The perpendicular anisotropy in MgO/CoFeB/Pt exists after annealing due to oxidation at the MgO interface. The response of the PMA to an electric field as a function of annealing temperature would generate interesting data. Combined with the result in section 5.4.1 the investigation of the entire sample set, annealing temperature and Pt thickness, would provide the first systematic study of the effect of an electric field on the anisotropy in the CoFeB system.

Since we find no evidence for high quality interfaces (from XRD data) it would appear that only an insulating interface is required. In the case of MgO/CoFeB/Pt, the PMA appears as a result of this interface, it is therefore easy to attribute the interfacial charging to the measured change in coercivity. For MgO/CoFeB/Pd on the other hand, the origin of the anisotropy is not clear. It could be possible that it is solely due to the CoFeB/Pd interface. If this is the case, the change in coercivity due to interface charging is not readily explained. If the anisotropy was again due to the MgO/CoFeB interface we would expect the same response from either system regardless of the capping material.

The origin of the PMA, and therefore the change in anisotropy induced by surface charging is not clear in the MgO/CoFeB system. What is clear though, is the fact that the effect is extremely small. It seems then, that the effect (at least in these systems) is not technologically exploitable for storage of magnetic data.

Other systems where PMA has been stabilised include SiO_2/Co/Pt (annealed at 400°C) [24]. This system contains no Fe: experimental verification of a lack of electric field induced change of anisotropy would validate the calculations of Nakamura *et al.* [7]. On the other hand, an effect in this system would require further thought for calculations.

What is required for the use of this effect in real storage device is a large response of the

anisotropy to an applied electric field (much larger than that presented here). Storage devices require high anisotropy for thermal stability, and so to be useful the anisotropy must be significantly lowered upon electric field application during the writing process. Since switching of magnetisation seems not to be possible solely with electric fields, the effect must be large to reduce the anisotropy so switching can be performed by some other "low-power" means.

Bibliography

[1] Weisheit, Martin and Faehler, Sebastian and Marty, Alain and Souche, Yves and Poinsignon, Christiane and Givord, Dominique. *Science* **315**(5810), 349–351 JAN 19 (2007).

[2] Maruyama, T. and Shiota, Y. and Nozaki, T. and Ohta, K. and Toda, N. and Mizuguchi, M. and Tulapurkar, A. A. and Shinjo, T. and Shiraishi, M. and Mizukami, S. and Ando, Y. and Suzuki, Y. *Nature Nanotechnology* **4**(3), 158–161 (2009).

[3] Endo, M. and Kanai, S. and Ikeda, S. and Matsukura, F. and Ohno, H. *Applied Physics Letters* **96**(21) MAY 24 (2010).

[4] Daalderop, G.H.O., Kelly, P.J., Schuurmans, M.F.H. *Physical Review B* **44**(21), 12054–12057 (1991).

[5] Zhang, S. *Physical Review Letters* **83**(3), 640–643 (1999).

[6] Niranjan, M.K., Duan, C.-G., Jaswal, S.S., Tsymbal, E.Y. *Applied Physics Letters* **96**(22), 222504 (2010).

[7] Nakamura, Kohji and Shimabukuro, Riki and Fujiwara, Yuji and Akiyama, Toru and Ito, Tomonori and Freeman, A. J. *Physical Review Letters* **102**(18) MAY 8 (2009).

[8] Shimabukuro, R., Nakamura, K., Akiyama, T., Ito, T. *Physica E: Low-Dimensional Systems and Nanostructures* **42**(4), 1014–1017 (2010).

[9] Zhang, H., Richter, M., Koepernik, K., Opahle, I., Tasnadi, F., Eschrig, H. *New Journal of Physics* **11**, 043007 (2009).

[10] Sahoo, S., Polisetty, S., Duan, C.-G., Jaswal, S.S., Tsymbal, E.Y., Binek, C. *Physical Review B - Condensed Matter and Materials Physics* **76**(9), 092108 (2007).

[11] Shiota, Yoichi and Maruyama, Takuto and Nozaki, Takayuki and Shinjo, Teruya and Shiraishi, Masashi and Suzuki, Yoshishige. *Applied Physics Express* **2**(6) JUN (2009).

[12] Ha, Seung-Seok and Kim, Nam-Hee and Lee, Sukmock and You, Chun-Yeol and Shiota, Yoichi and Maruyama, Takuto and Nozaki, Takayuki and Suzuki, Yoshishige. *APPLIED PHYSICS LETTERS* **96**(14) APR 5 (2010).

[13] Fowley, Ciaran and Decorde, Nicolas and Oguz, Kaan and Rode, Karsten and Kurt, Huseyin and Coey, J. M. D. *IEEE Transactions on Magnetics* **46**(6), 2116–2118 JUN (2010).

[14] Ohno, H., Chiba, D., Matsukura, F., Omiya, T., Abe, E., Dietl, T., Ohno, Y., Ohtani, K. *Nature* **408**(6815), 944–946 (2000).

[15] Kurt, H., Rode, K., Oguz, K., Boese, M., Faulkner, C.C., Coey, J.M.D. *Applied Physics Letters* **96**(26), 262501 (2010).

[16] Zhou, T., Leong, S.H., Yuan, Z.M., Hu, S.B., Ong, C.L., Liu, B. *Applied Physics Letters* **96**(1), 012506 (2010).

[17] Gamble, S.J., Burkhardt, M.H., Kashuba, A., Allenspach, R., Parkin, S.S.P., Siegmann, H.C., Stohr, J. *Physical Review Letters* **102**(21), 217201 (2009).

[18] Stohr, J., Siegmann, H.C., Kashuba, A., Gamble, S.J. *Applied Physics Letters* **94**(7), 072504 (2009).

[19] Chiba, D., Nakatani, Y., Matsukura, F., Ohno, H. *Applied Physics Letters* **96**(19), 192506 (2010).

[20] Sangiao, S., M. L. S. G. D. T. J. P. J. A. J. I. M. *Physical Review B - Condensed Matter and Materials Physics* **79**(1) (2009).

[21] Volkov, V.T., L. V. M. V. B. V. *Applied Physics Letters* **91**(26) (2007).

[22] Arita, M., Wakasugi, K., Ohta, K., Hamada, K., Takahashi, Y., Choi, J.-B. *Microelectronic Engineering* **85**(12), 2445–2450 (2008).

[23] Heiman, N., Hempstead, R.D., Kazama, N. *Journal of Applied Physics* **49**(11), 5663–5667 (1978).

[24] Nistor, L.E., Rodmacq, B., Auffret, S., Dieny, B. *Applied Physics Letters* **94**(1), 012512 (2009).

[25] Rodmacq, B., Manchon, A., Ducruet, C., Auffret, S., Dieny, B. *Physical Review B - Condensed Matter and Materials Physics* **79**(2), 024423 (2009).

[26] Lindemuth, J., Dodrill, B. *IEEE Transactions on Magnetics* **40**(4 II), 2191–2193 (2004).

[27] Ikeda, S., Miura, K., Yamamoto, H., Mizunuma, K., Gan, H.D., Endo, M., Kanai, S., Hayakawa, J., Matsukura, F., Ohno, H. *Nature Materials* (2010).

[28] Tadisina, Z.R., Natarajarathinam, A., Gupta, S. *Journal of Vacuum Science and Technology A: Vacuum, Surfaces and Films* **28**(4), 973–978 (2010).

[29] Pong, P.W.T., Egelhoff, W.F. *Journal of Applied Physics* **105**(7) (2009).

[30] Nistor, L.E., Rodmacq, B., Ducruet, C., Portemont, C., Prejbeanu, I.L., Dieny, B. *IEEE Transactions on Magnetics* **46**(6), 1412–1415 (2010).

Chapter 6

Local He^+-Ion Irradiation of Co/Pt Multilayers

"sure that pipe was leaking before we took it down"

- a suit from ARDMAC

6.1 Introduction

Currently magnetic information storage exploits media exhibiting perpendicular magnetic anisotropy, especially CoCrPt (see section 1.2). Perpendicular magnetic anisotopy (PMA) arises either through magneto-crystalline anisotropy or interfacial magneto-elastic strain (discussed in section 3.1). The CoCrPt medium is granular, with a distribution in grain size and has no long range order that possesses high magneto-crystalline anisotropy. A new technology known as bit patterned media (section 1.3), which aims to drive magnetic storage past 1 Tb/in^2, requires a long range ordered substrate with almost identical magnetic islands.

Such long range order (say 150 nm islands with 150 nm spacing over a 3.5" platter) is difficult to achieve with a granular medium. Direct patterning or self-assembly of patterns for the fabrication of these individual islands is necessary. These individual islands can be obtained by physical (topological) or magnetic (non-topological) patterning. A bit patterned substrate

could be composed of ferromagnetic islands in a non-magnetic matrix. This can be achieved using local magnetic patterning of a planar substrate with uniform perpendicular anisotropy, for example a Co/Pt multilayer film [1].

Perpendicular magnetic anisotropy in Co/Pt and Co/Pd multilayers is especially sensitive to layer thickness and interface quality (see [2] [3] and Chapter 4). The strong anisotropy in these systems is due to the broken symmetry associated with the interface and the magneto-elastic stress caused by lattice mismatching at the Co/NM interface (see Chapter 3 and [4]). Thus the PMA in these specific multilayers is heavily dependant on interface abruptness (section 3.1.3 and Figure 3.4).

If we can modify the interfaces in the Co/Pt system suitably then we can gain control over the PMA. For this we use an energetic beam of ions to cause atomic displacements [1]. As the ion irradiation dose is increased the atomic displacements which result from scattering in the multilayer film can relieve stress at the interface. When the interface is modified we can imagine two situations caused by atomic displacements: we can form ordered alloys from multilayer structures (increase K_{eff}) [5], or we can simply allow relaxation of the interfacial strain (decreasing K_{eff}) [1]. Since the PMA in multilayers is heavily dependent on interface properties any small (atomic length scale) displacement of atoms can lead to a dramatic change in the magnetic properties [6].

For simplicity we imagine a single Co/Pt layer where the Co layer is approximately one atom thick and continuous, see Figure 6.1 (a). Since the Co layer is continuous the interfacial strain should be high, due to the lattice mismatch between Co and Pt. When we subject this stack to an energetic ion beam we can cause displacements of both Co and Pt atoms. Bulk Pt displacements should not affect the interfacial anisotropy, however movement of the Co or Pt atoms at the Co/Pt interface will. Any ion beam induced movement of a Co atom, even an atomic distance, will cause lowering of the strain induced anisotropy (b). At a sufficient irradiation dose the interfaces will be modified so that the magneto-elastic contribution to the effective anisotropy will be substantially decreased (c). At this point we will have in-plane magnetic anisotropy.

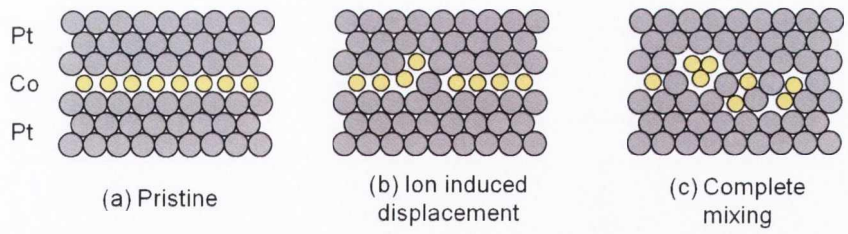

Figure 6.1: Graphical representation of ion beam induced intermixing of a single Co layer in a Pt/Co/Pt sandwich.

Traditional focused ion beam patterning is achieved with Ga^+, and it has successfully been used to modify the magnetic properties of thin films and devices [7] [8]. Focused Ga^+ ions and beam control software has recently been used to fabricate a micron sized magnetic tunnel junction (MTJ) *in-situ* [9].

An energetic beam passing through a material (such as a magnetic thin film) will have an associated interaction volume. The interaction volume is different for different beam energies and depends on the mass of the ion in the beam. Ga^+ has a large interaction volume in materials (see Figure 6.2), and introduces magnetically dead areas often of the order of 100 nm [9]. This is related to the lateral straggle of incident the Ga^+ beam. In Figure 6.2 we compare the interaction volumes of 30 keV Ga^+ and He^+ beams incident on a Co/Pt multilayer with a thick Pt cap layer at a dose of 10^{15} ions/cm^2 [1]. This dose corresponds to 160 ions impacting on the sample surface. The sample stack in the simulation is shown on the right of Figure 6.2. The ion beam trajectories are shown as red lines in the figure. For the case of He^+ most of the ions will pass through the full stack and end up in the SiO_2. For the Ga^+ beam we can see that most ions stop in the top Pt capping layer. The colour legend (green/purple/light blue and dark blue) represents the displacements of atoms in the multilayer upon impact with an incident ion from the beam. In the case of the capping Pt layer the difference between He^+ and Ga^+ is clear. For the case of Ga^+ the interaction and displacement of both Pt and Co atoms is major and the lateral straggle of the beam is over 2 nm. For the He^+ beam the displacement of atoms is substantially less and the beam profile is more uniform within the sample, the lateral straggle is less than 1

[1] This simulation was conducted using freely available software (described in section 6.6).

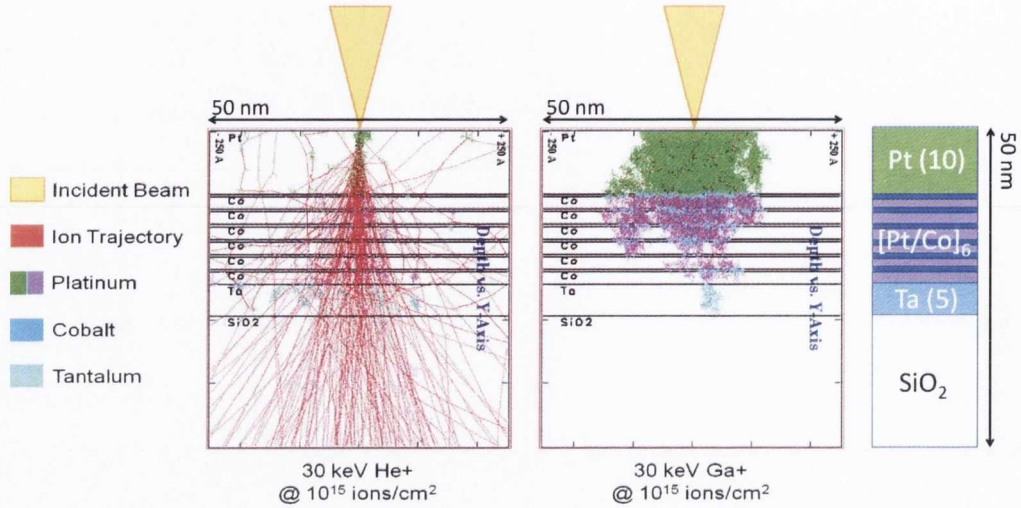

Figure 6.2: SRIM simulation of the interaction volume of 30 keV Ga^+ and 30 keV He^+ ions. The area represented is 50 by 50 nm^2. Red lines are incident ion trajectories. Colours are used to represent atomic displacements of atoms from their original locations. A graphical representation of the simulated stack is shown on the right. The full stack is $Si/SiO_2/Ta$ (5)/[Pt (2)/Co (0.4)]$_6$/Pt (10), the thicknesses in parentheses are in nm

nm.

It is noticed that although the beam profile is better for the case of He^+, we have some interactions far from the beam almost 2 nm away from the beam center. These interactions can also cause interface modification at that point and can affect the magnetic properties over a larger area. What is clear from Figure 6.2 is that a 30 keV He^+ beam can have a more subtle effect on the interfaces when compared to the Ga^+ beam.

The incident ion energy also has an impact on the interaction volume. A calculation of the interaction of differing energies is shown in Figure 6.3. In this simulation the interaction volumes for 10, 30 and 50 keV He^+ ions are shown. Irradiation is simulated on the same typical Co/Pt multilayer stack. What should be noticed is that at higher incident energies the interaction volume in the magnetic layers is smaller and incident ions tend to penetrate to the substrate. For the case of a 10 keV ion the interaction volume is mainly confined to the multilayer, therefore irradiations at this energy would result in a lot of beam induced modification of the interfaces over a larger lateral area. We see that a He^+ ion beam will have a smaller interaction cross-section at higher energies and that most of the incident ions penetrate to the underlying substrate.

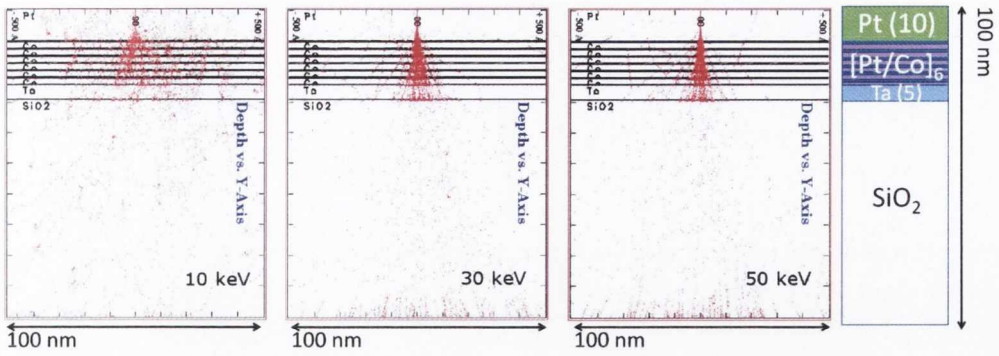

Figure 6.3: SRIM simulation of range and beam profiles of He^+ ions of differing energies with a typical Co/Pt multilayer for a dose of 1×10^{15} ions/cm^2. The simulated area is 100 by 100 nm^2. A graphical representation of the simulated stack is shown in the right. The simulation is described in the text.

Irradiation with He^+ ions has been shown to modify the magnetic properties of thin films with PMA [1] [10] [11] [12]. However all irradiations to tailor magnetic properties (to date) have been performed using a *broad beam* of He^+ ions. In [13] sub-50 nm structures were patterned by *broad beam* He^+ irradiation through a PMMA photoresist mask. The mask allowed selective exposure of certain regions, allowing relaxation of the lattice in those regions and a local reduction in the magnetic anisotropy. However, He^+ ions impacting on the side walls of the mask lose energy, so their interaction with the magnetic layers is different (as in Figure 6.3). In their experiment, collateral damage is evidenced by the nucleation of domains at the border of the shadow mask. The use of a physical mask can therefore be associated with a resolution limit to current He^+ lithography.

It was also shown that the combination of He^+ ion irradiation and a wedge shaped hard mask can be used to create a strip where the domain wall propagation field increases as a function of distance, thereby allowing the domain wall to be controllably moved (one way) along the strip [11]. By using a wedge the interaction between the beam and the multilayer was modified along the length of the wedge, and in this way the exposure dose of the underlying multilayer becomes a function of distance. The subsequent *broad beam* He^+ irradiation created a coercivity gradient along length of the strip. In order to move a domain wall along the wire the applied field must be continually increased.

In order to avoid the limit associated with using shadow masks and wedges we use the focused He^+ ion beam in a helium ion microscope (see section 2.3.2) to tailor, locally and masklessly, the magnetic properties in thin film Co/Pt multilayers with PMA. The effects of low energy ion induced damage can be minimised, because we now neglect any energy loss in the shadow mask. Ions incident on the sample will all have the same energy. We will have energy loss within the Pt cap layer but through careful choice of the capping thickness or material, it might possible to avoid the detrimental effects of lateral straggle altogether.

In this chapter we will demonstrate that a *focused* beam can be used to tailor the magnetic properties locally in magnetic films i.e. direct maskless magnetic lithography. This focused beam allows local tailoring of the magnetic properties within pre-patterned structures, specifically within Hall bar structures. The He^+ beam can also be used to mill areas of the Hall bar and, due to smaller interaction volume, should allow for much smaller features to be defined than with a traditional focused Ga^+ beam. By controlling the interface with high accuracy we can modify the PMA in thin film multilayers and exploit the magnetic patterning of planar multilayers for isolating independent magnetic islands in a paramagnetic matrix. Combining the effects of both focused ion milling and local modification of magnetic properties using He^+ ions, new opportunities for processing materials become accessible.

6.2 Experimental Methods

The effect of 30 keV He^+ ion irradiation on the magnetic properties of Co/Pt multiayers possessing PMA was investigated using the extraordinary Hall effect as a a detection mechanism. Perpendicular magnetic anisotropy was discussed in Chapter 3. The extraordinary Hall effect was described in section 2.4.3.

The multilayers were deposited by sputtering in Chamber A of the Shamrock sputtering system (see section 2.2.2) onto 25.4×25.4 mm^2 silicon substrates with 500 nm thermal oxide. Ar^+ ions were used to sputter Ta, Co and Pt layers at a power of 100 W. The deposition rates for Ta, Co and Pt were 0.007 nm/s 0.01 nm/s and 0.018 nm/s respectively. The deposition rates

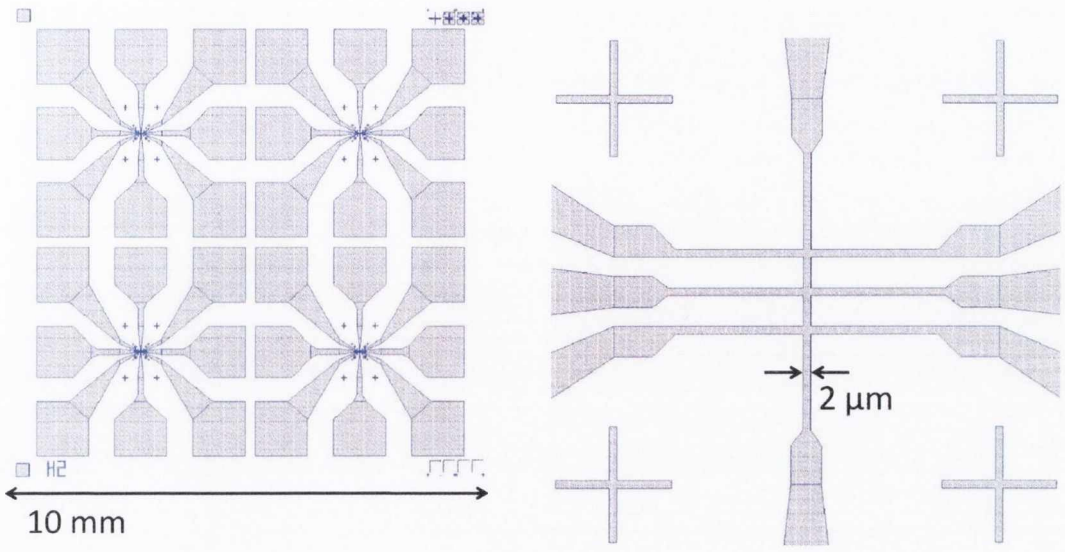

Figure 6.4: UV mask design for 2μm Hall bars. The chips are 4×4 mm^2 and there are four identical chips contained within 10×10 mm^2

.

were determined by XRR, as described in section 2.4.1. The deposition pressure was 1 mTorr with an Ar flow of 25 sccm. Turntable rotation was 44 rpm. The sample structure was as follows

$$Si / SiO_2\ 500 / Ta\ 5 / [Pt\ 2 / Co\ t]_6 / Pt\ 2 / Pt\ 8$$

Co thickness was t = 0.4, 0.5 and 0.6 (all thicknesses are in nm). The second Pt layer (8 nm) was deposited subsequently because of surface milling (see section 6.7).

After deposition the samples were patterned via UV lithography (as described in section 2.3.1). There are four devices contained within 10 by 10 mm^2, each with three Hall junctions nominally 2×2 μm^2 in size. The process parameters for exposure were as follows: Shipley S1813 photoresist was spun on the sample chip at 5000 rpm for 45 seconds using a programmable spinner; the resist was postbaked for 1 minute at 115 °C on a hotplate; the mask aligner was set up for near UV exposure (NUV - 365 nm); the intensity of the UV lamp was measured before exposure using a handheld intensity meter; the intensity was typically between 14 and 18 mW/cm^2. A 100 mm photomask with a Hall bar pattern (shown in Figure 6.4) was used to define the 2 μm Hall bars used for exposures. The sample was exposed using this mask

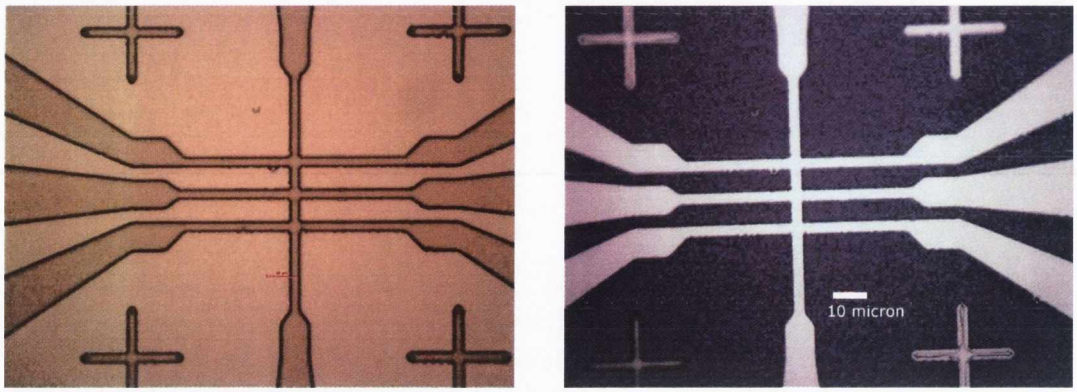

Figure 6.5: Optical microscope images of Hall bars before (left) and after (right) ion beam milling. On the left the pattern in the photoresist is visible above the planar Co/Pt multilayer stack (described in the text). On the right is the same stack, after ion milling and stripping of the photoresist

and the "quadrant" mask holder. The sample was loaded onto the chuck table and secured with the chuck vacuum. Hall crosses of interest were aligned over the center of the wafer by moving the sample stage under the mask. The sample was exposed in vacuum contact mode, which offers the highest resolution. Exposure time was programmed to be 3.5 seconds. This gives a dose of $\sim$ 50 mJ/cm^2. Finally the sample was exposed and then unloaded automatically. The exposed sample was placed in fresh Microposit MF-319 developer for $\sim$ 45 seconds (until the pattern became obvious on the substrate) and then rinsed in DI water for at least 45 seconds. Samples were then examined in an optical microscope in the class 1000 area of the CRANN cleanroom to ensure that good pattern transfer in the lithography process had been achieved. A typical image of an exposed Hall bar (before milling) is shown on the left of Figure 6.5.

After patterning the samples were ion milled in the Millatron (see section 2.3.1 and Appendix A). The milling angle was 45° and the argon partial pressure was 5×10^{-5} Torr. The RF power supplied to the ion gun was 400 W. Etching was monitored visually and stopped when the SiO_2 substrate was visible, SIMS was not used. After etching was finished the photoresist was removed using acetone (until the photoresist was dissolved) followed by an IPA wash and blow dry with nitrogen gas. The samples were then inspected again using the optical microscope to ensure that the resist was completely removed. An optical image of a finished 2 μm device is

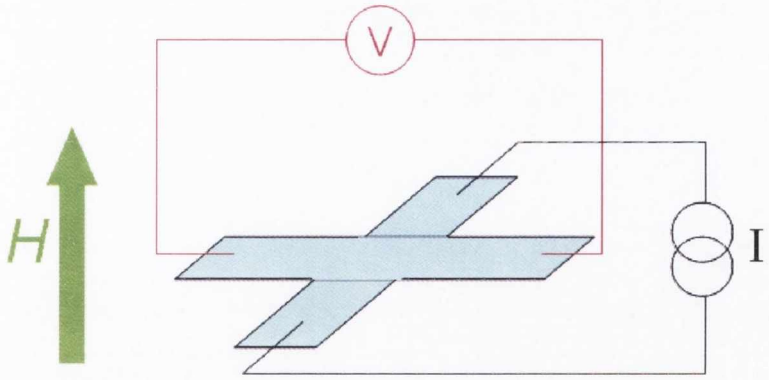

Figure 6.6: Experimental geometry for the EHE measurements on Co/Pt multilayers

shown on the right of Figure 6.5.

The individual 4×4 mm^2 devices were then extracted from the 25.4×25.4 mm^2 chips using the DISCO Automatic Wafer Dicer (see section 2.2.8). In order to protect the devices during dicing, another layer of S1813 was spun on the sample. The spin speed was 5000 rpm and the resist was then postbaked at 115 °Celsius for 1 minute. No UV exposure and no development took place. The wafer dicer was programmed to automatically cut each die from the center of the 25.4 × 25.4 cm^2 substrate. The blade height was 0.3 mm with a feed speed of 10 mm/s. The final chip size was 4.19 × 4.19 mm^2. Samples were contacted by pressing indium contacts that were attached to extended silver wire inside a sample box capable of being held inside the measurement electromagnet, in the R-T rig (as described in section 2.4.2).

All measurements were all conducted at the same sampling current and nominally the same field sweep rate (0.5 mT/s). This sweep rate was to ensure that the coercivities could be compared directly, and the current was chosen to avoid effects from sample heating etc. The field was applied along the film normal, whereas the current was in the plane of the sample. Longitudinal current was supplied while the transverse voltage was sensed using the 4-wire mode on the Keithley. The measurement geometry is show in Figure 6.6. The step size of the magnetic field was 0.5 mT and the sampling current was 600 μA.

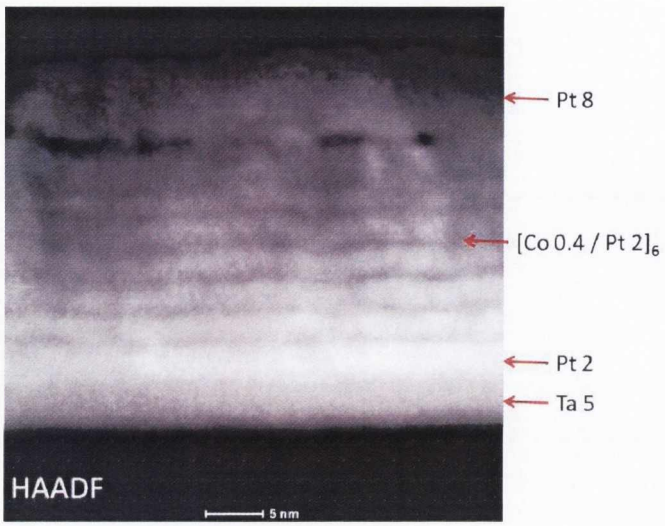

Figure 6.7: HAADF TEM image of a [Co 0.4 / Pt 2]$_6$ multilayer. Sample preparation is described in the text.

6.3 Initial Characterisation

Before ion irradiation, we characterised the patterned Hall bars of pristine layers using the extraordinary Hall effect and pristine planar films using SQUID magnetometry. A high angle annular dark field (HAADF) transmission electron microscopy (TEM) image of a pristine Co/Pt multilayer with a Co thickness of 0.4 nm is shown in Figure 6.7. TEM samples were prepared on a Carl Zeiss Auriga focused ion beam (FIB), and manipulated onto a Cu sample support for the TEM, in-situ. The sample final thinning was performed at a gallium ion accelerating voltage of 5 KeV. This reduces the sample amorphisation and gallium ion implantation in the lamella, compared to 30 KeV, leading to better insight into sample crystal structure, and a higher quality sample for high resolution transmission electron microscopy (HR-TEM)[2]. In HAADF mode, elements with higher Z number (such as Ta and Pt) appear brighter whereas lighter elements (such as Co) appear darker. We can clearly see the Co and Pt layers. From the TEM image we can be sure that we are working from a high quality platform comparable with state-of-the-art literature [14]. For the pristine samples we determined the coercivity for each sample

[2]TEM samples were prepared by Dr. Colm Faulkner and TEM imaging was performed by Dr. Markus Boese - both affiliated with the CRANN Advanced Microscopy Laboratory (AML)

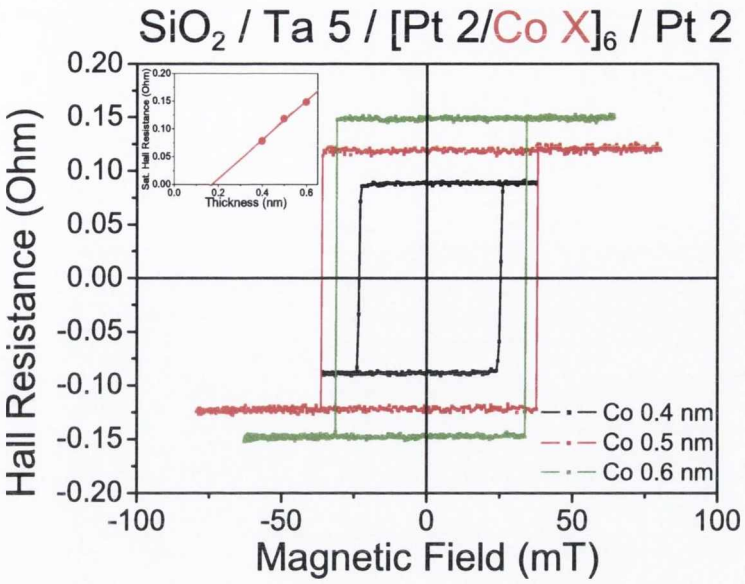

Figure 6.8: Typical Hall effect loops for 2 μm Hall bars patterned by UV lithography. The inset shows saturated Hall resistivity as a function of Co thickness

thickness. We also determined, from SQUID, the saturation magnetisation and the effective anisotropy K_{eff}. Typical extraordinary Hall effect (as described in section 2.4.3) loops for the patterned Hall bars are shown are shown in Figure 6.8. All thicknesses show clear perpendicular anisotropy with coercivities of ~35 mT. We can see that the saturated Hall resistivity increases with increasing ferromagnetic thickness (Figure 6.8 inset). The linear extraction of the fit of the coercivity versus saturated Hall resistivity extrapolates to zero at just below 0.3 nm. This implies that we would no longer have PMA below 0.3 nm. As the Hall resistivity is directly proportional to the magnetisation along the film normal, the Hall resistivity should scale with the out-of-plane magnetisation component, M_z. This can be attributed to the lack of a continuous film deposited in the Shamrock (see section 2.2.3).

The relationship between Hall resistivity and M_z is given in 2.4.3. The scaling factor between the Hall resistivity and the saturation magnetisation is called the extraordinary Hall coefficient, and is different for different materials. Since the magnetisation and resistance are related in $3d$ metals any sharp switch in magnetisation (along the perpendicular axis) manifests itself as a sharp change in the Hall voltage. This makes the extraordinary Hall effect an indirect

measure of magnetisation. To extract data on the real magnetisation, a magnetometer should be used. We only sample the component of magnetisation along the film normal within and around the area of the Hall cross. That is, the junction area where the current and voltage lines cross. It is therefore possible to probe all three junctions shown in Figure 6.5 independently.

The extraordinary Hall effect was used to characterise all samples in this chapter. The design size of the junctions was 2×2 μm^2, but after the patterning process the final size was closer to 3×3 μm^2. The reason for this is due to the process conditions, for example the edge bead of resist on the square substrate preventing full vacuum contact between the mask and substrate. Also the beam profile during ion milling can give angled side walls, all of which can increase the size of the final junction. We also conducted SQUID measurements of unpatterned and unirradiated multilayers in order to obtain absolute magnetisation data. We measured the magnetisation of the samples both in and out of the plane to calculate the saturation magnetisation, $\mathbf{M}_s$, and the anisotropy field, $\mu_0 H_a$ (Chapter 3).

Unpatterned 25.4×25.4 mm^2 samples were cut to 4×4 mm^2 chips for perpendicular measurements and 6×6 mm^2 chips for in-plane measurements using the DISCO DAD3220 Automatic Wafer Dicing Saw (see section 2.2.8). The size was chosen for the sample to fit neatly into the SQUID measurement straws. The magnetic moment was divided by the total magnetic volume to determine the magnetisation of each sample. Some SQUID data are shown in Figure 6.9. OP stands for out-of-plane and IP stands for in-plane. The increase in saturation magnetisation does not correspond to the increase in thickness. This is likely due to the uniformity from Chamber A as a result of the planetary motion which requires at least 15 seconds for a uniform layer. This corresponds to 0.15 nm steps (see section 2.2.3).

The saturation magnetization, $\mathbf{M}_s$, and anisotropy fields, $\mu_0 H_a$, (obtained by extrapolating the in-plane magnetisation curves to saturation) are tabulated together with the effective anisotropy in Table 6.1. The anisotropy constant is deduced from the anisotropy field

$$K_{eff} = \frac{\mu_0 H_a \mathbf{M}_s}{2} \tag{6.1}$$

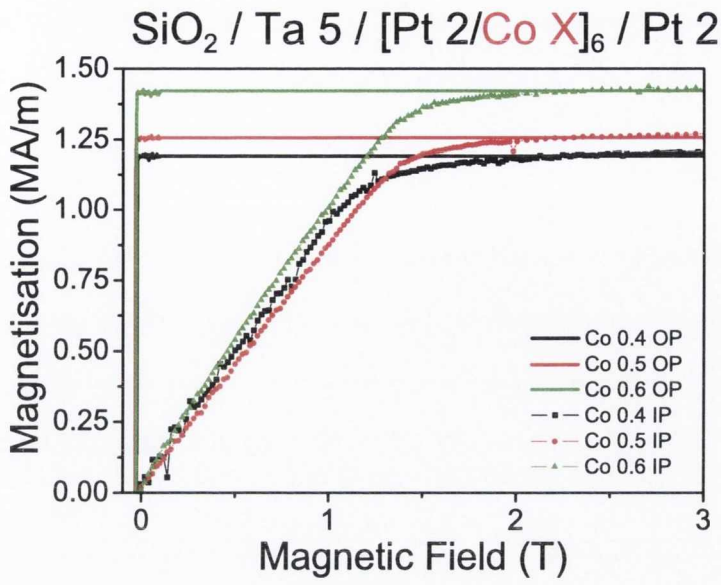

Figure 6.9: Volume normalised SQUID data for Co/Pt multilayers

Co Thickness	M_s	$\mu_0 H_a$	K_{eff}	$K_1.t$	δ_w
0.4 nm	1.18 MA/m	1.28 T	0.73 MJ/m^3	640 μJ/m^2	7.9 nm
0.5 nm	1.25 MA/m	1.43 T	0.89 MJ/m^3	933 μJ/m^2	7.3 nm
0.6 nm	1.41 MA/m	1.42 T	0.96 MJ/m^3	1339 μJ/m^2	6.6 nm

Table 6.1: Effective anisotropies for differing Co thickness's

Since $K_{eff} = K_1 - \frac{1}{2}\mu_0 \mathbf{M}_s$ we can determine K_1 per unit area (see section 3.1) which is expressed in the fifth column of Table 6.1. We can also determine the Bloch wall width $\delta = \pi\sqrt{A/K_1}$, given in column six, where A is the exchange stiffness, taken to be of the order of 10 pJ/m [15]. The effective anisotropy rises as the Co thickness is increased which indicates that we have both surface, K_s, and purely interfacial Néel type, K_N, anisotropy contributions to K_{eff} (section 3.1 and Figure 3.4). This decrease in anisotropy at lower thicknesses in the Co/Pt system has been previously observed [16]. We imply from this that in the case of our samples we are in the *coherent* regime where the film is uniformly strained due to the lattice mismatch with no defects. To compare to the bulk value of Co we determined the magnetic moment per Co atom. The saturation magnetisation of each Co thickness gives magnetic moments of 1.4 1.5 and 1.7 μ_B per atom for 0.4, 0.5 and 0.6 nm respectively. The bulk value of Co is 1.7 μ_B per atom.

The coercivity in Figure 6.8 shows a dependence on thickness and a maximum at 0.5 nm Co. Until a larger sample set is grown with a complete Co thickness dependence it is not possible to comment on this. We assume that the anisotropy will begin to follow the linear curve shown in Figure 3.4 as the Co thickness is increased. As the thickness is increased the volume anisotropy will increase as we are keeping the surface area constant. At these thicknesses of Co we expect that any interactions with ion irradiation will result in the relaxation of the magneto-elastic strain and destroy the sharpness of the interface. Such a reduction will manifest itself in a reduction in anisotropy energy and hence the coercivity. These local modifications can be measured by EHE in the Hall bar geometry.

6.4 Dose Tests

The patterned junctions were exposed to He^+ ions at various fluences and the EHE remeasured. Irradiations were carried out with Dr. Gavin Behan in the CRANN AML. The dose (in ions/cm^2) was calculated as a function of the ion current, dwell time and irradiated area.

$$\Phi = \frac{I_b t S}{A q} \tag{6.2}$$

S is the resolution of the image in pixels; for example 256x256 or 512x512. The resolution does not have an effect of the exposed area, but rather the beam stepsize. I_b is the beam current in amperes, t refers to dwell time in seconds, A corresponds to the field of view in the microscope or the exposed area (for patterning) in units of cm^2 and q is the electronic charge (1.6×10^{-19} C) of a single He^+ ion. It is important to note (again) that the beam used in this work is a focused beam that is rastered across the sample surface, unlike previous work using broadbeam ion sources [1].

It is possible to pattern both with the entire field of view of the microscope or to use bitmap images to pattern selected regions in a similar way to electron beam lithography. Using the bitmaps, individual pixels can be addressed and specific irradiations can be obtained.

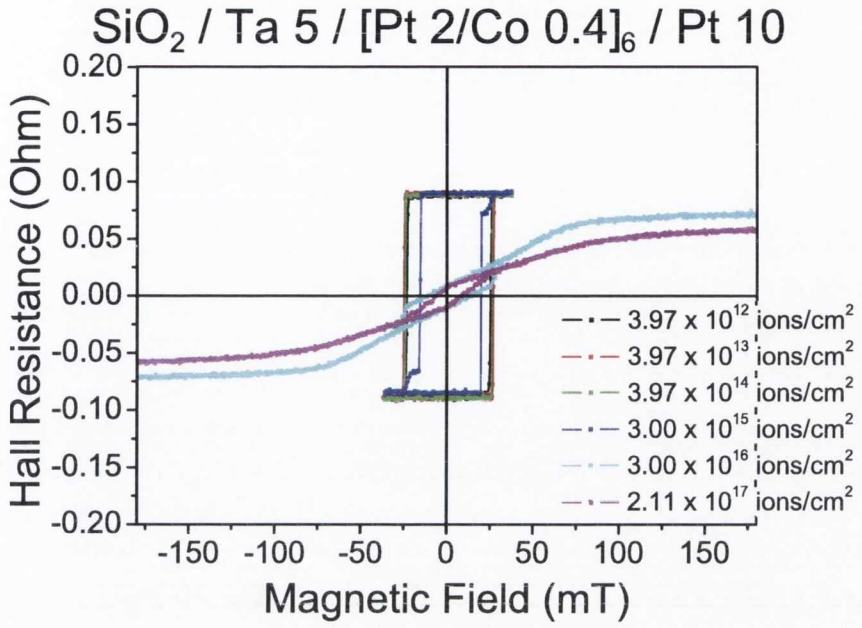

Figure 6.10: EHE loops as a function of dose for [Co0.4/Pt2]$_6$ 2 μm Hall bar

For the dose tests we irradiated an area larger than the junction area, 6.5×6.5 μm^2, using the entire field of view of the microscope. Individual junctions were dosed and in each set an unirradiated junction was used as a control to eliminate any time dependent effects on the anisotropy. We did not observe such a time dependent effect, but it is possible that it may occur in Pd based films [17]. Before each exposure the beam current was measured so an accurate dose could be calculated. We irradiated uniformly the junctions with doses ranging from 10^{12} to 10^{17} ions/cm^2. The results of exposures on multilayers with differing Co thicknesses are shown in Figures 6.10, 6.11 and 6.12.

All sample thicknesses show changes in perpendicular anisotropy and a fall in the coercivity as a function of dose (Figure 6.13). When we no longer measure coercivity we say we have lost the perpendicular anisotropy and the magnetisation in the junction area is in the plane. We can then define a critical dose Φ_{crit}, which is the dose required for the loss of coercivity in a perpendicular applied field. The dose required to destroy coercivity in all thicknesses is in the region of 10^{15} to 10^{16} ions/cm^2 (Figure 6.13).

The fall off in coercivity is due to the reduction of interfacial strain at the Co/Pt interface. It

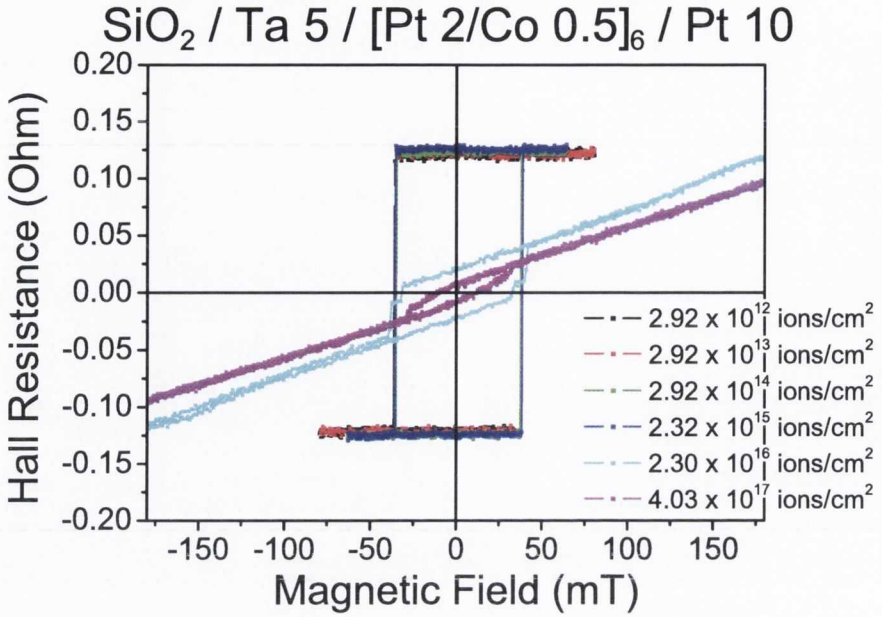

Figure 6.11: EHE loops as a function of dose for $[Co0.5/Pt2]_6$ 2 μm Hall bar

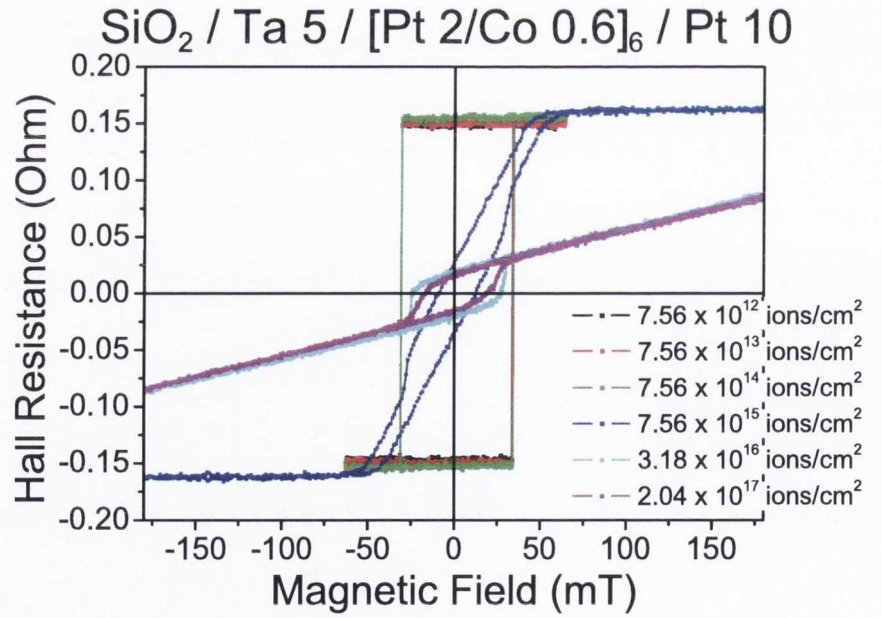

Figure 6.12: EHE loops as a function of dose for $[Co0.6/Pt2]_6$ 2 μm Hall bar

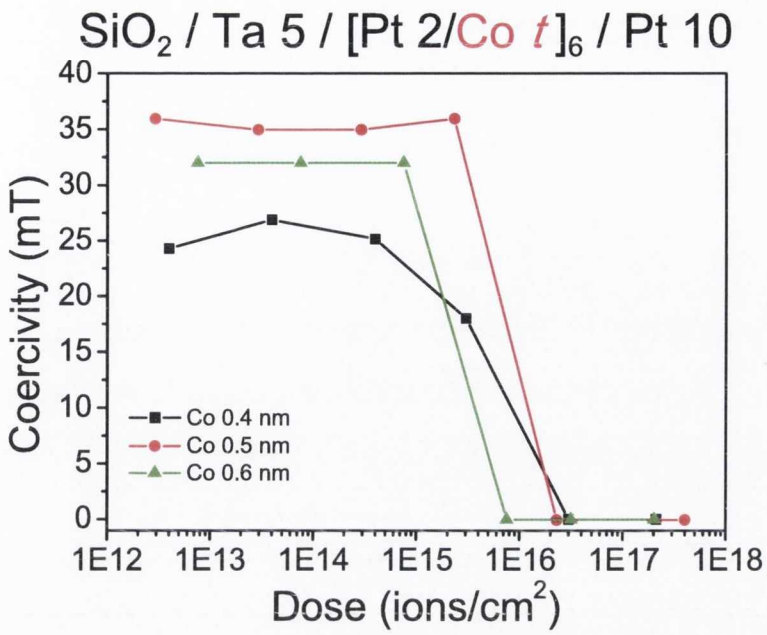

Figure 6.13: Coercivity as a function of dose for [Co t / Pt 2]$_6$ 2 μm Hall bars

was shown that He^+ ions cause the intermixing and alloying at the interface of Co and Pt [18]. This fall in coercivity was previously observed at similar fluences using 30 keV *broadbeam* He^+ ions [1]. The magnetic properties evolve first to reduce the coercivity and then the remanence. When the interface is suitably damaged, the shape anisotropy (which favours in-plane magnetisation) dominates the effective anisotropy and we lose the strong perpendicular anisotropy, as depicted in Figure 6.1.

At these doses we have a linear response of the magnetisation to the applied field indicating that we can still saturate the magnetisation along the perpendicular direction, but we have no remanence. It is noted that the slope of the line is too great to correspond only to the ordinary Hall effect ($R_H = -1/nq$ from section 2.4.3). The slope of the line for the ordinary Hall resistivity is inversely proportional to the carrier concentration. The slope is therefore still from the extraordinary Hall effect, further evidence for this is the ability to saturate the EHE signal at high fields. For example, in Figure 6.10 the EHE signal for an irradiated dose of 2.11×10^{17} is saturated at approximately 100 mT.

In the Hall bar geometry, since the leads are also made of the Co/Pt multilayer the hysteresis

seen at high fluences in the EHE curves most likely corresponds to the switching of an unirradiated part of the leads close to the junction area [19]. This hysteresis is always present and seems to be independent of the dose, suggesting that it does not originate from the irradiated area.

For a Co thickness of 0.4 nm, we can see clearly at a dose of 3.0×10^{15} ions/cm^2 in Figure 6.10 that we are lowering the coercivity locally within the Hall junction. When we no longer have remanence we notice that we increase the field required to saturate the Hall resistivity, $\sim$60 mT for a dose of 3.0×10^{16} ions/cm^2 and increasing to $\sim$80 mT for a dose of 2.11×10^{17} ions/cm^2. This implies that the anisotropy axis is more in-plane as the field required to saturate the magnetisation along the film normal is larger. As we increase to higher doses we also note a fall in saturated Hall resistivity. For $\Phi = 2.11\times10^{17}$ ions/cm^2, the saturated Hall resistivity has fallen by approximately 25% compared to the unirradiated sample. A decrease in Hall resistivity implies directly that the magnetisation of the irradiated area has decreased. This could be due to the physical removal of magnetic material, i.e. surface sputtering. Although physical removal of material should result in an increase in Hall resistance due to change in current flow in the stack, this change in resistance stemming from this should be small. In total for the stack shown in Figure 6.10 we have 5 nm of Ta, 22 nm of Pt and 2.4 nm of Co. As a percentage the Co represents less that 10% of the total structure. A decrease in non-magnetic thickness should yield some slight increase in saturated Hall resistance. This slight increase is most obvious in Figure 6.12. Increasing doses from 10^{12} ions/cm^2 to 10^{15} ions/cm^2 gives a small increase in the saturated Hall resistance. We attribute this to the milling of the surface Pt layer.

For the sample with Co 0.5 nm, we do not see the same intermediate fall in coercivity as we did for Co 0.4 nm. We do see a complete reduction in coercivity followed by a change in the slope of the Hall resistivity upon increasing the exposure dose. In Figure 6.11 the light blue curve (2.3×10^{16} ions/cm^2) saturates (or is close to saturation) at 180 mT indicating the reduction in the perpendicular component of the anisotropy axis. As we increase the dose we begin to modify the slope of the R-H curve. Comparing the doses of 2.3×10^{16} ions/cm^2 and 4.0×10^{17} ions/cm^2 we can see that we will saturate the magnetisation at different fields. We cannot verify this as the saturation field exceeds the field that can be applied by the magnet. However, we can

conclude that at higher doses we are still reducing the perpendicular anisotropy. As we increase the irradiation dose in-plane magnetisation is more favourable and out-of-plane magnetisation is less so. This will lead to an increase of the anisotropy field with increasing dose. After some time, however, we expect the anisotropy field to become constant.

For the thickest sample, Co 0.6 nm, we again see that we have a transition from strong perpendicular anisotropy to in-plane anisotropy. If we examine at Figure 6.12 and, in particular the R-H loop for $\Phi = 7.56 \times 10^{15}$ ions/cm^2 we can see that the remanence is reduced but the magnetisation saturates at about 50 mT. Since the saturated Hall resistivity is the same as that for lower doses with 100 % remanence we know that the component of magnetisation along the film normal must be the same. We have destroyed the perpendicular anisotropy but we have not reduced the magnetisation since the saturated Hall resistance is the same. We have irradiated with a dose slightly higher than the dose required to destroy the strong PMA. As we increase the dose we, again, begin to modify the slope of the R-H curve. From AFM measurements (discussed in section 6.7) we determined that surface sputtering with high doses is substantial. The drop in Hall resistivity we see here originates from actual magnetic material removal.

In order to learn more about the relationship between the irradiated and non-irradiated areas we took a fresh Co/Pt multilayer with a Co thickness of 0.4 nm and irradiated it at a dose of 6×10^{15} ions/cm^2. At this dose we still have 100 % remanence i.e. strong PMA, but we have reduced the coercivity. This implies that we still have perpendicular domains in the irradiated area. We show the EHE response of this junction in Figures 6.14 and 6.15. We see that we have a sharp switch around 15 mT with a tail around 30 mT. The sharp transition is due to the switching of the irradiated area. The tail is due to inhibited domain wall motion at the border between the irradiated and non-irradiated area of the junction. At the borders of the irradiated area we can have a lot of pinning sites from the irradiation, this would imply that as we increase the field beyond 25 mT then the fast domain wall motion associated with reversal in Co/Pt multilayers could be inhibited [6]. In Figure 6.14 we have overlayed the EHE loop of an unirradiated sample.

Although we expose an area larger than the junction it is still possible to sense some finite

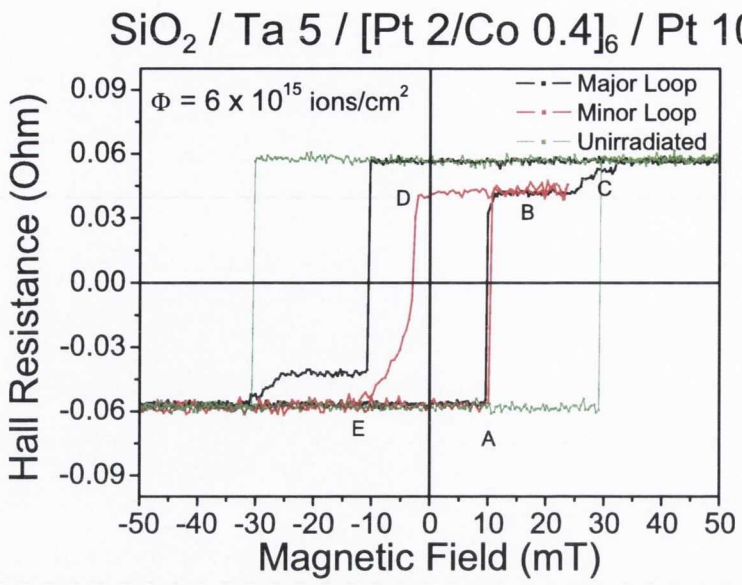

Figure 6.14: Minor loops of an irradiated [Co0.4/Pt2]$_6$ 2μm Hall bar

distance into the leads [19]. We scanned one full loop followed by a several minor loops (Figure 6.15). Figure 6.14 shows a full loop and a minor loop where we started to reverse the field sweep at 23 mT. The major and minor loops are the black and red curves respectively. We can see that there is coupling between the irradiated and non irradiated area. Along the major (black) loop, starting from high negative field (-180 mT) and sweeping the field towards the positive direction we observe the switch of the irradiated area at 10 mT (Point A). The Hall resistivity does not saturate, which means that there is some area we are sensing whose magnetisation has not switched yet. As reported before, we attribute this to an area around the junction itself that we also probe [19]. This non-irradiated area switches slowly at 30 mT (Point B). Sweeping the field in the reverse direction, we observe the switching of the irradiated area at -10 mT and the non irradiated area at -30 mT.

For the minor loop (red curve), if we reverse the field after 10 mT, when the irradiated area has switched (Point B) but before the non-irradiated area has switched (Point C), we can reverse the irradiated area at a much smaller field $\sim$ 4 mT (Point D). When the field is reversed before the inhibited domain motion (Point C) then at negative fields the Hall resistivity returns to its

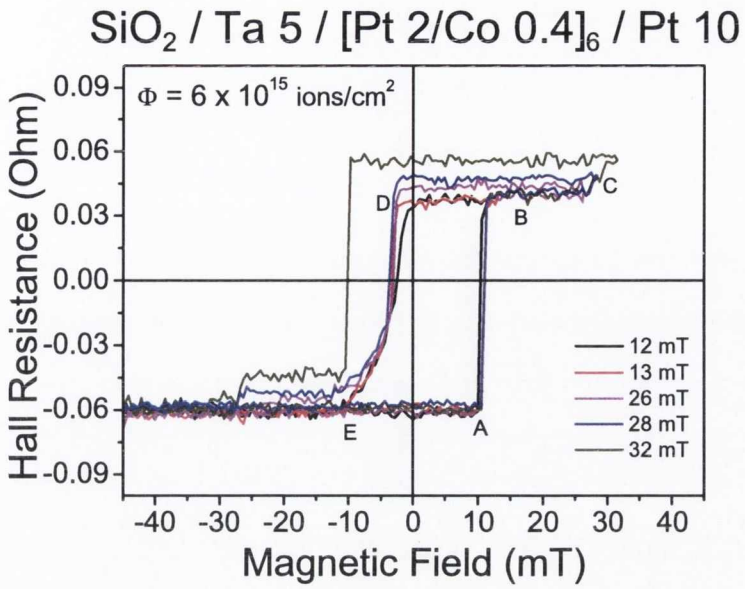

Figure 6.15: Minor loops of an irradiated [Co0.4/Pt2]$_6$ 2μm Hall bar irradiated at 6×10^{15} ions/cm^2

saturated value shortly after the irradiated area reversing (Point E of the red curve in Figures 6.14). We can reverse the field anywhere between 10 and 30 mT without affecting the reversal field for the irradiated area, it is always ~4 mT. That is, regardless of whether we reverse the field just after the switch at 10 mT or just before the switch at 30 mT, we do not affect the reversal of the irradiated area. This directly implies that we have magnetic coupling between the irradiated and non-irradiated areas.

We can also see that the switch for the non-irradiated area is not sharp. We can speculate that we have inhibited domain wall motion at the border between the irradiated and non-irradiated area. This can be due to either the topological effect of surface milling or the lateral straggle of the beam which will create an effective coercivity gradient, and we will therefore have irreversible domain wall motion at the edges of the irradiated area. This is evidenced directly in Figure 6.15 where we vary the field at which we start reversal around point C.

The reverse fields in Figure 6.15 are 12, 13, 26, 28 and 32 mT. If the field is reversed after the inhibited domain wall motion has started (in the region of Point C) then when the field is reversed the Hall resistivity has a plateau in the reverse direction (-10 to -30 mT) before reaching

its maximum value (32 mT curve in Figure 6.15).

Depending on where we stop around Point C, we will still have to apply a higher reverse field to fully saturate the junction area. This is consistent with small areas with a distribution of coercive fields. It seems that even with a focused beam, lateral straggle and "collateral damage" may be present. If we could quantify the size over which this inhibited motion takes place we could place a value in the fundamental limit of He^+ patterned media, similar to the quantification of shadow masked irradiations from [13].

6.5 Irradiation area dependence

As previously mentioned, it is obvious that we are probing an area outside the Hall cross area. In order to determine how the size of the irradiated area affected the reversal of the whole junction we systematically reduced the size of the irradiated area laterally from 6.5 $\times$ 6.5 μm^2 to 6.5 $\times$ 0.5 μm^2. We fixed the dose in this case to be 5×10^{15} ions/cm^2, the region where we see reduced coercivity in the junction area.

The measured EHE loops are shown in Figure 6.16 and the irradiation geometry is shown in the top-right of the figure. The saturated Hall resistivity is not modified for these doses as we are only reducing the interfacial anisotropy, the easy axis is still perpendicular to the film plane and we are not milling any magnetic material. We can only see the reduced coercivity for the largest boxes, 6.5 $\times$ 6.5 μm^2 and 6.5 $\times$ 6.0 μm^2. For smaller boxes we don't clearly see reduced coercivity. For the large sizes we see switching similar to that of an unirradiated junction. It is not possible to sense the irradiated area inside the junction because most of the Hall signal is coming from the unirradiated area.

The results do place a limit on EHE as a detection scheme for single small exposures. In so far as the irradiated area (or areas) should occupy a large portion of the area of the junction. We are confident that we are modifying the coercivity locally within the junction at this dose because of data obtained on full junction irradiations.

We have also patterned junctions with dense dot arrays (100 nm squares with 100 nm spac-

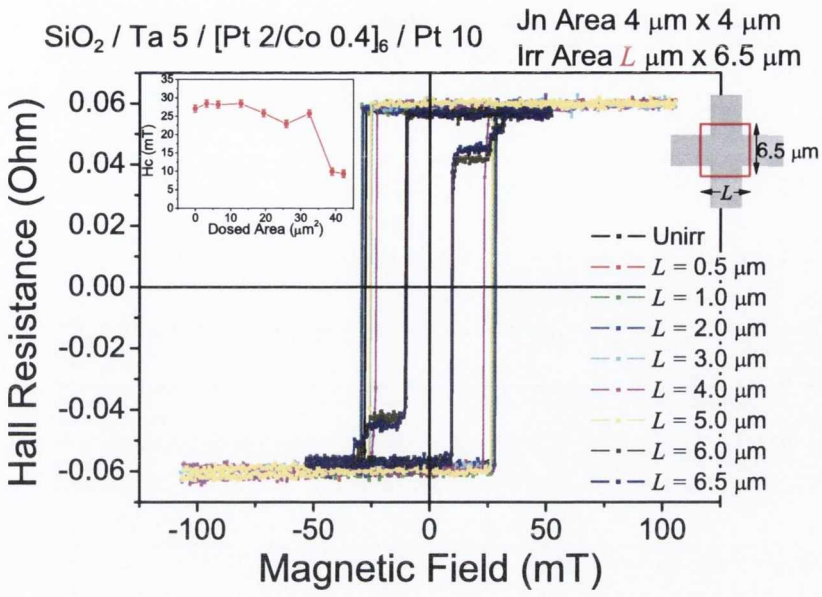

Figure 6.16: EHE loops of an irradiated $[Co0.4/Pt2]_6$ 2μm Hall bar with differing exposure areas. Inset: dependence of coercivity on dosed area

ing) within the junction area. These grid like patterns show modified hysteresis loops, shown in Figure 6.17. The results are difficult to interpret (much like foreign languages) in the context of few exposures. Irradiation of these grids at lower fluences results in loops that look similar to irradiations at higher fluences. The gaps and islands are larger than the calculated Bloch wall width (~10 nm, tabulated in Table 6.1). Both 10^{14} ions/cm^2 and 10^{15} ions/cm^2 grids result in EHE loops with no measured coercivity, low remenance and a significant drop in the saturated Hall resistance. Full junction irradiations at similar doses do not give the same results (also shown in Figure 6.17). The grid irradiations also have a noticeably lower saturated Hall resistance, similar to full junction irradiation of 2.1×10^{17} ions/cm^2. Since the saturated Hall resistance is proportional to $\mathbf{M}_z$ we know we have removed magnetic material from the junction,

At these doses we should only be modifying the anisotropy of the Co layers and milling only the capping Pt layer. If the effect of the grid shape is to introduce pinning sites then we need to take into account the lateral straggle of the beam. This might provide a path to patterning devices at lower doses. At lower doses we would avoid effects such as surface sputtering while

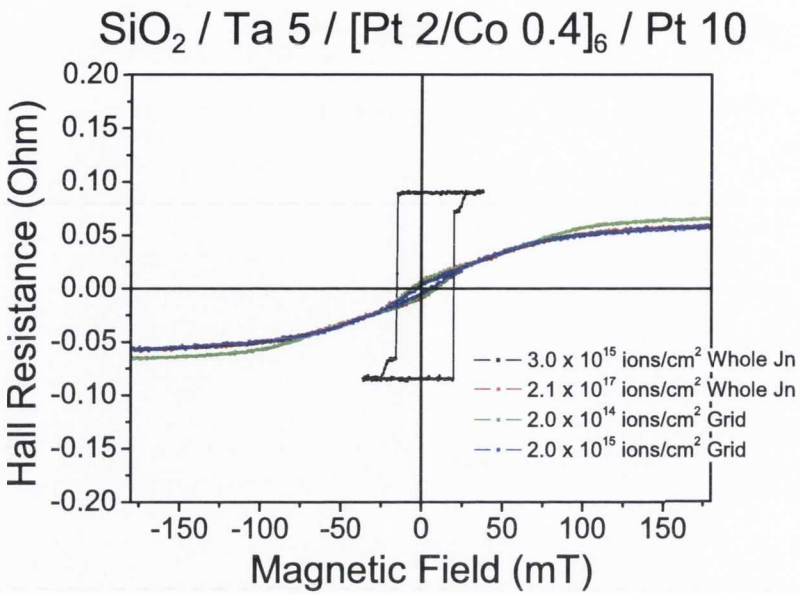

Figure 6.17: EHE loops of an irradiated $[Co0.4/Pt2]_6$ 2μm Hall bar for grid exposures and whole junction irradiations

clearly still modifying the hysteresis loop. We observe a drop in coercivity at the same doses as irradiations performed with a broadbeam [1] however the ion milling is not commented on in previous work. The nature of the rastered beam could be responsible. Ion milling is treated in section 6.7.

6.6 Calculations

Calculations on the doses were performed using freely available software called Stopping and Range of Ions in Matter (SRIM) [20]. SRIM software was used to determine the lateral straggle of the He^+, intermixing of layers and surface sputtering yields. The software was also used to calculate the range and straggle of the 30 keV He^+ ion beam in planar layers of Pt, Co and SiO_2. The distances, and calculated sputtering yield are tabulated in Table 6.2. The range of a 30 keV He^+ ion in Pt is 60 nm, whereas in Co and SiO_2 it is considerably larger. The consequence of this is that the ion beam will lose energy more rapidly as a function of distance with a Pt cap layer. The interaction with the underlying interfaces is therefore modified.

30 keV He^+ into	Projected range	Lateral straggle	Sputtering Yield (per incident ion)
Pt	60 nm	62 nm	< 1
Co	107 nm	64 nm	< 1
SiO_2	377 nm	124 nm	< 1

Table 6.2: Projected depth ranges and lateral straggle calculated for 30 keV He^+ into Pt, Co and SiO_2 using SRIM software [20].

The software was also used to calculate the number of collisions and displacements that typical dosing would cause. We assume that the area of the spot of the He^+ beam is 16 nm^2 [3]. We then scale the dose rate from ions/cm^2 to ions/nm^2, reducing by a factor of 10^{-14}. From this we get, 16, 160 and 1600 ions per pixel for doses of 10^{14}, 10^{15} and 10^{16} ions/cm^2. We use this for the number of ions in the simulations. The entire multilayer structure is constructed inside the simulation. We also simulate the interaction of the ions with the multilayer with a 0.1 nm and a 10 nm capping layer. We choose these two extremes as we are aware that we are milling the surface of the Pt cap. These simulations therefore represent the best (no milling) and worst (complete milling) case scenarios.

From simulations we are able to observe displacement of Co and Pt atoms within the structure. The penetration and distribution of atoms which are displaced due to collisions are shown in Figure 6.18. In the figure, the red lines represent the ion beam trajectories, green represents Pt atoms that have been displaced by ion collisions, blue represents Co atoms displaced by ion collisions. The ion beam can cause substitutional displacements, Co to Co, Pt to Pt, Co to Pt and Pt to Co. Since the modification of the interface is of interest here the substitutions of interest here are Co into Pt and Pt into Co. These will have a direct consequence on the PMA in the system due to the modification of interfaces.

From this figure the lateral straggle is clearly visible with the ion beam spreading up to 5 nm from the incident beam within the multilayer from the initial point of incidence. We can observe intermixing for the cases with and without the capping layer, represented by green (Pt displacement) and blue (Co displacement) dots at the Co/Pt interfaces. Without the capping layer we appear to have less mixing far from the point of incidence. The consequence of the

[3] the pixel spacing was 4 nm, the area of a pixel is 16 nm^2.

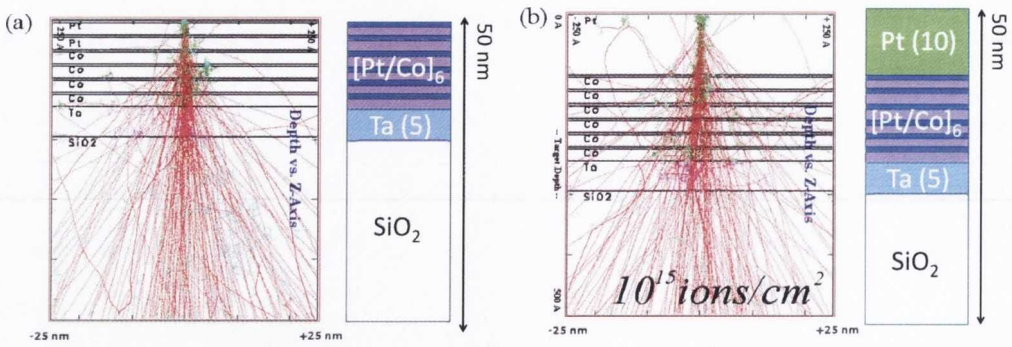

Figure 6.18: SRIM calculations for 10^{15} ions/cm^2 with 0.1 nm Pt capping layer (a) and 10 nm Pt capping layer (b)

thick capping layer is the increased spreading of the beam. Collisions in the capping layer will reduce the energy of the ion before it interacts with the Co/Pt interfaces [11]. The atomic displacements for scattering events are shown in Figures 6.19 to 6.21. We can clearly see in these figures the increased movement of Co atoms as a function of dose. The x-scale is the inverse of the displacement distance, so the lower the number the more the displacement. For example 35×10^6 corresponds to a displacement of 0.28 nm (an interatomic distance), where as 3×10^6 corresponds to $\sim$ 3.3 nm. The y-axis shows how the Co and Pt atoms move vertically in the stack. Here we can see if a Co atom is moved into the Pt layer and vice-versa by the colour legend.

For a dose of 10^{14} ions/cm^2 (Figure 6.19) we see that the beam interaction will displace the Co atoms out of the Co layer and roughen the Co/Pt interfaces. This does not occur throughout the entire stack, and the Co displacements are small in comparison to the Pt spacer thickness. Increasing the dose to 10^{15} ions/cm^2 (Figure 6.20) we have displacement of Co atoms across the Pt layer. At 10^{16} ions/cm^2 (Figure 6.21) we can see heavy intermixing of the Co/Pt interface with Co atoms, evidenced by the almost a continuous blue line at the left of (a) and (b) in Figure 6.21 for Co atoms both with and without Pt capping.

Such heavy intermixing at higher doses will result in a loss of an abrupt interface between Co and Pt. The effect of irradiation on intermixing and the roughening of the interface was investigated as a function of dose [6]. The SRIM calculations (Figures 6.19, 6.20 and 6.21)

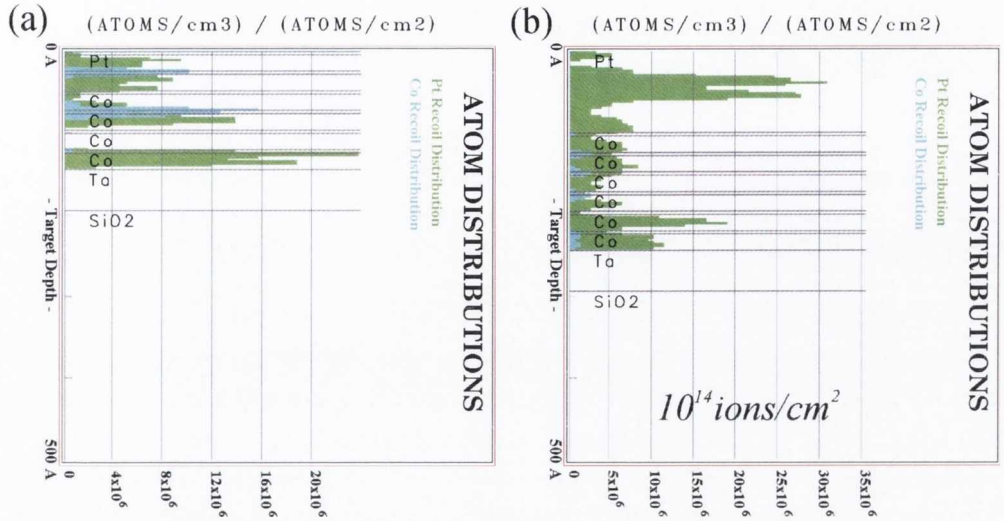

Figure 6.19: Atomic displacements for 10^{14} ions/cm^2 with 0.1 nm Pt capping layer (a) and 10 nm Pt capping layer (b)

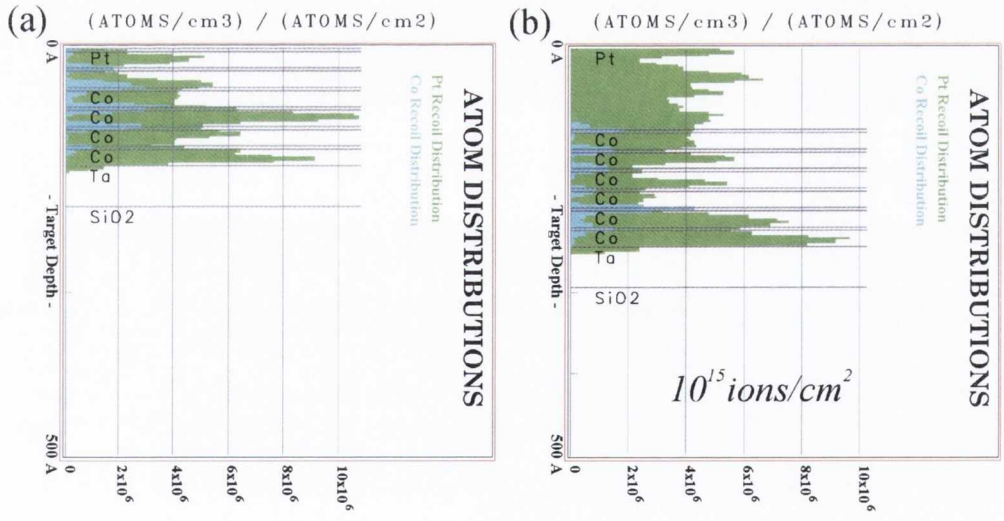

Figure 6.20: Atomic displacements for 10^{15} ions/cm^2 with 0.1 nm Pt capping layer (a) and 10 nm Pt capping layer (b)

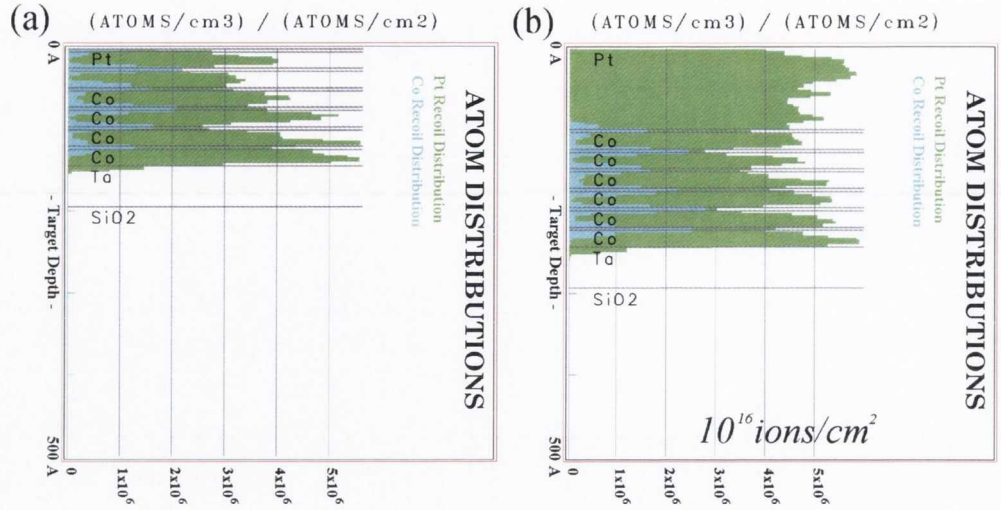

Figure 6.21: Atomic displacements for 10^{16} ions/cm^2 with 0.1 nm Pt capping layer (a) and 10 nm Pt capping layer (b)

correlate well to the loss of coercivity in the experimental data (Figures 6.10, 6.11and 6.12). We see no real change up to 10^{15} ions/cm^2, and a loss of coercivity at fluences of the order 10^{16} ions/cm^2.

6.7 Magnetic/Atomic Force Microscopy

6.7.1 Magnetic Information

Since we are modifying the magnetic structure it would seem prudent to obtain some real magnetic information from the irradiated junctions. This was accommodated using the magnetic version of the atomic force microscopy (AFM), magnetic force microscopy (MFM). A magnetic cantiliver tip is used as a sensing probe. This method gives information regarding topology as well as domain structure of the sample.

After the EHE measurement the samples are uniformly magnetised, it is necessary to demagnetise them. This is accomplished using a high frequency AC magnetic field that is decreased in systematic steps until zero field.

Figure 6.22 shows an MFM scan of the [Co 0.4 / Pt] multiayer that was irradiated at 3.0×10^{15} ions/cm^2. The EHE loops was shown previously in Figure 6.10. When imaged using MFM, the large irradiated area of demagnetised samples shows domain structure. This confirms that we have merely reduced the perpendicular anisotropy within the junction area. At the borders of the irradiated and non-irradiated areas we can see domain walls. This suggests that the border acts as a domain wall pinning site.

The moment from the AFM tip can be enough to uniformly magnetise the irradiated area but not the un-irradiated area. Evidence of this can be seen in Figure 6.22 where the domain structure inside the cross is modified between two scans. In the center of the first scan we can make out domain structure (blue maze domain lines). After the second scan we find no domain structure indicating a saturated state, which can only be caused by the moment from the AFM tip.

AFM/MFM scans were conducted with the help of Dr. Zhu Diao and summer student James Kally.

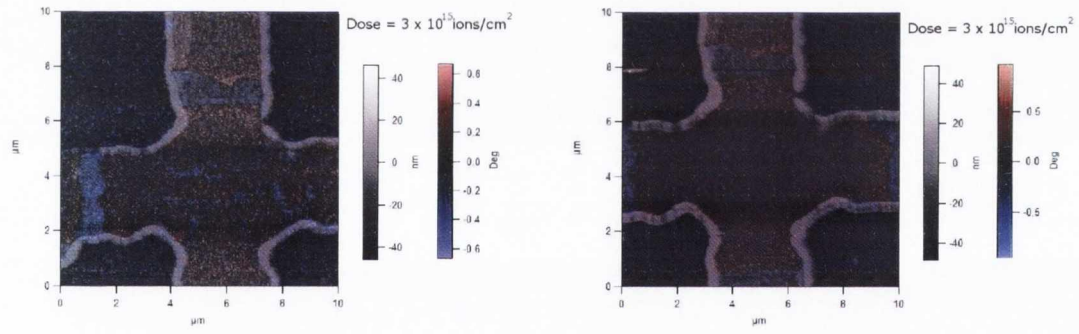

Figure 6.22: Sequential MFM images showing the switching of the irradiated area using the moment of the AFM tip, on the left we can see domain structure in the initial scan, on the right the tip moment has saturated the irradiated area and domains can no longer be seem

6.7.2 Surface Milling

AFM was initially done at the same time as the MFM scan presented in Figure 6.22. A linescan obtained from that AFM scan is shown in Figure 6.23. Approx 6 nm of material was removed

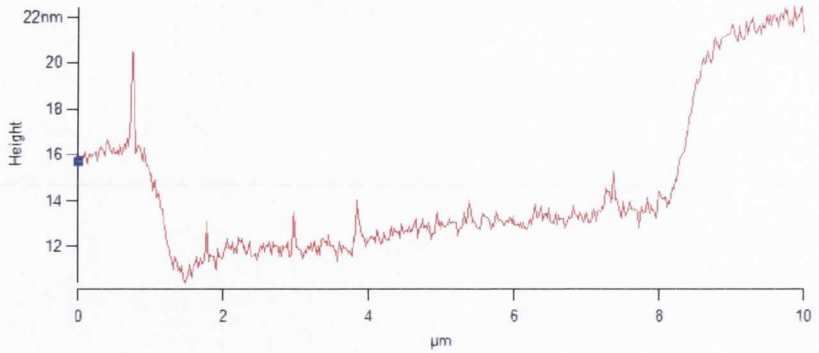

Figure 6.23: AFM linescan for a Hall junction exposed at 3×10^{15} ions/cm^2

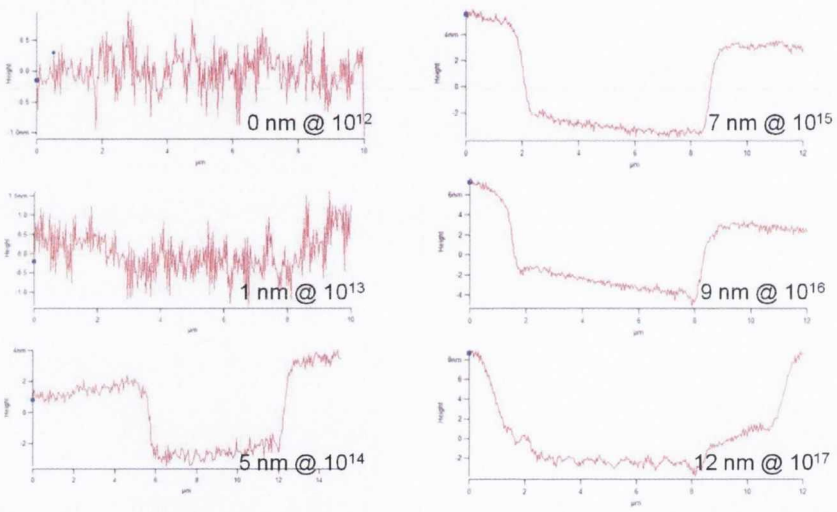

Figure 6.24: AFM linescans for all exposed doses on Hall bar junctions

from the top of the sample at a dose of 3×10^{15} ions/cm^2. All linescans are shown in 6.24.

We can calculate the sputter yield for this dose. The volume of a 6 nm thick 1×1 cm^2 slab of Pt is 6×10^{-7} cm^3. Using ρ_{Pt}=21.45 g/cm^3, Avagrado's constant $A = 6.022 \times 10^{23}$ atoms/mol and the atomic weight of Pt 195.06 g/mol, the number of atoms in this slab is therefore 3.9×10^{16} atoms.

Since the dose was 3×10^{15} ions/cm^2 we simply divide the two quantities to obtain the sputter yield. For every incident 30 keV Helium ion at this dose 13 Pt atoms are sputtered. More details of sputtering can be found in section 2.2.1 and [21]. SRIM calculations give sputter yields far below this value, < 1 atom/incident He$^+$ ion. The fact that we see significant

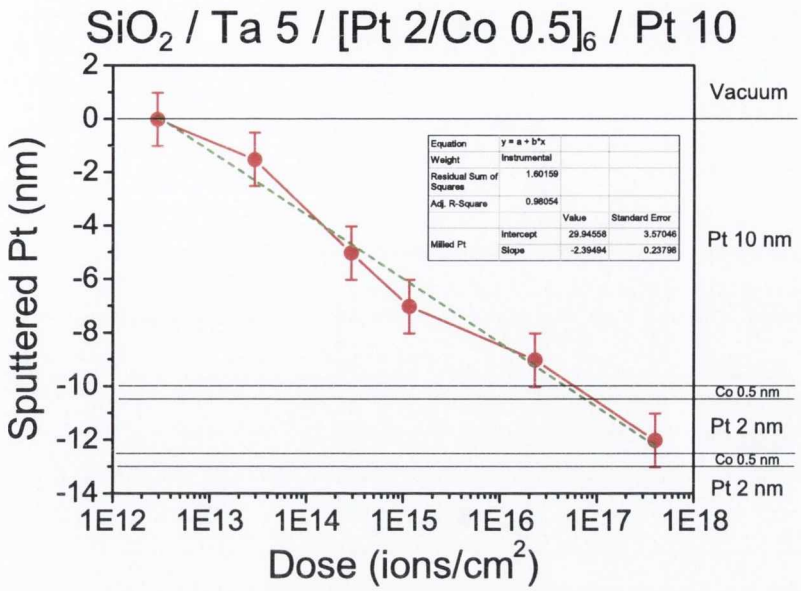

Figure 6.25: Ion milling depth as a function of dose for Pt

surface sputtering casts into doubt the usefulness of the SRIM simulations. However given the fact that the dose ranges are approximately correct in terms of intermixing, we assume that the effect of surface sputtering is not taken into account correctly in the SRIM code. Since the He^+ beam is rastered across the sample it is possible that we may have significant surface heating. Other reports of surface milling (2 nm with 75 keV He^+ in [22]) cannot be replicated in the SRIM code.

To characterise the surface milling we conducted AFM scans on a complete range of doses, specifically we used the junctions that were presented in Figure 6.11. The Co thickness in this case was 0.5 nm, several AFM linescans were performed on irradiated junctions and the milling depth was determined for each dose. We then plotted the milling depth against the irradiated dose. The dose, Φ, ranged from 10^{12} - 10^{17} ions/cm^2. These data are plotted in Figure 6.25.

It is remarkable that that the amount of Pt removed scales as the log of the dose. The beam current was kept constant (3 pA) for all the irradiations except 4.03×10^{17} ions/cm^2 (52 pA). It seems unlikely that the log dependence seen in Figure 6.25 is a result of a change in spot size as the beam current was not changed for the majority of doses. The exposure parameters are

Dose (ions/cm^2)	Beam current (I_b)	Dwell time (t)	S	A
2.92×10^{12}	3 pA	1 µs	256^2	6.5 µm
2.92×10^{13}	3 pA	10 µs	256^2	6.5 µm
2.92×10^{14}	3 pA	100 µs	256^2	6.5 µm
2.32×10^{15}	3 pA	100 µs	512^2	6.5 µm
2.30×10^{16}	3 pA	500 µs	1024^2	6.5 µm
4.03×10^{17}	52 pA	500 µs	1024^2	6.5 µm

Table 6.3: Exposure parameters for irradiations from which the ion milling rate was calculated

given in Table 6.3.

At high doses of 10^{17} ions/cm^2 we have 12 nm milling, this indicates that our previous estimation of the He$^+$ ions aggressively sputtering seems to be an issue. If we now re-analyse Figure 6.10 the drop in Hall resistivity is assumed to originate from the ion milling and surface sputtering of the top Pt and the first (or second) magnetic layer. The reduction in saturated Hall resistivity for a dose of 2.11×10^{17} ions/cm^2 in Figure 6.10 is approximately 25%. As we have six Co repeats in our multilayer milling one of these layers away will result in a magnetisation reduction of 16%, milling two would result in a 32 % reduction. Although this is not an exact match, we can explain some of the reduction of the Hall resistivity through surface and magnetic layer milling.

Ion milling with focused He$^+$ ions was reported in literature on suspended graphene layers [23]. They performed linescans with doses from 3 to 15 nC/cm. Taking the charge on an ion to be 1.9×10^{-19} C, 3 nC/cm corresponds to 1.8×10^{10} ions/cm or, expressed per unit area, 3.24×10^{20} ions/cm^2. This was not investigated systematically with AFM, the authors merely comment that from AFM they obtain a dip of 4 nm in graphene at a dose of 20 nC/cm. Milling using He$^+$ was also reported during the magnetic patterning of FePt [22]. Using a 75 keV projected He$^+$ beam, 2 nm of material was milled at an ion dose of 10^{16} ions/cm^2. The increased milling could be due to the lower energy used in our experiment.

6.8 Conclusions

We have shown *local* control over the perpendicular magnetic anisotropy in Co/Pt multilayers using a *focused* He^+ ion beam. We were able to determine the dose range required to selectively reduce the magnetic anisotropy and create areas of reduced coercivity whose switching could be observed by EHE. MFM scans show that in locally irradiated areas we can modify the magnetic properties and that the edges of the irradiated areas form domain wall pinning sites. Minor loops have shown that there is a large coupling between the irradiated and non irradiated areas.

Surface milling using a focused He^+ ion beam was investigated systematically and a relationship between the etch rate and the dose was determined. The etch rate was found to vary as the log of the dose. We are modifying the interfacial anisotropy in the same dose region as reported before [1]. However in our case ion milling seems more aggressive than previous reports [22]. This could be related to the scanning nature of the beam. Evidence for this is the drop in saturated Hall resistivity with chequerboard patterns at low doses, Figure 6.17. Further investigating is required to determine the nature of the logarithmic dependence of milling on dose.

The He^+ ion microscope holds promise both as a magnetic and topological patterning tool. Thicker overlayers are required to magnetically pattern buried layers without milling the magnetic layers. Patterning of thin films using the He^+ ion microscope may prove useful in preparing small nanometer scale samples without the associated damage caused by Ga^+ ions.

However, the speed at which the He^+ beam can pattern (either magnetically or topologically) is limited. To pattern a Co/Pt layer, such as the one presented here, for use as bit-patterned media using this method would require a long time (possibly days). Such a long exposure time would make the technique redundant as it offers no real advantage over what was previously presented in the literature. That said, however, the use of the He^+ beam to create coupled areas in perpendicular media would provide a useful insight to the physics of the reversal processes on the nanometer scale. If a more in depth study of the coupling of irradiated and non-irradiated areas (from section 6.7) using MFM was conducted, specific mechanisms of domain wall nucleation

and possibly even domain wall motion could be explored.

Bibliography

[1] Chappert, C., Bernas, H., Ferré, J., Kottler, V., Jamet, J.-P., Chen, Y., Cambril, E., Devolder, T., Rousseaux, F., Mathet, V., Launois, H. *Science* **280**(5371), 1919–1922 (1998).

[2] Carcia, P.F. *Journal of Applied Physics* **63**(10), 5066–5073 (1988).

[3] Fowley, Ciaran and Decorde, Nicolas and Oguz, Kaan and Rode, Karsten and Kurt, Huseyin and Coey, J. M. D. *IEEE Transactions on Magnetics* **46**(6), 2116–2118 JUN (2010).

[4] Chappert, C., Beauvillain, P., Bruno, P., Chautineau, J.P., Galtier, M., Le Dang, K., Marlire, C., Mgy, R., Renard, D., Renard, J.P., Seiden, J., Trigui, F., Veillet, P., Vlu, E. *Journal of Magnetism and Magnetic Materials* **93**(C), 319–325 (1991).

[5] Ravelosona, D., Chappert, C., Mathet, V., Bernas, H. *Applied Physics Letters* **76**(2), 236–238 (2000).

[6] Devolder, T. *Physical Review B - Condensed Matter and Materials Physics* **62**(9), 5794–5802 (2000).

[7] Faulkner, C.C., Atkinson, Del., Allwood, D.A., Cowburn, R.P. *Journal of Magnetism and Magnetic Materials* **319**(1-2), 9–12 (2007).

[8] Kerr, E., Van Dijken, S., Langford, R.M., Coey, J.M.D. *Journal of Magnetism and Magnetic Materials* **290-291 PART 1**, 124–126 (2005).

[9] Persson, A., Thornell, G., Nguyen, H. *Journal of Micromechanics and Microengineering* **20**(5), 055039 (2010).

[10] Bilzer, C., Devolder, T., Chappert, C., Plantevin, O., Suszka, A.K., Hickey, B.J., Lamperti, A., Tanner, B.K., Mahrov, B., Demokritov, S.O. *Journal of Applied Physics* **103**(7), 07B518 (2008).

[11] Urbaniak, M., Kuwik, P., Kurant, Z., Tekielak, M., Engel, D., Lengemann, D., Szymanski, B., Schmidt, M., Aleksiejew, J., Maziewski, A., Ehresmann, A., Stobiecki, F. *Physical Review Letters* **105**(6), 067202 (2010).

[12] Stanescu, D., Ravelosona, D., Mathet, V., Chappert, C., Samson, Y., Beign, C., Vernier, N., Ferré, J., Gierak, J., Bouhris, E., Fullerton, E.E. *Journal of Applied Physics* **103**(7), 07B529 (2008).

[13] Devolder, T., Chappert, C., Chen, Y., Cambril, E., Bernas, H., Jamet, J.P., Ferré, J. *Applied Physics Letters* **74**(22), 3383–3385 (1999).

[14] Hellwig, O., Bosworth, J.K., Dobisz, E., Kercher, D., Hauet, T., Zeltzer, G., Risner-Jamtgaard, J.D., Yaney, D., Ruiz, R. *Applied Physics Letters* **96**(5) (2010).

[15] Kambersky, V., De Haan, P., Łimov, J., Porthun, S., Gemperle, R., Lodder, J.C. *Journal of Magnetism and Magnetic Materials* **157-158**, 301–302 (1996).

[16] Guo, V.W., Lu, B., Wu, X., Ju, G., Valcu, B., Weller, D. *Journal of Applied Physics* **99**(8), 08E918 (2006).

[17] Li, L., Wen, F.S., Zhang, F., L, Y.F., Lu, Y.F., Liu, Z.Y., Xu, B., Yu, D.L., He, J.L., Tian, Y.J. *Journal of Applied Physics* **107**(12), 123912 (2010).

[18] Fassbender, J., Ravelosona, D., Samson, Y. *Journal of Physics D: Applied Physics* **37**(16), R179–R196 (2004).

[19] Aziz, A., Bending, S.J., Roberts, H., Crampin, S., Heard, P.J., Marrows, C.H. *Journal of Applied Physics* **98**(12), 1–4 (2005).

[20] Ziegler, J.F. *available from http://www.srim.org* .

[21] Sigmund, P. *Physical Review* **184**(2), 383–416 (1969).

[22] Bruenger, W.H., Torkler, M., Dzionk, C., Terris, B.D., Folks, L., Weller, D., Rothuizen, H., Vettiger, P., Stangl, G., Fallmann, W. *Microelectronic Engineering* **53**(1), 605–608 (2000).

[23] Bell, D.C., Lemme, M.C., Stern, L.A., Williams, J.R., Marcus, C.M. *Nanotechnology* **20**(45), 455301 (2009).

Chapter 7

Conclusions

"Are you writing conclusion?"

- H. Tokuc, PhD candidate

7.1 Conclusions

We have investigated perpendicular magnetic anisotropy by the extraordinary Hall effect. The extraordinary Hall effect is extremely sensitive to the magnetisation component perpendicular to the plane of the sample. We are able to prepare, in our Shamrock system, high quality layers with perpendicular magnetic anisotropy. Co/Pd layers prepared in this fashion show perpendicular anisotropy up to large thicknesses [1]. Our CoFeB layers also show perpendicular anisotropy at small thicknesses which shows the high quality of our sputtered layers.

We determined the anisotropy for the CoFeB/Pd interface and exploited this in terms of electric field modification of anisotropy. We find clear evidence of perpendicular magnetic anisotropy in the system up to a CoFeB thickness of 0.7 nm provided a seed layer of Pd is provided. By conducting SQUID measurements along the hard axis we determined the anisotropy energy density K_{eff} and hence the relative contributions for the volume and surface. From SQUID there is an elevated moment which is attributed to an induced moment of 0.6 μ_B per Pd atom and is consistent with literature [2]. We determined the surface anisotropy contribution

to be 0.32 mJ/m^2. We then replaced one of the Pd layers with MgO, a commonly used tunnel barrier material for magnetic tunnel junctions. In this case the CoFeB layer was shown to be superparamagnetic with a blocking temperature of 230 K.

We also investigate the PMA in the MgO/CoFeB/Pt system as a function of annealing temperature and Pt cap layer thickness. We find that 2 nm of Pt is optimum for the oxidation of the MgO/CoFeB interface.

The effect of an electric field on the anisotropy was opposite in the case of MgO/CoFeB/Pd and MgO/CoFeB/Pt indicating that the origin of the anisotropy is different in both cases even though we have PMA in both systems. Also, the measured electric field modification of anisotropy is very small, of the order of a few % in both the CoFeB/Pd and CoFeB/Pt systems. As a result of this it would not seem possible to exploit this effect for magnetic recording. This is unfortunate as the effect has held high hopes for the future of low-power recording. The reason why the effect is small is due to the fact that it is difficult to modify the electronic density by more than 0.1 electrons per interfacial atom. In calculations it is always easy to apply fields up to 1 V/Å but these are experimentally unfeasible.

In Chapter 5 it was observed that an electric field which charges the ferromagnet/insulator surface is sufficient to modify the anisotropy energy as reported before [3] [4] [5]. The system we employ is much more feasible than a bottom up approach employed by other groups [4] [5] in terms of the electric fields we can apply. However this is still not enough.

The system also allows for investigation of the origins of the perpendicular anisotropy in these oxide/ferromagnetic systems. Purely magneto-elastic effects will be symmetric in applied electric fields. The fact that we have an anti-symmetric response indicates we are affecting magneto-crystalline anisotropy with applied voltage.

To modify the magneto-elastic contribution to the perpendicular anisotropy we used a Carl Zeiss He^+ Ion Orion microscope to locally irradiated 2 μm Hall bar junctions. We were able to locally modify the coercivity and perpendicular anisotropy in the junctions. As a result of MFM investigations we observed surface milling with increasing dose. This new phenomena could be used for nanoscale patterning. Its advantage over traditional focused ion beam lithography

(with Ga^+) is the reduced ion damage due to the larger penetration depth of the helium ions. Such a tool is useful therefore in both magnetic and topological patterning.

7.2 Future Work

In terms of future work, it would be interesting to attempt to build a magnetic tunnel junction using the perpendicular MgO/CoFeB/Pt electrode. So far electrodes have not shown high TMR due to the lack of [001] texture required for spin-dependent tunneleing of the electrons.

Since the PMA in the MgO/CoFeB/Pt system shows great dependence on both the Pt cap layer thickness, investigation by the extraordinary Hall effect and applied electric fields can shed light on the nature of the O-bonding at the interface. The PMA in the CoFeB/MgO system is, at present, poorly understood. Boron diffusion in MTJs has also caused much debate in the literature [6]. A nice study of the perpendicular anisotropy in the CoFeB/MgO system would include detailed study of the appearance of PMA with different underlayers such as Pt, Pd and Ta.

Complementary to this would be the modification of the PMA through surface charging. The effect Ta/CoFeB/MgO system has been reported [5]. The effect in Pt/CoFeB/MgO is shown here. The effect is the same sign, but different magnitude. Undertaking the study of surface charging at various steps in the annealing temperature / thickness / remanence plot (Figure 5.14) would shed light on the origin of the anisotropy (MgO or underlayer interface). It might also be possible to optimise the thickness and annealing conditions to maximise the effect.

The investigation of the interface between the irradiated and non-irradiated areas by MFM would provide information on the coupling at a scale associated with the beam probe size ($\sim$ 5 nm). Such lithography with common photoresists is extremely difficult. Even with traditional focused beams (Ga^+) magnetic damage is prevalent, often up to 100's of nm [7] [8]. With the focused He^+ beam such magnetic damage is not believed to be be so large [9] [10]. In regards to contamination from the focused beam, He^+ ion lithography could offer superiority in thin film TEM sample preparation over Ga^+.

Bibliography

[1] Fowley, Ciaran and Decorde, Nicolas and Oguz, Kaan and Rode, Karsten and Kurt, Huseyin and Coey, J. M. D. *IEEE Transactions on Magnetics* **46**(6), 2116–2118 JUN (2010).

[2] Pasyuk, V.V., Lauter, H.J., Johnson, M.T., den Broeder, F.J.A., Janssen, E., Bland, J.A.C., Petrenko, A.V., Gay, J.M. *Journal of Magnetism and Magnetic Materials* **121**(1-3), 180–184 (1993).

[3] Weisheit, Martin and Faehler, Sebastian and Marty, Alain and Souche, Yves and Poinsignon, Christiane and Givord, Dominique. *Science* **315**(5810), 349–351 JAN 19 (2007).

[4] Maruyama, T. and Shiota, Y. and Nozaki, T. and Ohta, K. and Toda, N. and Mizuguchi, M. and Tulapurkar, A. A. and Shinjo, T. and Shiraishi, M. and Mizukami, S. and Ando, Y. and Suzuki, Y. *Nature Nanotechnology* **4**(3), 158–161 (2009).

[5] Endo, M. and Kanai, S. and Ikeda, S. and Matsukura, F. and Ohno, H. *Applied Physics Letters* **96**(21) MAY 24 (2010).

[6] Kurt, H., Rode, K., Oguz, K., Boese, M., Faulkner, C.C., Coey, J.M.D. *Applied Physics Letters* **96**(26), 262501 (2010).

[7] Persson, A., Thornell, G., Nguyen, H. *Journal of Micromechanics and Microengineering* **20**(5), 055039 (2010).

[8] Kerr, E., Van Dijken, S., Langford, R.M., Coey, J.M.D. *Journal of Magnetism and Magnetic Materials* **290-291 PART 1**, 124–126 (2005).

[9] Devolder, T. *Physical Review B - Condensed Matter and Materials Physics* **62**(9), 5794–5802 (2000).

[10] Devolder, T., Chappert, C., Chen, Y., Cambril, E., Bernas, H., Jamet, J.P., Ferré, J. *Applied Physics Letters* **74**(22), 3383–3385 (1999).

Appendix A

Ion Milling and SIMS in the Millatron

Ion Milling with the Millatron using Secondary Ion Mass Spectroscopy (SIMS)

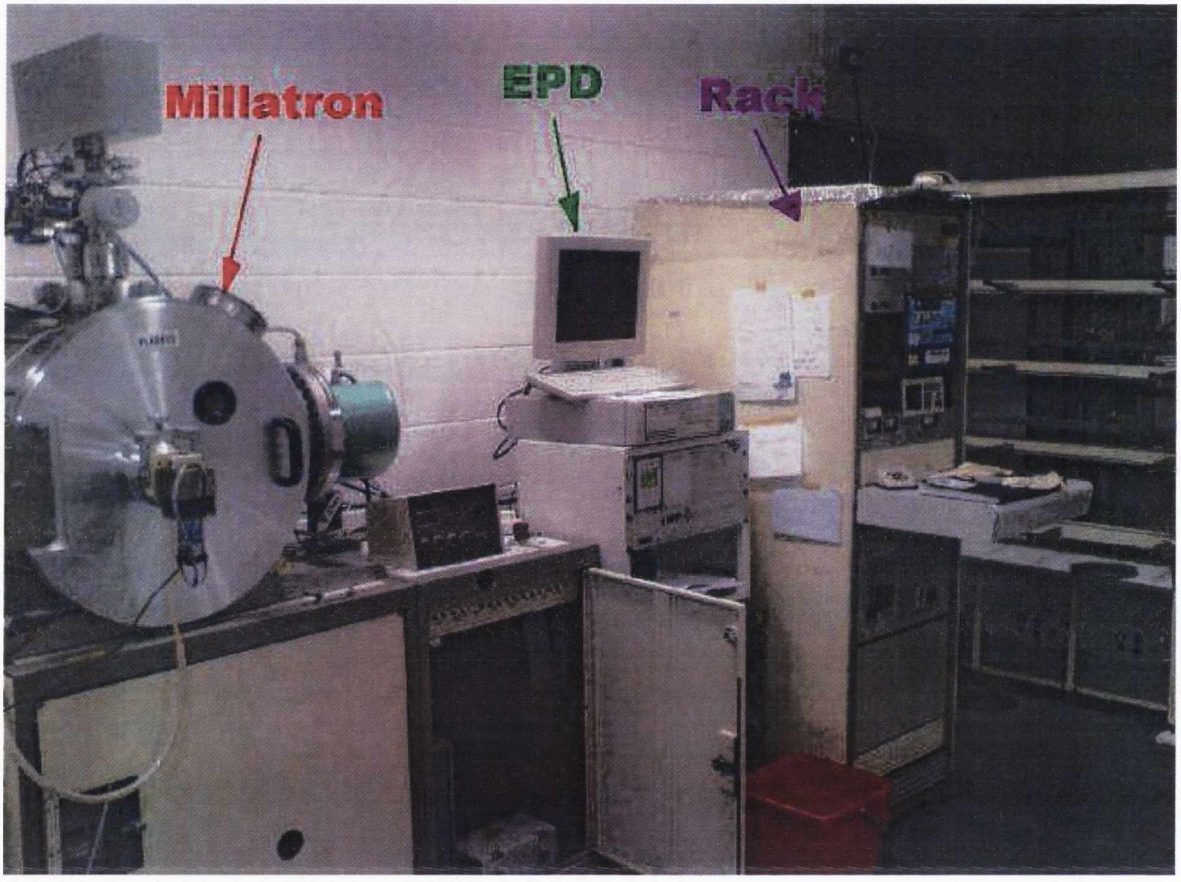

This manual was written with the help of Dr. Karsten Rode

Introduction

The Millatron is a broad beam ion milling tool which uses an Argon plasma to etch samples located on a rotating stage. It has a Hiden Analytical secondary ion mass spectrometer (WR12386; fitted 2007) which is used to monitor the materials etched in the chamber. It has a typical base pressure of 10^{-6}, RF forward power is 400W.

The sample stage was refitted (along with the chamber door in Summer 2007), the door was assembled by Plassys in Paris, France. The stage rotates at a fixed speed, metallic areas of the stage are protected by carbon to minimise interference with the SIMS scanning, the only SIMS contribution is from the stainless steel clips that hold the wafer in place during milling (keep this in mind during SIMS scanning).

The SIMS monitors the ions that are milled away from the sample on the stage. Depending on the milling angle variable voltages on plates inside the SIMS are set to deflect charged ions into a quadrupole mass spectromemter which is tuned to a particular mass. The quadrupole specifies a particular mass using AC and DC electric fields to only allow passage of a particular charge/mass ratio into the multiplier tube, if one scans for more than one element, the quadrupole scans for one mass at a time, therefore realistically you can scan for about nine or ten masses before the time taken to scan all masses becomes inconveniently long to give reliable readings (in short you could miss a thin layer of material).

After ions enter and impact on the multiplier tube they cause a secondary electron cascade, the counts of which are registered and give a relative reading of the amount of material present in milled material.

This guide is meant to introduce you to the system and allow you to mill your sample unattended, as with all equipment if you don't have the *slightest* clue what you are doing ask someone for help, if you have a *slight* clue, remember "No Guts, No Glory!": just take responsibility if you mess up.

A.1 Water and Gas

In the chase of the cleanroom are the facilities for the Millatron, in order to get a plasma you need Ar gas and in order to keep the gun and sample from over heating you need running water.

1. Turn on water with valve marked V3 to obtain pressure at or slightly above blue marker line.
2. In gas cabinet - Open valve on top of Argon bottle.
3. *REMEMBER to close these valves after milling*

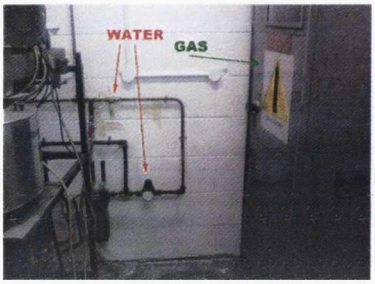


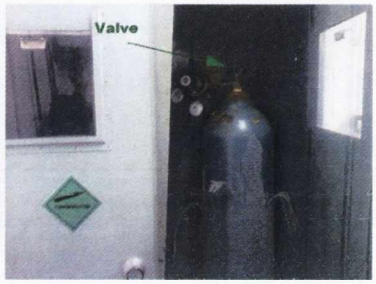

A.2 Dress up !

Put on lab-coat and blue overshoes without letting the overshoes touch the "dirty" side of the lab.

A.3 Venting the chamber

1. Verify that both the roughing pump (Mech. pump) and the high-vacuum pump (cryop-ump) are running
2. Hi-vac valve should be closed (switch in middle position) and rough valve should be closed (switch down)
3. Open black vent valve on the back of the chamber.
4. Let air fill the chamber, close the vent valve and open the door. The chamber is now vented.

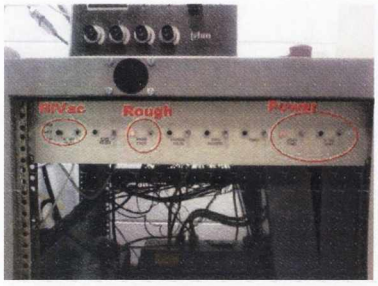

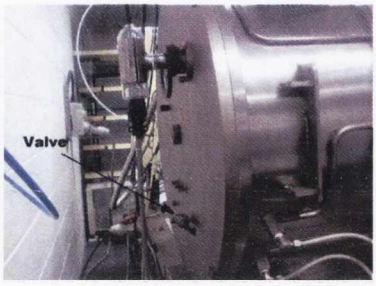

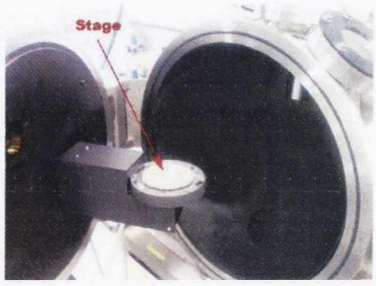

A.4 Sample Mount

If you are using the EPD you need to think about the mounting. If your sample is small and you mount it on a 4" wafer covered in resputtered material then the wafer will drown the signal from your sample, if you dont have a clean Si wafer you can use the Cu plate (unless of course you want to see Cu clearly). Mount your sample on the stage. Verify that the sample doesn't fall off when the wafer is turned upside down. Load the wafer into the sample holder in the chamber and use the four clams to hold it firmly in place. Close the door using the following procedure:

1. Close door while slightly lifting it into position and make sure it is centered
2. Open rough valve, if you are using EPD start the pumps on it as described in section A.6.
3. Let the pump do its work ...allow for 10 to 15 minutes of rough pumping before proceeding to next step, monitor the chamber pressure on the gauge on the rack. It must be below 10^{-2} before engaging cryo pump (hi-vac)

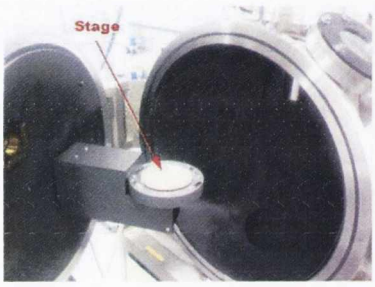

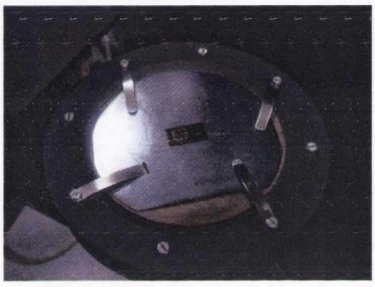

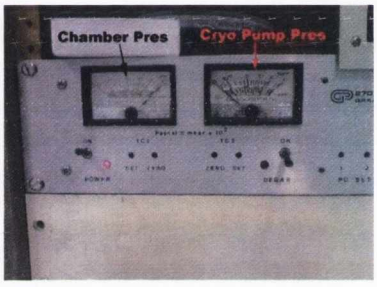

A.5 High Vacuum

Close rough valve then open high-vac valve. Start Ion gauge on "senTorr" (Varian BA) control unit.

- switch on on the back
- press "EMIS" to start the gauge

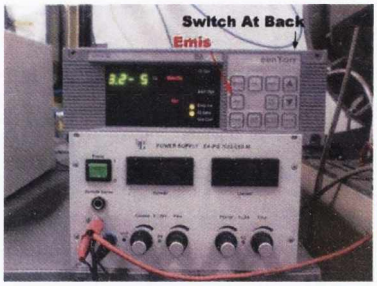

Let the chamber pump for $\sim$ 30 minutes to get into the low 10^{-6} or high 10^{-7} mbar range. This will take $\sim$ half an hour. The EPD pumps should also reach full speed within this time.

A.6 SIMS Unit set-up

This section is only needed if you plan to use the SIMS end-point detector. Skip to section A.9 if you rather mill only!

A.6.1 SIMS pumping system

On BOC-Edwards controller unit:

1. Use arrow keys to high-light "Turbo OFF - Back OFF". Press "On/Off" button twice. One time to enter the menu system and one time to start the turbo and the backing pump. Press "back/menu". The display should now read "Turbo ON - Back ON"

2. *WAIT* until turbo is running at half speed before turning on the SIMS penning gauge (AIMX in the BOC-Edwards controller). Sometimes the gauge will not "strike" if the vacuum is too low. This can also be done once the chamber has reached it's working vacuum (see section A.5).

Turn on both HIDEN controllers.

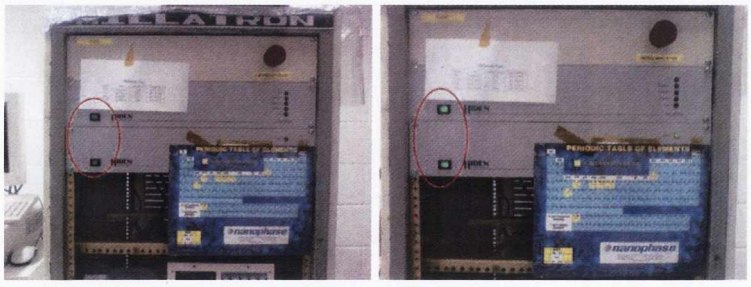

A.7 Ignite Plasma

1. Switch on power supply EA-PS 7037-050 CM *twice*. Should read $\sim$ 14.7 V and $\sim$ 4.00 A.

2. Allow Ar gaz into the chamber by switching on "Tylan" unit. Allow the unit to settle, it will go very high then very low then stabilise, do not fear, it is normal. Do not modify the gas flow.

3. Switch on ANELVA PRF-125C Power Supply (RF generator). This activates the RF controller unit.

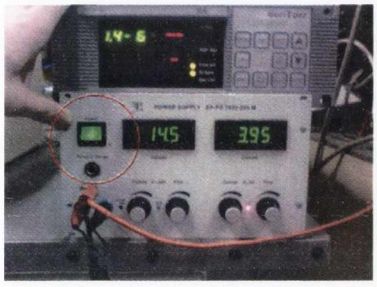

4. Set RF controller unit reflected power to 33.5 using the "up" and "down" buttons. This is equivalent to an incident power of 400 W.

5. Hold down "Confirm" and press power simultanously to ignite the plasma. The RF controller unit shoud read 0.40 and 33.5.

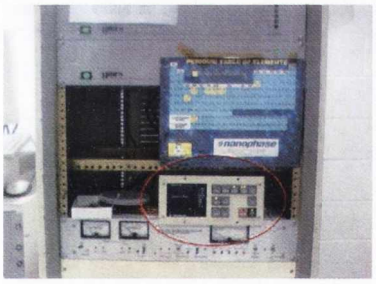

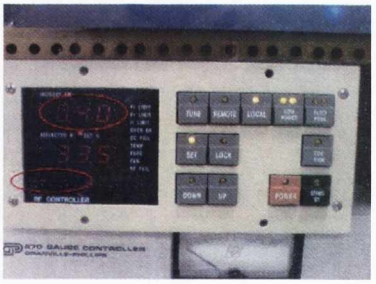

6. Turn off the ion gauge by pressing "EMIS"

7. Close hi-vac valve while looking into the chamber through the window. Once the plasma ignites, open the high-vac valve again

8. On the ion gauge controller, press "EMIS" again to turn on the ion gauge.

A.8 MAsoft software - SIMS/EPD Only

Log on to the computer with the password (if you don't know this, you haven't been trained). Open MAsoft from desktop shortcut. Then do the following.

1. Open an old file or, if you dont have one, hit file → new

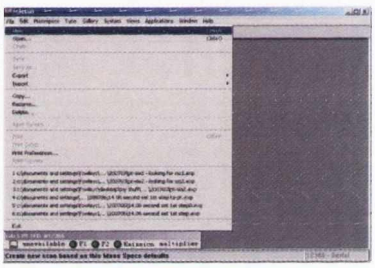

2. On the desktop open the relevant text file for what angle you want to mill at (45 °, 75 °, 85 °etc.)

3. In MAsoft doubleclick on the "RGA" box, change to "+IonSIMS".

4. be sure to check the multiplier voltage is correct (this is the most important setting), and if i find you using it at an incorrect voltage i will crucify you and ban you from the machine.

5. Change the settings according to the .txt file remembering to click the "change" button for each change.

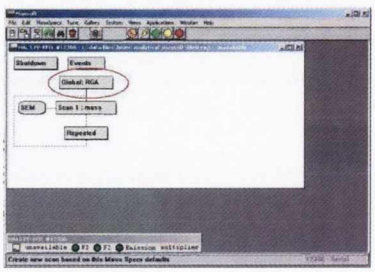
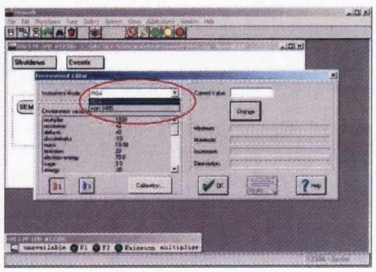
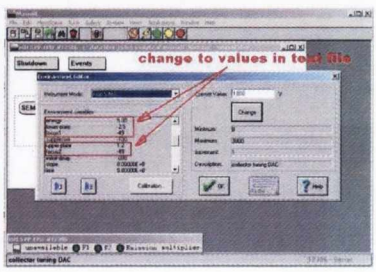

6. Double click "SCAN1:Mass" and change the name to whatever you want to scan (Fe, Au, ...) and also set the start and stop mass value to the same value corresponding to the mass of the majority isotope of your material.

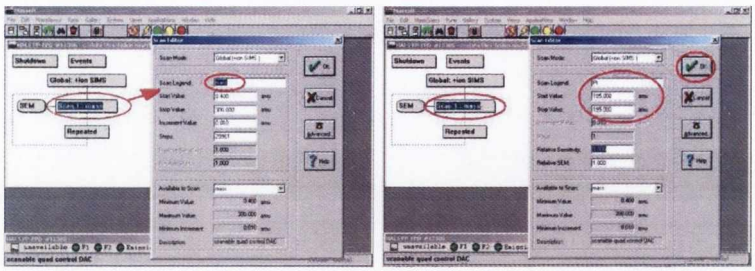

7. You can add more materials to be scanned by clicking the third button "box over box" and repeat the above point.

8. If you are scanning ions that give high counts (>10,000 counts), you should reduce the sensitivity of the detector to lengthen its lifetime. Doubleclick on "+IonSIMS" and change the value of "delta-m" to +50. Similarly for ions with low counts (<5000 counts) you can set this to a more negative value. If you want to this for only certain elements, you can use a *local* environment by clicking the 4th icon and clicking on the environment box above you element. This has the effect of changing the mass window which you detect, for Co, Ni, Fe set it to more positive values to close the window. For Ta, Pt, Au, set it more negative to enlarge the window and increase counts.[1]

You're now all set to SIMS detect. Click the green traffic lights, the select the mass from the scan-tree and click the binoculars to monitor that ion's evolution during the scan.

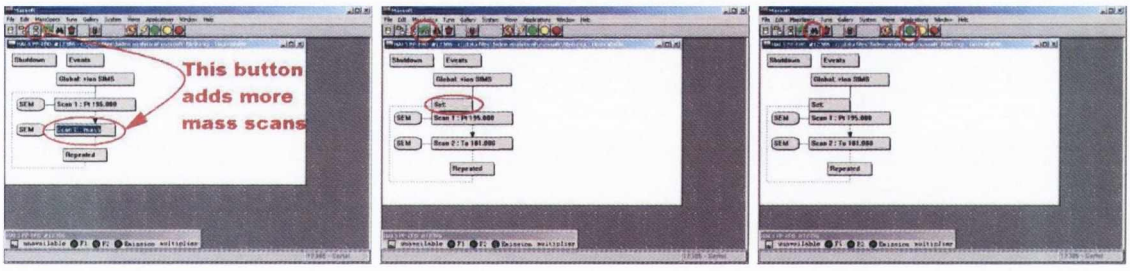

[1] That's what Ciarán says and it is true

A.9 Sample positioning

Switch rotation on with the switch located on the control unit attached to the chamber door. Manually tilt the sample stage to the angle you decide, or the angle you set for in the SIMS scan. Take a look into the chamber and verify your sample is rotating correctly. If you arent using the EPD when you see the Si wafer (or other substrate) stop the plasma (see section A.11).

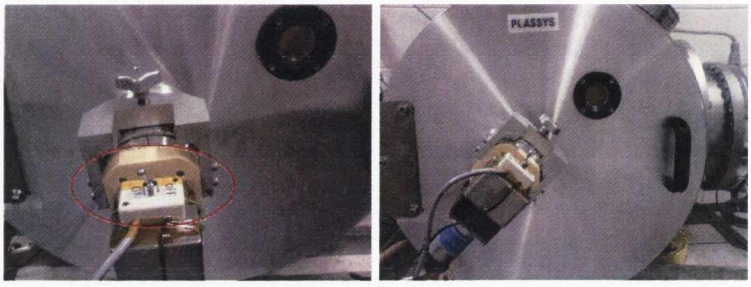

A.10 Monitor your SIMSing

A scan should look something like this It should have clear signals for when you mill through

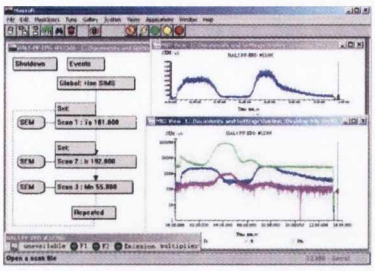

different layers, if your scan looks completely flat you need more help to run the EPD. Even if you do not see any change in the signals you are still using the multiplier, which has a finite lifetime which is determined by the number of ions that impact on it. So even though you see nothing the SIMS lifetime is decreased, please keep this in mind when using the SIMS.

A.11 Stop the milling

When your sample has been milled away it is time to stop milling. Follow these easy steps:

1. Click the yellow traffic light in MAsoft. This stops the SIMS scan.
2. On RF controller unit, hold down "confirm" and press "Stand-by" simultanously. This stops the plasma.
3. Switch off ANELVA PRF-125C Power Supply (RF generator)
4. Close off the Ar supply on the "Tylan" controller unit.

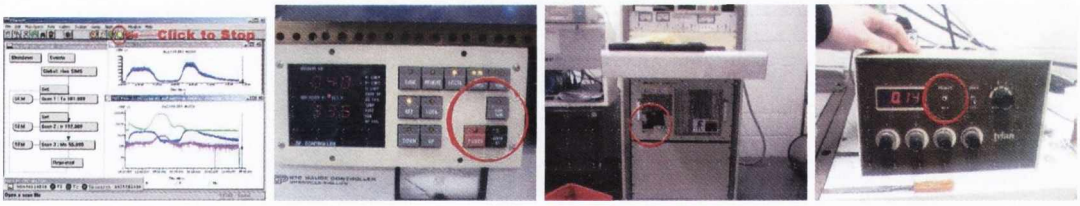

5. Save data files and the close MAsoft.
6. Turn off HIDEN controllers
7. On BOC-Edwards controller unit: turn off AIMX and turbo + backing pumps (see A.6.1)
8. Turn off ion gauge
9. Turn off the EA-PS 7037-050 Power Supply.

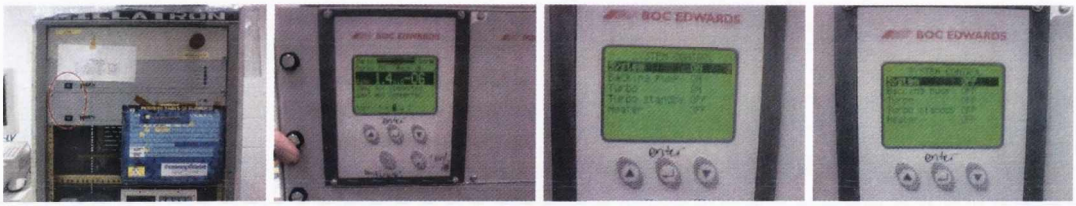

10. Rotate samnple stage back to horizontal and turn off sample rotation.
11. wait until SIMS turbo halts and Ar gun cools down.$\sim$ 20 minutes.
12. Close the Hi-Vac valve and verify the rough valve is also closed.

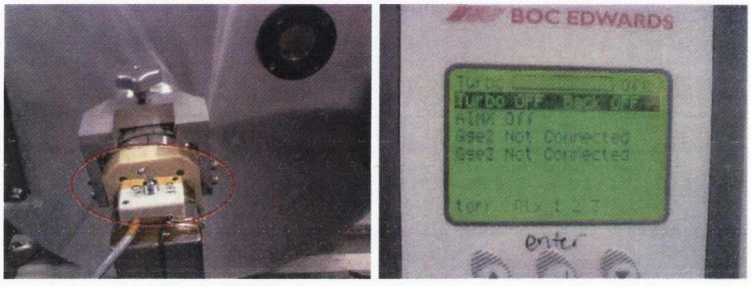

13. Vent the chamber (see section A.3), take out your sample.
14. Close door and rough pump only as described in A.4.
15. FILL IN THE LOGBOOK (VERY IMPORTANT).
16. On your way out, turn off water and gas as described in A.1.

Congratulations you have successfully milled your sample, pat on the back deserved

A.12 Maintenance

A normal user should not attempt this section.

Every month run "pm-test" and check the multiplier voltage, RGA mode under good vacuum. The multiplier voltage is important, re-run "pm-test" after new multiplier has been found.

Run "postune" once a year, with Ta foil, no rotation, for various milling angles. Check the energy, focus and plate voltages and save in the text files.

A.13 Cryopump Regeneration

In the event that the cryopump needs to be switched off, or the power fails etc, the following procedure must be followed to regenerate the pump. You CANNOT just switch it back on!

This guide assumes the following:

- The cryopump is off
- The pressure in the cryo is high. The pressure is read from the ion gauge on the rack labelled "cryo pressure"

To regenerate the cryopump do the following:

1. Make sure water is flowing to cryo pump.
2. Check the cryo pump pressure, on the ion gauge on the rack, it must be above 10^{-2} mbar.
3. Verify that both the High vacuum valve and Rough pump valve to the chamber are closed.
4. Open the fore-regen valve. This will pump excess gas from the cryo pump.
5. Wait until the cryo pump pressure is below 10^{-2} mbar.
6. Go into the chase and turn on the cryo pump. The switch is on the back of the compressor.
7. Wait around 10 minutes. Verify that the pressure in the cryo is going down.
8. Close the fore-regen valve. If this valve is left open and the cryo pump starts cryo-pumping then the pressure in the cryo will be lower than the rough pump. At this point you will be cryopumping the rough pump (this is not good).
9. Let the cryo pump cool down overnight to ensure it has good vacuum.
10. In the morning, verify that the cryo pump pressure on the gauge on the rack is maxed out to the left.
11. If the cryo pressure is high, there is a leak and the system should be checked.

Appendix B

Shamrock Deposition Troubleshoot

"There is nothing more dangerous than a resourceful idiot"
- Christopher P. Murray, Intel researcher in residence

B.1 Introduction

As all of the deposition work in this thesis took place in the Shamrock tool. This appendix is a compilation of the knowledge accumulated over the years. This appendix is also based on the work of other people not just myself.

B.2 Pulsed DC Sputtering of Aluminium Nitride

This work was conducted by a summer student, James Kally from University College Santa Barbara, during the summer of 2010.

Several AlN films were deposited by reactive sputtering in Chamber A of the Shamrock. The deposition power, N_2 gas flow, Ar:N_2 gas ratio and deposition pressure were all varied. The films were characterised by; XRR, to obtain surface roughness and film density information; XRD, to determine the texture of the deposited film; AFM, to determine the surface roughness; the breakdown voltage was determined by several two-point measurements to determine an average.

The AlN deposition process was optimised and the following recipe parameters were obtained.

Power	Pressure	Nitrogen Flow	Argon Flow	Deposition Rate
250 Watts	2.25 mTorr	40 sccm	10 sccm	0.00377 nm/second

(atmosphere contains approximately 80% N2 gas with these parameters)

The AlN film deposited with these conditions should have the following parameters.

Thickness	Deposition time	Average RMS roughness	Average breakdown voltage
27.17 nm	7200 seconds	0.361 nm	561 MV/m

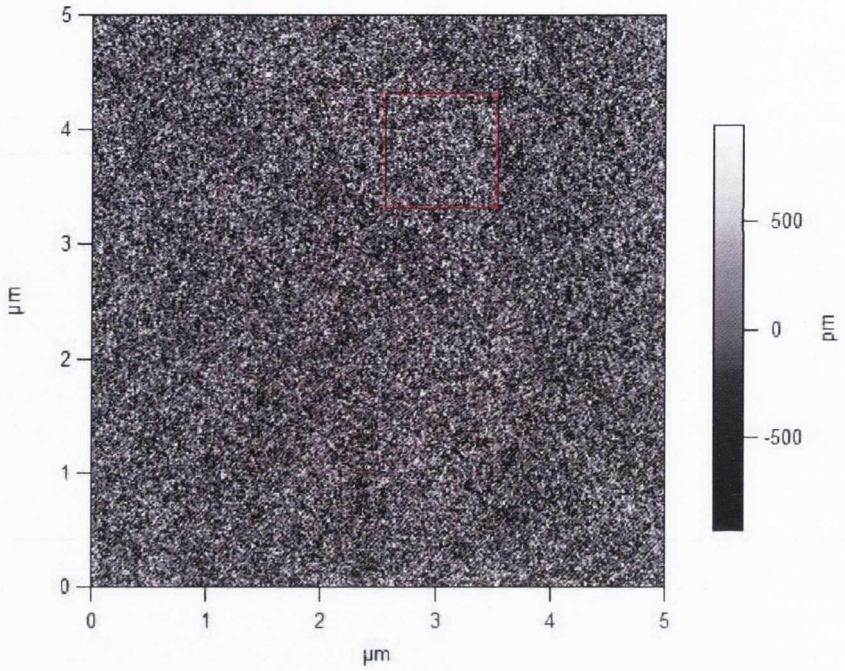

Figure B.1: AFM of AlN with the above deposition parameters

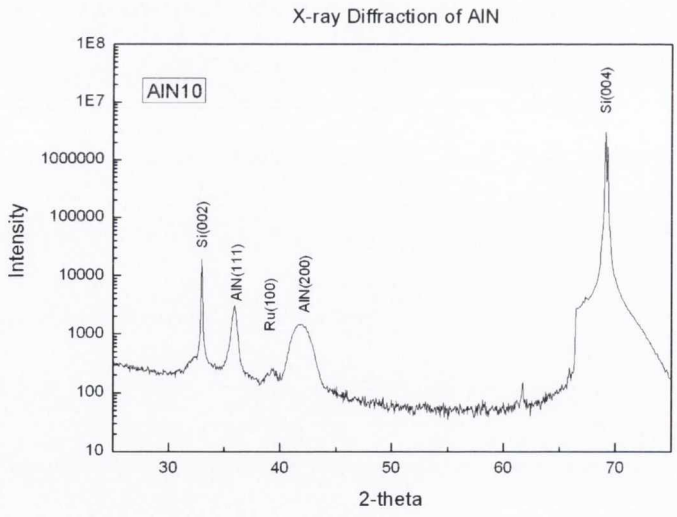

Figure B.2: X-ray diffraction of with the above deposition parameters. Note the AlN here is grown on a seed layer of Ta 5 nm / Ru 5 nm

B.2.1 Procedure Steps

- Ensure Al target is loaded in Gun 6. The process was optimised for this gun.
- Ensure pulser is connected to Chamber A, Gun 6. See Figure B.3.
- Load sample to CM.
- Verify the AlN recipe file contains the parameters given above (or any newly optimised parameters). Verify the deposition time is correct for your desired thickness.
- Insert AlN recipe into a pre-existing flow, or into its own flow.
- Unload sample to the CM.
- If you want to continue sputtering other materials it is advisable to run a *Burn-In All* process to remove any nitride contamination.

Figure B.3: Pulser wiring. Note the MDX shown here is Gun 5, Gun 6 is directly below

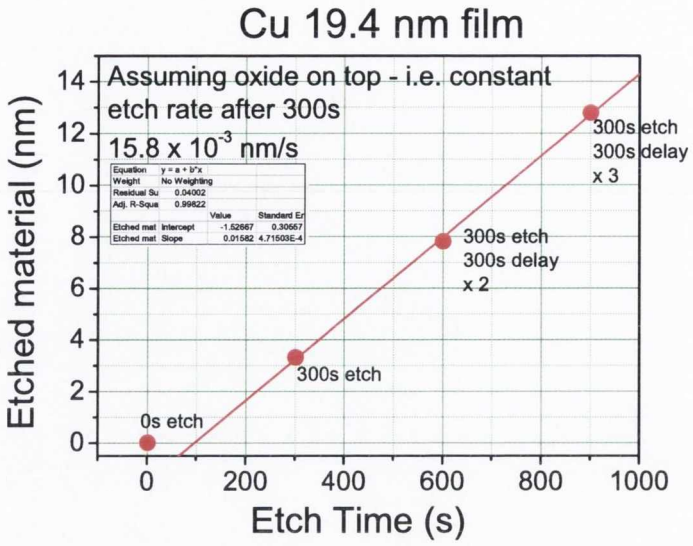

Figure B.4: Calibration of etch rates for Cu using the ion miller in Chamber A

B.3 Ion Milling

The ion miller is used primarily for substrate cleaning and native oxide etching prior to deposition. The ion milling recipes are stored locally on the ion miller controller in the mistic rack. Two programs have been saved, one with an accelerator voltage of 500 V the other with an accelerator voltage of 1000 V. In general the 1000 V recipe produces rougher films, where as the 500 V program etched uniformly. The etch rates were calibrated via XRR (see section 2.4.1). We used a calibration growth sample 1" square with a metal deposition for 1800s. The sample thickness was measured by XRR before etching took place. The sample was milled for 300 seconds with 3sccm Ar, then thickness was remeasured. The sample was then milled for 600 seconds (300 seconds etching, 300 seconds delay and 300 seconds etching), then thickness was remeasured. The sample was then milled for 900 seconds (300 seconds etching, 300 seconds delay, 300 seconds etching, 300 seconds delay and 300 seconds etching), then thickness was remeasured. The 300 second delay was used to avoid substrate heating from the filaments in the ion source. The sample is not actively cooled in the Shamrock, save conductive contact to the planet.

Calibrated etch rates for Cu, Ru and Ta are shown in Figures B.4 to B.6.

Sometimes the ion mill will return an error and there will be no apparent problem. This can happen if the preset task contains a large Ar gas flow. The sputtering Ar is injected, below the turntable, into the chamber close to the ion gun. Since the turntable is in between the gas injection point and the evacuating turbo pump the partial pressure can be very high in the vicinity of the ion gun. This will cause a large plasma current since there is more argon to be ionised. This can return an error to the Shamrock software (E-25).

This can be overcome by removing Ar gas from the preset task. I generally run a preset task with no Ar gas and the ion etching works fine. My recipes are named CF IONTETCH followed by the etching time, 300 s, 600 s... etc.

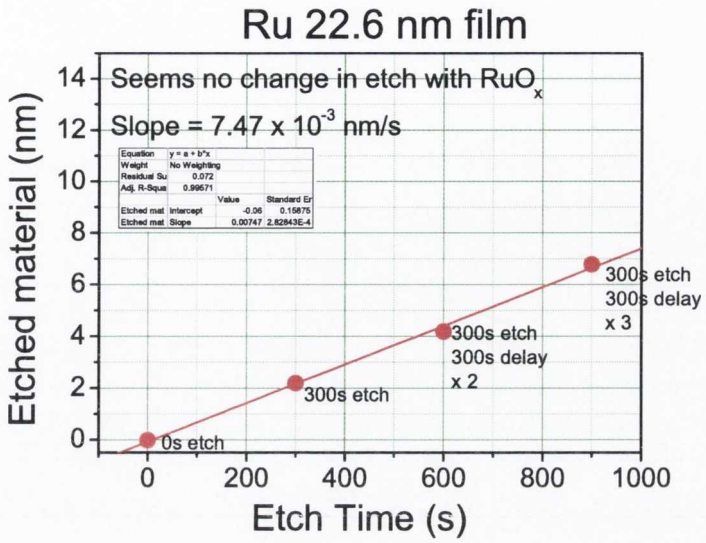

Figure B.5: Calibration of etch rates for Ru using the ion miller in Chamber A

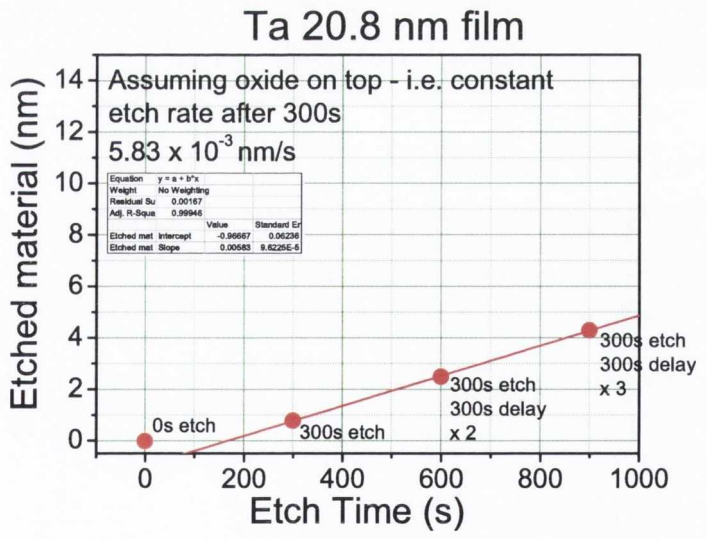

Figure B.6: Calibration of etch rates for Ta using the ion miller in Chamber A

B.4 Manual Robot Operation

The robot in the TM is a Genmark GB3 vacuum manipulator, it has an independent robot controller separate to the main Shamrock system. It can be controlled by the Shamrock MISTIC controller (automatic - interlocked) or by DOS command prompt directly (manual - non-interlocked). There is a series of commands that can be used in the manual mode which are listed below as well as the way to use such commands. Manual control over the robot is obtained by switching the communication cable from MISTIC to PC. This switchbox is located in the Shamrock rack beside the robot controller. Once the communication is switched the robot program is accessed from the SFI Shamrock program group (you may have to minimise the Shamrock software to see this - minimise is the small triangle in the top right corner of the Shamrock software. Double click the ROBOT icon. This will open the DOS interface window. Distances are imperial.

Whenever you use any of these commands, always try to keep a finger on F2 on the keyboard, this button will pause movement until you press it again. Using it is essential to prevent robot crashes. This program allows the transfer of wafers from Chamber A, B and C with relative ease. However, the program has **ABSOLUTELY NO INTERLOCKS**. If you tell it to move to a chamber when a slot valve is closed it will CRASH and you will have to FIX IT! You may also cause considerable downtime on the tool as a result of a crash.

Exercise EXTREME CAUTION!!!

The chamber names are different for the robot program and what we call the chambers.

Robots Chambers

A Cassette Module
B Chamber B
C PM / Chamber A
D Cs evaporation source inside the Transfer Module
E Chamber C (intermediate chamber before the UHV Chamber)

All slot valves have to be opened manually using the push buttons located on the lower left side of the Cassette Module.

General Commands

- ♯PIK1 This is the PICK command, it will pick up the wafer in slot 1 of the CM, ♯PIK2 picks slot 2 etc.
- ♯PLC1 This PLACES the wafer in the CM in slot 1, ♯PLC2 places in slot 2 etc. You should never place a wafer in a slot that is already occupied!!!
- RCPA - This gives the current position of the robot. It should be used before each movement

- MTCA Move To Chamber A, this moves the arm into the CM, with no picking of placing motion. MTCB will move to chamber B, MTCC to the PM etc. Etc
- MTSA Move To Setpoint A, this positions the robot such that it faces the CM, but the robot doesnt move from the center of the TM, it can be useful to use MTSB after loading a sample into Chamber B for example (in fact this is its most common use)
- MVRR, 10 MoVe Relative Radial this moves the arm towards or away from the center of the TM. The units are measured in 0.001 of an inch. MVRR, 1000 moves the arm 1 inch further from the center of the TM.
- MVRT, 10 MoVe Relative Tilt moves the arm left or right , units are in 0.01 of a degree. NEVER USE A NUMBER GREATER THAN 10 FOR THIS, MVRT, 1000 will probably cause the robot to hit the wall of the TM
- MVRZ, 10 MoVe Relative Z-Axis will move the robot arm in the vertical direction. Be CAREFUL as the robot arm height is normally quite close to the slot valve housing, moving too low will cause the robot arm to bend... and possibly break!

Moving the Elevator Platform

This is an extremely dangerous procedure, you should always exercise EXTREME CAUTION using this command!!!!!!

- RPE Read Position of Elevator. The elevator in the cassette module cannot move RELATIVELY only ABSOLUTELY. Therefore you need to be extra careful and always read the current position using RPE.
- MAE 1, 3000 MoVe Absolute Elevator 1. The units are measured in 0.001 of an inch. This will move the elevator to an absolute position 3 inches above the bottom of the CM.

You should only use these two commands RPE and MAE 1, XXXX in the following way in the robot program.

RPE [enter]	typed by the user
0, 0, 7653	returned by the robot controller
MAE 1, 7600 [enter]	typed by the user
0000	returned by the robot controller

B.5 Powering Down / Powering Up (after power failure)

The Shamrock is controlled in the following manner.

- A PC is connected via token ring ethernet to the MISTIC controller
- The MISTIC controller is connected to the rack heads.
- the rack heads connect (via analog voltage units from OPTO22) to the various subsystems of the tool, e.g. sputter gun supplies, ion gauges, mass flow controllers, power control relays etc.

If the power fails it is the racks that must be restarted in a certain sequence, such that the MISTIC controller is turned on last. Thus the power down sequence is as follows

- turn off the right most rack (which houses the MISTIC controller)
- turn off the middle rack (which houses sputter gun power supplies 1 - 3)
- turn off the left rack (which houses sputter gun power supplies 4 - 6)

The power up sequence is the opposite with one additional step. The power up sequence should be used when there is a power cut or if someone activates an emergency stop button on the tool.

- Turn off the racks from right to left using the the red OFF buttons at the bottom of the racks.
- Locate the Shamrock (208 V 3-Phase) power distribution board in the chase area of the cleanroom (CRANN L4.36).
- On the left of the panel there is a black button labelled "Reset". Press it. This will reset the entire power board to the tool. If this is not pressed then the tool doesnt respond after the full reset. I dont know what this button does, but it needs to be pressed FIRST.
- In the cleanroom, power on the racks from left to right (MISTIC unit last) using the large green ON buttons at the bottom of the racks.
- Restart the Shamrock controller software, the user name is 'gen' and the password is 'fg'
- Select TM on the bottom panel and select Pump All from the TM screen.

B.6 Misitc MMI Runtime

The Mistic MMI Runtime is allows the manual operation of several Shamrock subsystems. The panel on the left allows users to select certain chambers and perform various tasks with relaxed interlocks. For instance, a user can fire the sputtering guns without ensuring all four planets are loaded. This program is used for checking the plasmas on the sputter guns after changing the targets. This is outlined in the following section;

- Ensure that the base pressure in Chamber A is below 5×10^{-5} Torr.

- Click PM on the left menu. On the lower half of the screen there is a button to 'Turn Cooling Water On'. Cooling water is required before sputtering can take place.
- Click 'Sputter' on the left menu. Here you can enter gas flow values and gun powers. Enter 40 Sccm for Ar1 and set the power on all guns to 100 W.
- Click 'Ar1' to start the Ar flow.
- Click '1' to apply power to Gun 1, check the voltage and current. Voltage should be about 200-300 V and current should be about 0.2 - 0.3 A (i.e. 100 W)
- Click '1' again to stop applying power.
- Repeat to check the plasmas on Guns 2 - 6.
- When finished click 'Ar1' again to stop the gas flow.
- Click PM on the left menu and select 'PM Pump'

The MMI runtime is used; when calibrating the locations of planets 1 - 4; when calibrating the planetary alignment; for testing the turntable rotation while the chamber is open (to check for gear or idler wheel grinding).

It should not be used for deposition, only for troubleshooting.

B.7 Solid State Compact Flash HDD Upgrade

The Shamrock system is almost twenty years old. The original hard drive capacity was 1 GB. Modern hard drives (over 2/4 GB) are incompatible with the system. In order to incorporate redundancy into the system I switched the 1 GB magnetic hard drive to a 2 GB compact flash setup. Compact flash cards are readily available and fulfil the 2 GB limit imposed by the BIOS of the Shamrock controller computer. It is possible (at least theoretically) to introduce a new computer with larger hard drive compatibility and still control the Shamrock system. The major hurdle for such a project is the token-ring ethernet card (a living fossil!). Most modern motherboards will have no problem allowing the Windows 3.11 operating system to run. Several copies of Chamber A software are held on CF cards in the cleanroom. A DVD of the drive image as well as instructions how to load them to a CF card is held in the Shamrock rack.

Appendix C

Disco DAD3220 Wafer Dicer Manual

Wafer Dicing with the Disco DAD3220 Wafer Dicer

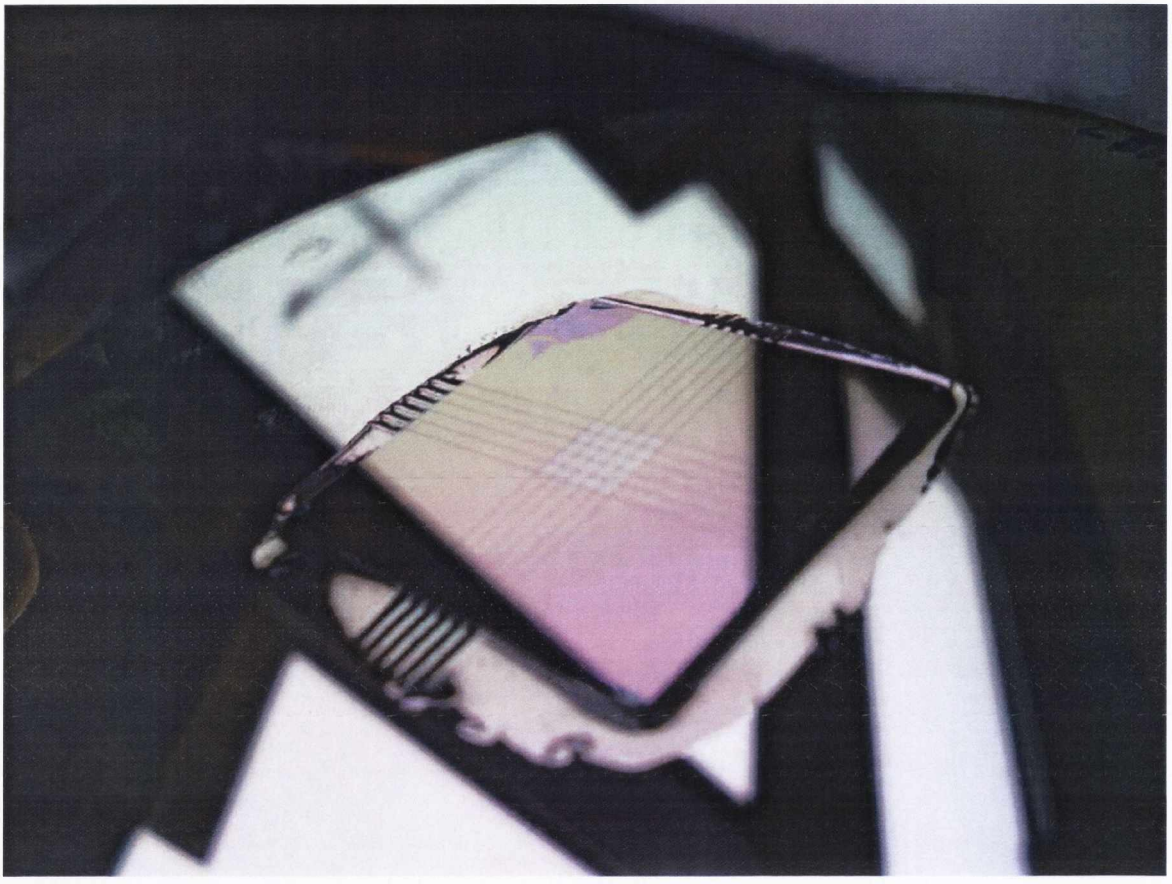

Tool Owner: Ciarán Fowley x4640
Second Contact : Dr. Huseyin Kurt x4637

Standard Operating Procedure - Rev 4

Introduction

The wafer dicer is what it is, a tool for dicing substrates into small chips for measurement. The system is based around a spinning diamond blade rotating at high rpm on an air bearing. The wafer is held by vacuum on a stage and the stage is moved towards the blade in order to cut your wafer. It can cut SiO_2, glass, MgO, STO.

The machine is fully automatic and can be taught to recognise patterned wafers by the surface features (which can be defined in the etching, there should be a section on this in the manual). As the spinning blade is cutting your wafer both the blade and the area being cut are showered with DI water, so if you want to protect your sample you could spin a layer of photoresist to protect it.

As with any machine here, you have to respect it and try to think about your process, this tool is generally for industrial use where full wafers are cut automatically by pattern recognition. Here, however, everyone is dicing different wafers. This guide will explain how to *scribe* (not fully cut through) a standard 4" Si wafer into chips of a particular size, for example 2×1 cm^2.

Scribing your wafer is much quicker than cutting fully through because the chuck required is different and you don't have to prepare your sample on a thin tape which takes about 5 minutes.

Facilities to the machine are DI water, chilled water, N_2 gas and compressed air.

This guide is meant to introduce you to the system and allow you to dice your sample unattended, as with all equipment if you don't have the *slightest* clue what you are doing ask someone for help, if you have a *slight* clue, remember "No Guts, No Glory!": just take responsibility if you mess up.

Important Notice: This machine is not set up to dice GaAs, InAs or any other As containing wafers!!!!! (it is dangerous)

For creating your own recipes choose the right type of dicing blade for your dicing job. The available dicing blades can be found at http://www.disco.co.jp/eg/products/blade/index.html.

Also as regards the SOP, users trained on this SOP are trained only in the basics of the tool. If you want to cut a different substrate, cut extremely small chips or use the tape mounting you must be trained further. If you attempt to use anything but the SOP without asking permission or being trained your usage rights will be revoked.

C.1 Prepare your sample

Before you dice, it is recommended that you spin photoresist on your wafer to protect the surface. The photoresist can be expired. Its only for protection and you will remove it with acetone afterwards.

If this step is a problem for you contaminating your sample you will have to design your own process after being trained on the machine.

As the wafer is being diced there will be a lot of debris moving around the surface of your wafer. the debris will be expelled by the blade but will be pushed by the DI water used to clean the cut. You can mount your sample on a thin tape but that requires additional training and a change of chuck table.

The machine is currently setup for a very quick turnaround time and ease of use regardless of Si substrate oxide. Different silicon wafers stick differently to the sticky tape method. With this stage the sample is held direct by vacuum and won't move around much.

If simply scribing your sample is not sufficient, then I will show you how to change the stage and use the tape method. But for the moment this is the easiest method to teach *and* to use.

C.2 Turning on the Tool

1. Check the N_2 and Compressed Air at the rear right of the machine. This should be left on normally, but if it is off turn it on *BEFORE* powering up the machine.
2. Check the pressure of N_2 (nominal 5 bar) and Compressed Air (nominal 7 bar) on the regulator on the wall. If these values are below the nominal values then the machine cannot be used safely. Inform the tool owner.
3. Turn on the DI water at the rear of the machine.

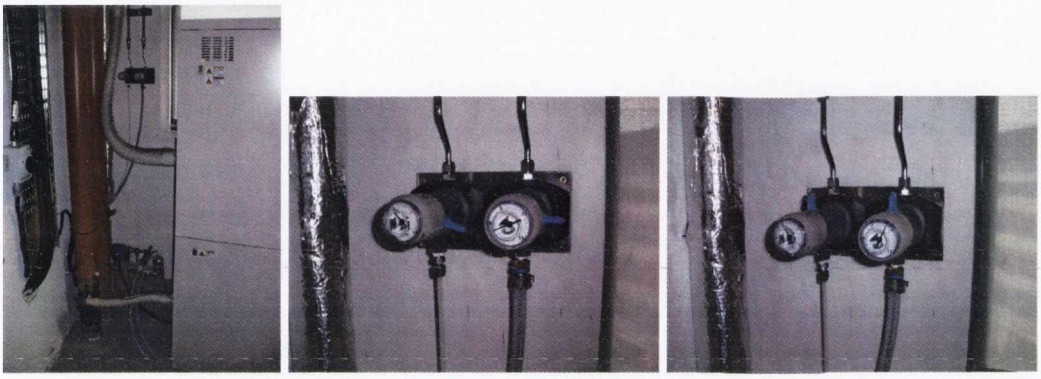

Figure C.1: (left to right) location of the gas and DI water connections; gas in OFF state; gas in ON state

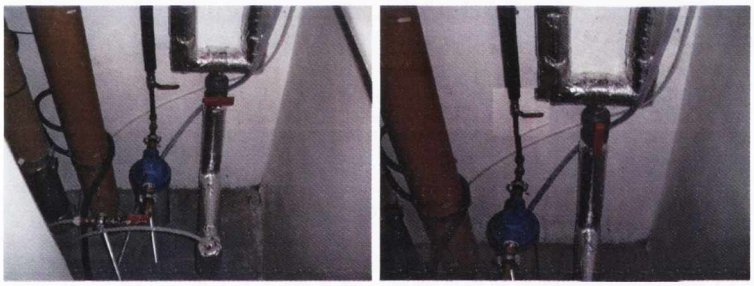

Figure C.2: (left to right) DI water in OFF state; DI water in ON state

4. Turn the "ignition" key to start and then release. The machine will now start up. Booting takes about three earth minutes. At this stage verify the cooling water flow rate from the flowmeter on the back of the machine. The cooling water flow rate should be greater than 1.8 L/min. The main cooling water is now connected to the Coey Groups chiller (the big white thing behind you beside the gas cabinet)
5. When the system boots you will be greeted by the main screen.
6. Look at the main air pressure, if it is not above 0.5 MPa *DO NOT PROCEED*. The blade spins on an air bearing and the clearance is about 10 μm (AFAIK) so you can imagine that a loss of pressure will cause the spindle to strike the outer wall.

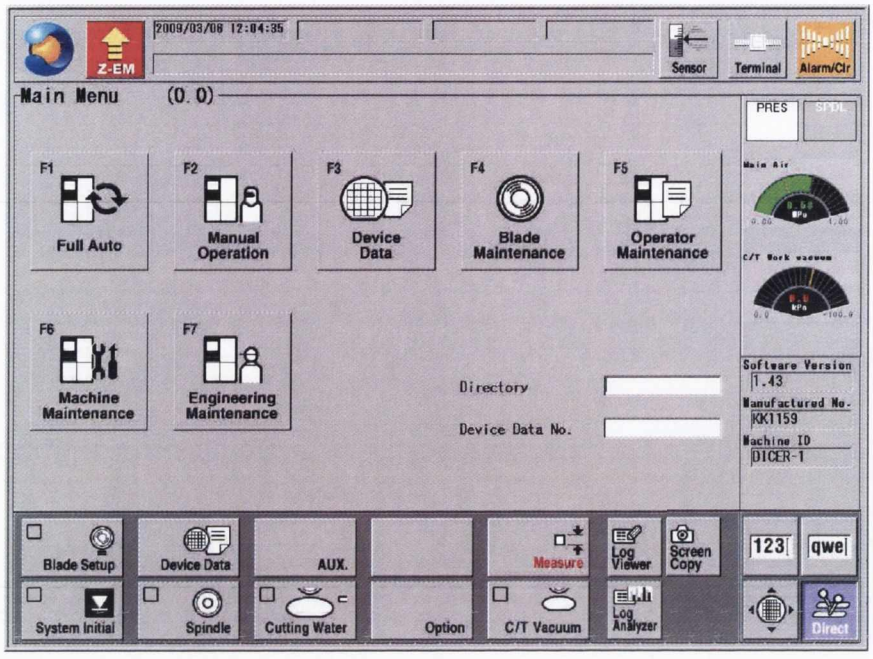

Figure C.3: Initial startup screen, note main air pressure 0.58 MPa

7. The system is now ready to be initialised.

C.3 Initialise the system

1. In the lower left corner press "System Initial". This will check the chuck rotation, stage movement and interlocks. If this fails you cannot proceed.
2. Open the blade side splash cover and visually check whether the blade has a uniform circular shape without any damage. If the blade is damaged it must be replaced. Contact equipment owner to replace the dicing blade.
3. Close the blade splash cover fully.
4. Push blade setup.
5. Push start to setup the blade parameters. This starts the spindle rotating and checks the blade to ensure it is OK for use.
6. Press Exit.
7. Press the "Cutting Water" button. This starts two DI water flows, one from the front of the blade (used to clean the cut on the wafer) and the other from the sides of the blade (which shower the blade to prevent damage).
8. To the bottom right of the main screen there are two water flow-meters, these should both read about 1 L/minute. If they dont adjust them using the small valves at the bottom of the meters, its ok for them to be a little high, but never to be lower than 1 L/min. The DI water should run for a while to allow for thermal stabilisation of the cutting blade.
9. During this 5 minutes you can prepare your sample if it is not already prepared.

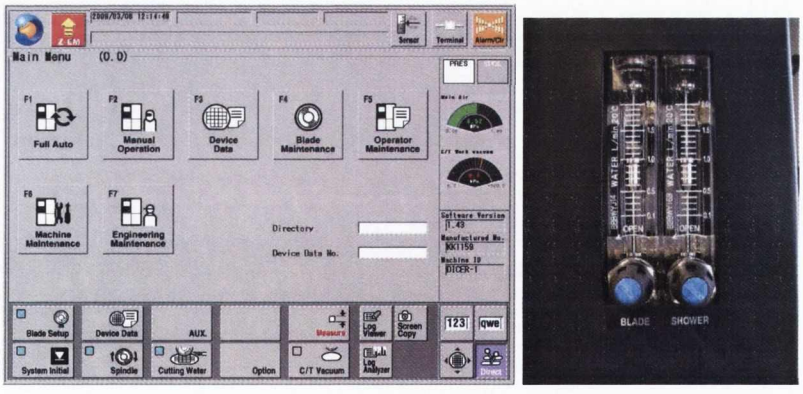

Figure C.4: Main operating screen, system initialised, spindle and cutting water started; Cutting water flows $\sim$ 1 L/min

C.4 Prepare your Dicing Recipe

The dicer can save everything you need to regularly cut wafers, blade height, chip size, inspection parameters etc. The only thing is that you have to load the file each time, so you might as well check during loading that no one has changed the parameters. Especially *Blade Height*, if this is incorrect you will *DESTROY* (and I do mean destroy) the blade. The figure below gives an outline of the dimensions that are important in wafer dicing. We will not use the "Tape", so the blade height is the height above the chuck table.

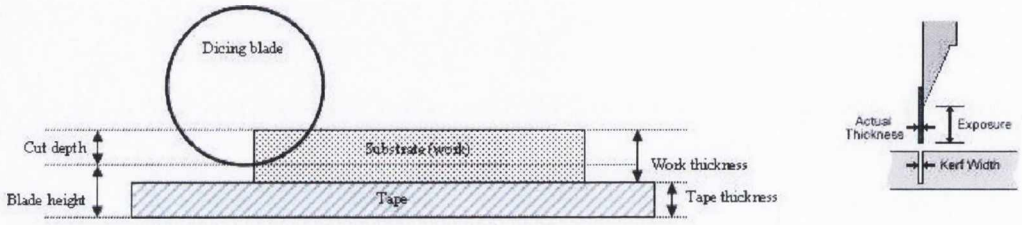

Figure C.5: Cut depth should be limited to blade exposure minus 0.1mm - BLADE EXPOSURE IS NOT EQUIVALENT TO MAX CUT DEPTH (it can be slightly wrong)

1. Select "Device Data", if you have diced before select your personal file, if you have not you will be trained on the SOP file in the CRANN folder - so select that.

2. When you select the file and press enter you will be taken to the device data screen.

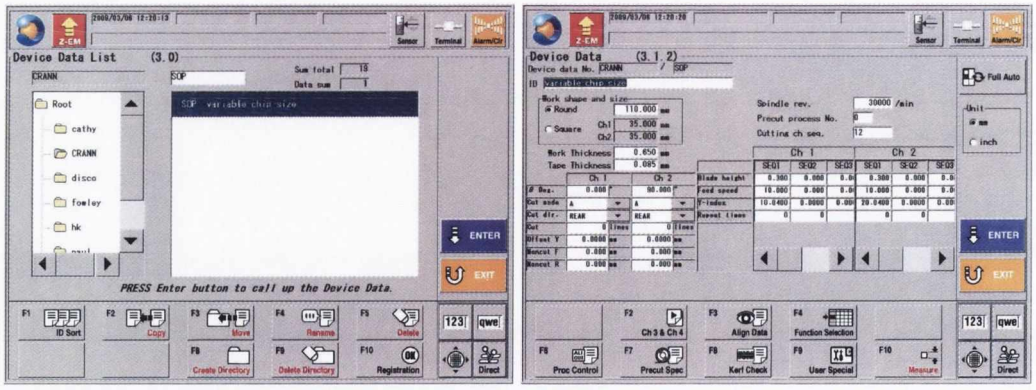

3. Important things around the screen;

   (a) **Work shape and size;** this is the size of your work piece, not the chip size you want. A 4" Si wafer is 110mm round. Of course you can enter all the sizes in inches if you want by changing the "unit" on the right hand side of the screen

(b) **Work thickness;** this is the thickness of your wafer, standard Si is 565 μm but if you mount your sample on hot wax you must know the full thickness, its very important for the blade height. This can be measured by the tool, but it is advanced and is not covered in this SOP. NB: wafer thicknesses as follows:

Diameter	2"	4"	6"	8"	12"
Thickness μm	275	525	675	725	775

NOTE: the machine can only handle up to 6" - but you may have chips from larger wafers.

(c) **Tape thickness;** this is the thickness of the tape, if you mount it that way, but for the SOP you wont use tape, ensure its set to zero.

(d) **Ch 1 and Ch 2;** these are the cutting directions, 0° is from left to right across the machine, and will correspond to the height of your chip, 90° is up and down, from user to the water and gas, and will correspond to the width.

(e) **Cut Lines;** this is important, if you want to cut your 10 cm wafer into 1 cm pieces you need at least 9 cut lines. If you want to cut it into 2 cm pieces then at least 4 cut lines are required. Cut Lines $\times$ Y-Index $<$ Work Size i.e. do not cut where your wafer is not.

(f) **Offset Y;** This can save some time for you, if you align to the wafer edge it will make the first cut this distance into the wafer. Setting this equal to your chip size (Y-index) then you will save one cut and the associated time.

(g) **Spindle rev.;** how fast the blade spins ($\approx$ 30k/min)

(h) **Cutting ch seq.;** this is important, there can be up to 4 channels, but you will use two. The sequence 12 corresponds to cutting channel 1 first, then channel 2.

(i) **Blade height;** *the most important thing*; This is the height relative to the chucktable surface. 300 μm corresponds to about half way through a 4" Si wafer. This is safe fast and sufficient. If you need a detailed explanation I will give you one. Enter the same number for Ch 1 and Ch 2. Never set the blade height below 200 μm, this is too dangerous to the blade, and you will be banned if found using heights below this.

(j) **Feed speed;** Should be set to 10, units are mm/s, faster feed speed will decrease the process time but you increase the risk of blade damage.

(k) **Y-index;** the size in each direction. You will notice 40 μm have been added to ch 1 and ch 2. this corresponds to the cut track width. If you dont add 40 μm then your chip wont be the exact size you specify, it will be 40 μm smaller in each direction.

4. Press exit twice to return to the main screen. It should show the filename on the main screen now.

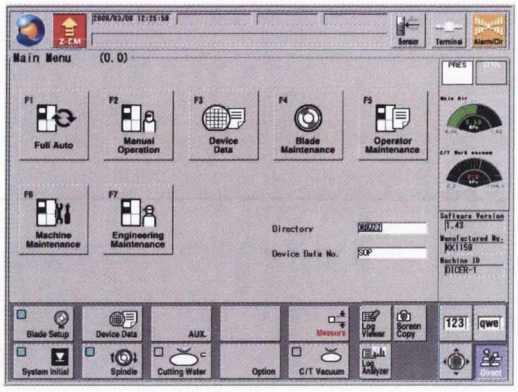

Figure C.6: Main screen after setting up "device data". Note the "Directory" and "Device Data No." fields are now populated

C.5 "Load" your wafer

Here you will load your wafer onto the metal wafer chuck, if the ceramic chuck is fitted then you cant do the following section (if you want to use the ceramic chuck you must be trained accordingly).

1. Slide the wafer chuck cover back on the right side of the tool.
2. Place your sample in the center of the chuck, if your sample is circular match the shape up to the concentric rings on the chuck for a good vacuum and ease of use.
3. On the computer screen press "C/T Vacuum" (chuck table vacuum) on the lower right hand of the screen.
4. Slide the wafer chuck cover back.

Figure C.7: Wafer loaded onto chuck table; C/T Vacuum button on lower right side

5. Press "F2 - Manual Operation".
6. Ensure the C/T Work Vacuum is sufficient (ensure it is green!)
7. You are now ready to align you sample for dicing.

Cutting Quarter Wafers

For processsing cuts of large wafers - say a qaurter of an 8" wafer from INTEL you should place the wafer in like so.

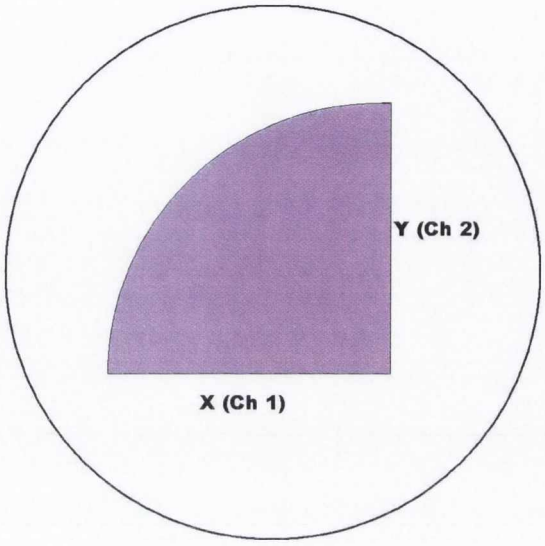

This allows you to align to the straight edges more easily.

C.6 Alignment of dicing axes

In order to cut your sample along a specific axes you must align the blade to that axis. This is usually the flat of a Si wafer or the edge of a square, or the alignment marks on your wafer. The dicer can align automatically between two reference points. In this example it will be the two ends of the wafer flat. But in other cases it can be two alignment marks on the opposite sides of a fully patterned wafer. You will first focus the camera on the sample, then align Channel 1.

C.6.1 Focus

1. *If your sample surface is out of focus it needs to be focused, but if you are processing multiple wafers you dont need to focus for each wafer - the machine will remember*
2. Press the "F2 - Alignment" button. The CCD microscope camera will engage with the wafer and show you the sample surface. This image needs to be focused, the reason is two fold, to see features on your sample and to gauge the height of the sample surface above the chuck table.
3. Using the four positioning arrows (in hi-speed mode) navigate to the wafer flat.
4. Press the "Focus" button on the lower panel. Then press "Auto Focus". This may not work first time, if you cant see anything on the surface please try again (yes i understand it is difficult with a clean Si wafer).
5. Once the sample is in focus you can now align.
6. Press Exit.

C.6.2 Alignment

1. Move the central solid line to the wafer flat on the left hand side of the flat. Press the "Align θ" button once.
2. The sample stage will be moved so you can align to the right hand side of the wafer flat, again using the four positioning arrows. Once you have moved the central solid line to the wafer flat on the right hand side of the flat press the "Align θ" button again. The computer will now rotate the sample stage to ensure the blade will pass through both of the points selected i.e. parallel to the wafer flat.
3. Next you will be asked to align the "hairline" to the "street". This only matters with a fully patterned wafer, the street would run through the alignment marks that separate the chips on your wafer. In the case of an unpatterned wafer it simply selects the point at which the first cut will take place (in general this is the wafer edge). The last direction you must move is UP, this is to ensure the wafer cuts the line you specify.
4. Press Enter
5. The machine now wants you to align Channel 2, however since by proxy it is aligned when you align Channel 1 you can simply press the "Align θ" button twice *WITHOUT ADJUSTING ANYTHING.*

6. You must now align the "hairline" to the "street" for Channel 2. Navigate to the wafer edge closest to you and select a point inside the wafer where you want it to start the cut. Again this is the wafer edge. Again The last direction you must move is UP.

7. After alignment is done, press Enter. This returns you to the Manual Operation screen.

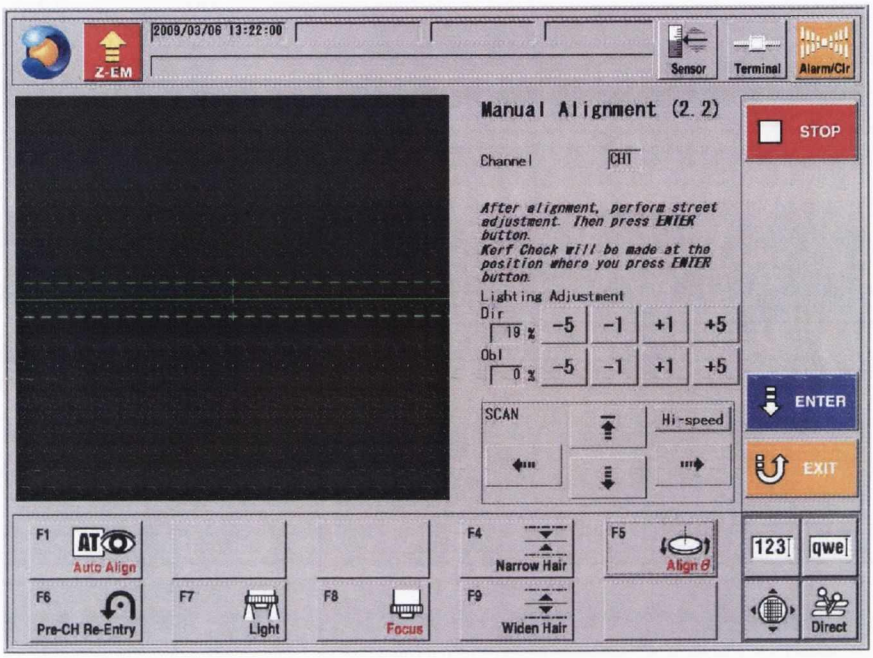

Figure C.8: Manual alignment window, bottom panel buttons for Focus and Align θ.

C.7 Dicing

You have successfully setup aligned and mounted your sample and it is finally ready to be cut.

1. Press the "Cutting Auto" button
2. Press "Start", the length of time this takes depends on the number of cuts required. To see how long it takes press - F4 Status and it will give you the exact time of finish.
3. When the cut is finished press the "Alarm/Clr" button to silence the alarm.
4. Press Exit.
5. Press C/T Vacuum to return the chuck to its home position.
6. Slide back the sample cover and remove your wafer.
7. Use the N_2 gun on the front of the machine to blow the excess water from your sample. Some paper should be on the window sill to the right of the machine.

C.8 Power Down

1. Press "spindle" to slow down the blade.
2. When the spindle has stopped, inspect the blade and note any damage to the tool owner.
3. Turn the "ignition" key to the off position.
4. After the PC has shut down, turn off the DI water.
5. Leave the N_2 and the compressed air ON.
6. ALWAYS SIGN THE LOGBOOK

Congratulations you have successfully diced your sample, pat on the back deserved.

Quick Operation for *TRAINED* Users

- Turn on the tool, water and gas
- Press "system initial"
- Press "blade setup" - check remaining blade exposure (should by smaller than your cut depth)
- Test cutting water and flows.
- Select your recipe in device data
- Verify recipe - expecially blade height. Check the number of lines aswell.
- Load your sample on the chuck table - press CT vacuum
- Press "Manual Operation" and press "Alignment"
- Align your sample and set the place for the first cut
- Align subsequent channels and set the place for the first cuts
- Press cutting auto - hit start
- Done
- FILL IN THE LOGBOOK